Stony Brook University

Bayesian Reliability Analysis and Nonlinear System Identification for Complex Particle Accelerator Protection Systems

A Dissertation Presented

by

Prachi Chitnis

to

The Graduate School

in Partial Fulfillment of the

Requirements

for the Degree of

Doctor of Philosophy

in

Electrical Engineering

Stony Brook University

December 2015

Stony Brook University

The Graduate School

Prachi Chitnis

We, the dissertation committee for the above candidate for the

Doctor of Philosophy degree, hereby recommend

acceptance of this dissertation.

T. G. Robertazzi – Dissertation Advisor
Professor, Department of Electrical and Computer Engineering

K. A. Brown – Dissertation Advisor
Control Systems Head, Collider Accelerator Department, Brookhaven National Laboratory

W. Tang – Chairperson of Defense
Associate Chair and Associate Professor, Department of Electrical and Computer Engineering

S. Hong – Committee Member
Professor, Department of Electrical and Computer Engineering

N. Tsoupas – Committee Member
Adjunct Professor, Department of Physics and Astronomy
Brookhaven National Laboratory

This dissertation is accepted by the Graduate School

Charles Taber

Dean of the Graduate School

Abstract of the Dissertation

Bayesian Reliability Analysis and Nonlinear System Identification for Complex Particle Accelerator Protection Systems

by

Prachi Chitnis

Doctor of Philosophy

in

Electrical Engineering

Stony Brook University

2015

Relativistic Heavy Ion Collider (RHIC) at Brookhaven National Laboratory is used to study primordial form of matter that existed in the universe shortly after the Big Bang. Enormous energy (72 MJ) is stored inside RHIC in the form of ion beams and superconducting magnet currents during operation. The accelerator Machine Protection System (MPS) is used to safeguard against undesirable energy leakage due to the faults developing in the collider, and needs to be highly reliable. The most crucial parts of MPS are the Beam Permit System (BPS) and the Quench Detection System (QDS).

The BPS monitors the health of RHIC subsystems and takes active decisions regarding safe disposal of the stored energy. The first segment of this dissertation aims towards Bayesian reliability analysis and quantitative estimation of system level catastrophic events of BPS which can lead to significant downtime of RHIC, and to identify the weak links in the system. A dynamic Monte Carlo failure model is developed, with modules having exponential lifetime distribution with competing risks. The module failures are calculated by Fault Tree Analysis, which traces down system level failures to component failures. This model is verified by an equivalent mathematical probabilistic model. A Bayesian reliability model is then employed to integrate the failure model and the historical failure data of BPS. It is based on a two-parameter Weibull

distribution with unknown scale and shape parameters, and implemented using Markov Chain Monte Carlo algorithm.

The QDS is responsible for detecting the superconducting magnet quenches and initiates the magnet energy dump. The second segment of this dissertation aims towards the accurate determination of developing quench failures, through remodeling the superconducting magnet behavior using Nonlinear System Identification. This reduces the false failures in the system, thereby enhancing the availability of the system. A mathematical memory model is conceptualized to define the highly nonlinear behavior of magnets undergoing saturation and hysteresis. This model shows good compliance with the data. It eliminates the manual calibration of hundreds of magnet lookup tables every year.

More importantly, this work generates design recommendations for reliable protection systems of upcoming eRHIC project at Brookhaven National Laboratory, first of its kind in the world.

To the One

Table of Contents

List of Figures

List of Tables

List of Abbreviations

ADC	Analog to Digital Converter
AIC	Akaike Information Criterion
AKM	Abort Kicker Module
B	Blind failure
BIC	Bayesian Information Criterion
BNL	Brookhaven National Laboratory
BPS	Beam Permit System
CeC	Coherent electron Cooling
CERN	Conseil Européen pour la Recherche Nucléaire (European Council for Nuclear Research)
CW	Continuous Wave
DD	Dirty Dump failure
DSP	Digital Signal Processor
eRHIC	electron Relativistic Heavy Ion Collider
ERL	Energy Recovery Linac
FB	False Beam abort failure
FFAG	Fixed Field Alternating Gradient
FIT	Failures In Time (failures per 10^9 hours)
FMEA	Failure Mode and Effect Analysis
FMECA	Failure Mode, Effect and Criticality Analysis
FMES	Failure Mode and effect Summary
FQ	False Quench failure
FTA	Fault Tree Analysis
LHC	Large Hadron Collider at CERN
MCMC	Markov Chain Monte Carlo
MH	Metropolis Hastings
MPS	Machine Protection System
MTTF	Mean Time To Failure
NHPP	Non Homogenous Poison Process
PI	Permit Input
PM	Permit Module
PMIO	Permit Module Input-Output strip
QCD	Quantum ChromoDynamics
QDS	Quench Detection System
QI	Quench Input
RBD	Reliability Block Diagram
RHIC	Relativistic Heavy Ion Collider
SMRX	Single Mode fiberoptic Receiver
SMTX	Single Mode fiberoptic Transmitter
SRF	Superconducting Radio Frequency
VME	Versa Modulo Euro

Acknowledgments

I express my deepest gratitude to my advisor, Dr. Kevin Brown for his continuous support throughout my Ph.D. research, and bestowing me with his patience, motivation, enthusiasm, and immense knowledge. I am thankful to him for reviewing my work, providing suggestions on my views, and helping me understand and deepen my ideas.

I am extremely grateful to my advisor Prof. Thomas Robertazzi, for his invaluable help, encouragement and reviewing of my work. I thank him for furnishing insightful comments that were thought-provoking and helped enriching the content of the work.

I would like to sincerely thank Prof. Wendy Tang and Prof. Sangjin Hong for sparing their invaluable time for the assessment of this work. I heartily thank Nick Tsoupas for providing valuable insights on RHIC magnets and for agreeing to evaluate my work as a defense committee member.

I specially thank Prof. Svetlozar Rachev, who helped built strong fundamentals in Bayesian statistical framework and furnished vision into the reliability assessment aspects.

I would like to thank Don Bruno for his constant assistance, help with testing the inductance tables and providing the magnet data. I also thank George Ganetis for his guidance in explaining RHIC magnet characteristics. I would like to thank Animesh Jain for providing knowledge about the saturation characteristics of RHIC magnets. I thank Carl Schultheiss for giving ideas about memory modeling of hysteresis of magnets.

I would like to thank Charles Theisen for cogitations on technical details of beam permit system that helped me understand it to greater depths. I thank Ralph Schoenfeld for help in mining the historical failure data and providing important documentation.

Many thanks to the entire crew of Controls Group at BNL for their immense help and support. I am grateful to Brookhaven National Laboratory and Stony Brook University for enabling the use of excellent facilities for my research work and providing best possible support.

Last but not the least, I would like to thank my family and friends, whose love, encouragement, continued help and moral support kept me successfully going through my dissertation work.

This work is supported by Brookhaven Science Associates, LLC under Contract No. DE-SC0012704 with the U.S. Department of Energy.

Awards and Publications

Award

Experimental Physics Control Systems Prize by European Physical Society, for significant contributions to the reliability of RHIC beam permit system.

Publications

1. P. Chitnis et al., "Bayesian Reliability Model for Beam Permit System of RHIC at BNL", International Conference on Accelerator and Large Experimental Physics Control Systems, Melbourne, Australia, 2015 (Invited talk)
2. P. Chitnis et al., "Nonlinear System Identification of Superconducting Magnets of RHIC at BNL", International Conference on Accelerator and Large Experimental Physics Control Systems, Melbourne, Australia, 2015 (mini-talk)
3. P. Chitnis et al., "Understanding the Failure Characteristics of the Beam Permit System of RHIC at BNL", International Conference on Accelerator and Large Experimental Physics Control Systems, Melbourne, Australia, 2015
4. P. Chitnis et al., "A Monte Carlo Simulation Approach to the Reliability Modeling of the Beam Permit System of RHIC at BNL", International Conference on Accelerator and Large Experimental Physics Control Systems, San Francisco, CA, 2013
5. P. Chitnis et al., "Quantitative Fault Tree Analysis of the Beam Permit System Elements of RHIC at BNL", International Conference on Accelerator and Large Experimental Physics Control Systems, San Francisco, CA, 2013
6. P. Chitnis et al., "Analytical Modeling of Inductance for Saturation and Hysteresis of Superconducting Magnets", submitted for journal publication
7. K. A. Brown, P. Chitnis et al., "Machine Protection Issues for eRHIC", International Conference on Accelerator and Large Experimental Physics Control Systems, San Francisco, CA, 2013
8. K. A. Brown, P. Chitnis et al., "Control System Issues and Planning for eRHIC", International Conference on Accelerator and Large Experimental Physics Control Systems, San Francisco, CA, 2013

Chapter 1

Introduction

The engineering industry has been expanding exponentially since the industrial revolution, with systems evolving to unprecedented level of complexity. Getting a full understanding of the functioning and interactions of these complicated systems is always a challenging task. This can result in unforeseen events causing system failures. The failures can range from causing inconvenience to severe societal, environmental and economic impact. Some of the events that caused catastrophic aftermath resulting into accidents [1] [2] like the Three Mile Island incident, the space shuttle Columbia accident, the Chernobyl nuclear accident, the Bhopal industrial accident and the numerous aircraft accidents signify the need of highly reliable designs for complex systems, with evaluation of risks associated with them.

1.1 Motivation

On 19 September 2008 [3], a faulty electrical connection between two magnets at LHC (Large Hadron Collider at CERN, Geneva) resulted into a Helium system failure that runs the liquefied Helium at 4K temperature. This event resulted into evaporation of about 6 tons of Helium causing the explosion of vacuum sealed systems and Helium leakage into the LHC tunnel. About 200 MJ of energy was instantly deposited at the failed interconnect region between two magnets. This vaporized the magnet bus and the cryogenic pipe inside the interconnect bellows between two magnets and the vacuum beam tubes were seriously damaged. The estimated cost of repair was USD 20 million and took more than a year of downtime before the operation could be restarted. Fig. 1 shows the seriously damaged vacuum beam tubes of the LHC.

For any complex systems containing huge amount of energy, it is very important to assess the reliability and estimate the probabilistic risk associated with the catastrophic events. The design of

the LHC systems is quite similar to the systems of the Relativistic Heavy Ion Collider (RHIC) [4] at Brookhaven National Laboratory. This emphasizes the importance of analyzing RHIC reliability as well.

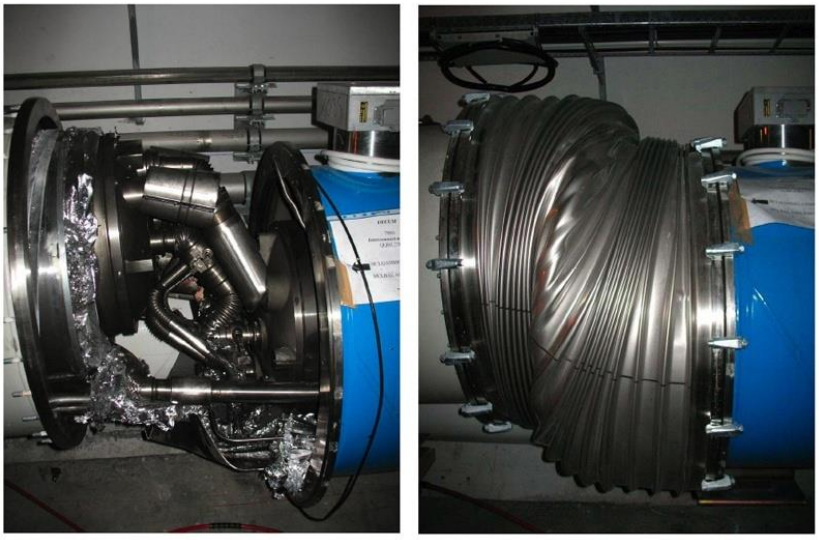

Figure 1: Seriously damaged vacuum beam tubes of LHC, Geneva

RHIC is a hadron and ion collider, which is a type of particle accelerator that smashes bunches of ions or particles together. RHIC enables the studies of nuclear phenomena in collisions of positive ions and protons, which helps answering how the universe looked like in the first few microseconds of the Big Bang [5]. It consists of two rings, called yellow and blue rings that circulate two counter revolving beams of positive particles. The beams collide at six interaction regions around the ring where the collision phenomenon is studied using sophisticated detectors.

The energy stored in RHIC during a run has high damage potential, which underlines the need to safely contain and dispose this energy. The peak energy stored in RHIC is 72 MJ at full energy operation, with about 70 MJ in the superconducting magnets current and 2 MJ in the particle beams. Any fault in the machine can cause an instant leakage of this energy in outer environment that could be hazardous to equipment. To protect against such unsafe disposal of energy, the RHIC Machine Protection System (MPS) is employed. It protects the collider from the anomalous conditions occurring inside the machine by dumping the stored energy safely. The reliability of MPS thus directly impacts the reliability of RHIC. Hence, there is an inherent need for high reliability of a safety critical system like MPS. The most critical parts of the MPS are the Beam

Permit System (BPS) and the Quench Detection System (QDS). The BPS is the controlling part of the MPS that takes decision for extracting the energy out of the collider in a controlled manner. The QDS detects the quench in superconducting magnets, and reports it to the BPS. A quench if undetected can release almost all stored energy (70 MJ) in an instant. This work aim towards the reliability analysis of two most crucial elements, the BPS and the QDS, with a focus on failure risk assessment of the BPS using Bayesian analysis, and remodeling for magnets using nonlinear system identification for reliable detection of the quench failures.

1.2 Objective

The RHIC MPS ensures the safety of the machine equipment. It is utmost important for a safety critical system like MPS to be highly reliable. The fundamental objective of this work is the quantitative estimation of the MPS risks associated with the failures that compromise the safety and availability of RHIC, and the reliability enhancement by improving the failure detection through nonlinear system identification.

The failures occurring in MPS can be broadly classified in two categories. A fail-safe condition shuts down the machine even if there is no fault reported to the MPS. This failure compromises the availability of RHIC. This type of failure is called a *False* failure. Another failure is where a fault reported to the MPS is ignored by it. This failure is quite dangerous and compromises the safety of RHIC. This type is called a *Blind* failure [6]. There is another category of failure in which the MPS sweeps the beams while dumping the beams. This elevates the radiation levels inside the tunnel. This failure is called a *Dirty Dump* failure, and is less severe than the false or blind failure. Following failures will be analyzed in subsequent chapters.

1. False Beam Abort failure: Beams are dumped due to an internal failure in MPS
2. False Quench failure: Beams are dumped and magnets are shut down due to an internal failure in MPS
3. Blind failure: Beams and/or magnet currents are maintained in spite of an actual fault in the field
4. Dirty Dump failure: Beam is swept across the beam pipe while dumping, which increases the radiation levels

The probabilities will depend on the MPS configuration and the reliability of different components and subsystems. They also depend upon the number of faults reported to the MPS. The false beam abort failure and dirty dump failure are attributed to BPS only, whereas the false quench failure and the blind failure are attributed to BPS and QDS both. This analysis will also highlight the failure prone components in the machine, and the impact of design configuration of elements on the reliability.

The aim of this research is towards the reliability assessment and the improvement of the two most vital parts of MPS: the BPS and the QDS

1. Beam Permit System: BPS is responsible for making active decisions regarding safety of the machine, for aborting the beams and extraction of the magnet currents. This work assesses the probability of BPS failures that could lead to substantial downtime. A fail-safe condition imparts downtime to restart the machine, while a failure to respond to an actual fault can cause potential machine damage and impose significant downtime. The aim is to explore the finer failure characteristics as well as provide system level perspective to the BPS reliability. It entails using the various information sources such as the manufacturer supplied failure data for components, various failure data handbooks as well as the historical failure data collected over the 15 years of RHIC operation.
2. Quench Detection System: QDS is responsible for detecting the developing quench states inside the magnet and reporting it to the BPS, thus safeguarding against the leakage of magnet energy. A model based quench detection scheme is employed in RHIC for the protection of superconducting magnets, which replicates the magnet behavior. A deviation of the magnet behavior from the model is detected as a *Quench* (a transition from superconducting state to a normal conducting state). Due to indeterminate nonlinear nature of the magnets attributing to saturation and hysteresis, this model is manually calibrated introducing inaccuracies and false failures. This work aims towards automatic calibration of the magnets along with development of mathematical model to quantify the nonlinear effects associated with saturation and hysteresis to a higher degree of accuracy.

RHIC has been in operation since 2000. RHIC systems are very similar to the LHC systems. A near future upgrade to RHIC will be eRHIC, which will be an asymmetric collider, colliding

electrons with positive particles. One of the RHIC ring and its associated subsystems will be replaced by an electron accelerator and its subsystems. Thus eRHIC will be a combination of old RHIC systems as well as newly designed systems. This reliability analysis of RHIC MPS will benefit in two ways:

- Providing reliability figures for systems that will be intact in eRHIC
- Providing intelligent decision support for the eRHIC MPS design

1.3 Literature Survey

Latest developments in the field of accelerator reliability are highlighted in the recent conferences on experimental physics control systems. A number of papers were presented at the recent conferences that emphasized on the improvements of the accelerator systems for attainment of high reliability [7] [8] [9] [10] [11] [12] [13] [14] [15] [16] [17] [18] [19]. In [20]a qualitative hazard driven approach has been adopted for the design of safety systems of CLS accelerator using of IEC 61508 safety standard. A study [21] has been conducted for the safety analysis of personnel protection system of Apollon laser facility according to EN 60825standard. Another reliability evaluation of beamline personnel safety system of ANKA facility is reported in [22]. A previously developed analytical reliability model system [23] for LHC beam dumping is updated with newer operational data that led to the discovery of 10 new failure modes. Online monitoring of equipment failures is another technique to enhance reliability and reduce downtime of machine that is discussed in [24]. A rule based diagnostics is applied for MPS of PETRA-3 accelerator [25] that traces the cause of a fault, thereby reducing the downtime involved.

In classical terms, there has been a lot of concern regarding the reliability of particle accelerators that is apparent in published literature. The figure of merit for particle accelerators is high availability which is achieved by maximizing the reliability and minimizing the downtime periods [26] [27] [28] [29]. Diversified efforts are being employed to improve the availability of existing accelerators and design of new accelerators [30] [31]. The approach is generally based upon the direct analysis of operational data followed by the determination of weak links in the system such as failure prone components and inefficient procedures [28] [29] [20] [32] [33].

If operational or failure data is not available in adequate amount, or if the system interrelation dynamics have to be analyzed, a formal risk analysis methodology is used. According to [2], there are two categories of reliability evaluation techniques: analytical and simulation. Analytical techniques represent the system by a mathematical model and evaluate the reliability indices from mathematical solutions. Some of the popular models [34] are Failure Mode, Effect and Criticality Analysis (FMECA), Fault Tree Analysis (FTA), Reliability Block Diagrams (RBD), Markov Chain models and Petri-net based models. The simulation models, generally based on Monte Carlo technique, estimate the reliability indices by simulating the actual process and random behavior of the system. The method therefore treats the problem as a series of real experiments.

A series of reliability studies have been performed using these models for accelerator safety systems. An FMECA model [35] was developed for the reliability analysis of beam interlock system for CERN accelerators. An FTA [36] is done for the reliability evaluation of beam loss monitor system for LHC. RBD has been used for determining accelerator reliability in [37]. Markov models have been used in [38] for the dependability analysis of beam dumping system of LHC. In [39], an analytical model is developed for a general multistate system and is applied to the reliability prediction of quench protection system. A Monte Carlo simulation model is developed for LHC MPS [6] for calculating probabilities of system failures, and is compared with a mathematically equivalent model.

The work presented in this report includes both an analytical as well as a simulation approach. For the BPS, the lower level on the hierarchy is evaluated by mathematical models like FTA [40] as there are numerous components and the dynamics are simpler. The higher level has more complicated operational dynamics, thus a Monte Carlo simulation approach [41] is adopted. Combining the result of these studies with the historical failure data, a Bayesian reliability analysis [42] is done that provides the most informed inference about the reliability of system.

Another unique approach towards analyzing and improving the reliability has been adopted by using nonlinear system identification [43] and remodeling the inductive behavior of superconducting magnets [44], that is being used to detect the quenches. The dependence of inductance on the magnet current and current history is discussed in [45]. However, there is limited knowledge available on the magnetization phenomena and the *B*-*H* curves of magnetic materials [46]. Due to this indeterminate nature, holes and cutouts are used in RHIC superconducting

magnets' iron yoke to reduce the saturation induced effects [47]. Moreover, the inductance has to be modeled to an accuracy of +/-1mH for proper quench detection. The task of modeling saturation and hysteresis has been dealt separately in literature. Three flux linkage vs. current saturation models are compared in [48], which have pretty good fit to the data. For saturation modeling, [49] uses a 5th degree polynomial, however the analysis for RHIC quench detection data shows that limited degree polynomial does not give the needed accuracy. For the modeling of hysteresis Presaich model has been used, but it is difficult to parameterize the model for a certain magnet [50]. Hysteresis has also been modeled by using parallelogram and elliptical models [51] [52].

The following methodologies are being adopted for the MPS reliability analysis. The principles of Monte Carlo methods are explained in [53]. The concept of competing risks theory and elaborate details on exponential distribution is given in [54]. A more mathematical approach for competing risks is presented in [55]. The Markov state diagrams are elaborated in [56]. The RHIC, MPS, BPS and QDS details are given in [57] [4] [58] [59] [60]. The FTA has been studied from [61] [62]. The mathematics for quantitative FTA is described in [63]. The validity of exponential distribution to be used for electronic components is stated in [64]. The Bathtub curve is explained in [64] [2]. The component level failures are evaluated from [65] [66] [67] [68]. The nonlinear system identification techniques are elaborated in [69]. Statistical techniques used for the system identification have been referred from [70] [71].

1.4 The Relativistic Heavy Ion Collider

The RHIC [4] facility at the Brookhaven National Laboratory enables studies of nuclear phenomena in collisions of light and heavy ions, and polarized protons. It has been in operation since 2000. RHIC (Fig. 2) is a complex set of accelerators interconnected by beam transfer lines. The injector system can be operated independently of the collider. The main tunnel is connected to the Alternating Gradient Synchrotron (AGS) through the injection tunnels. The collider has support buildings, four experimental areas, and a cryogenic refrigerator system with the capacity to meet RHIC requirements. Fig. 2 shows all major components of the RHIC complex. RHIC collides two beams of positive ions head-on when they are travelling at 99.995% of the speed of light. The beams travel in opposite directions around RHIC's 2.4-mile storage rings that are hexagonally shaped. The six interactions regions are at the middle of the six relatively straight

sections, where the two rings cross, allowing the particles to collide. The beams are in the form of short bunches that are separated by 108 ns.

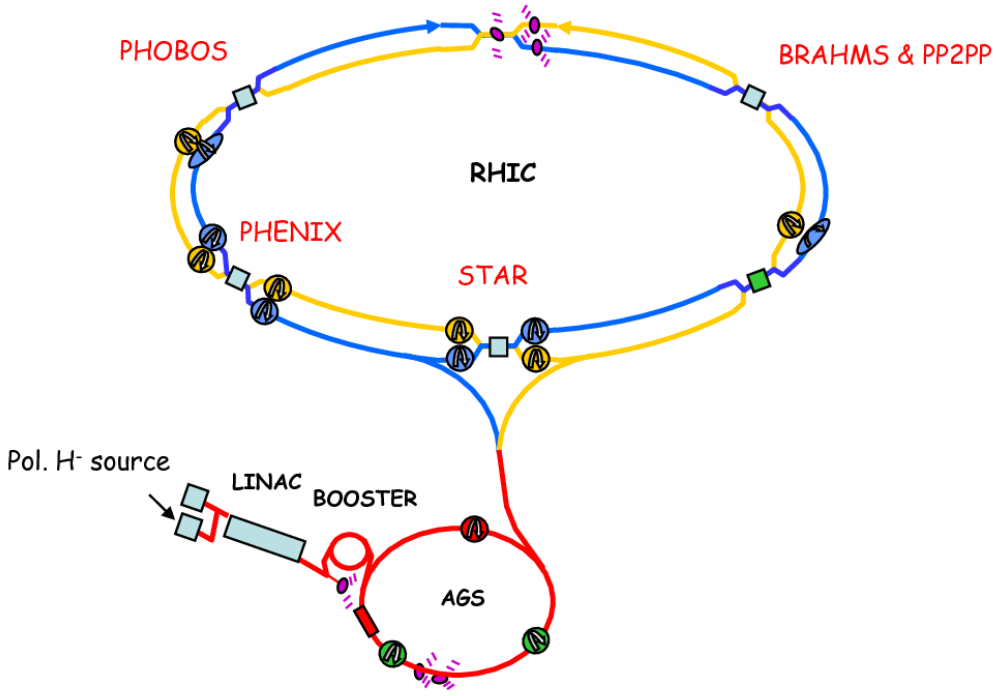

Figure 2: Relativistic Heavy Ion Collider

The research objectives of RHIC involve the study of collisions of heavy ion beams (e.g., beams of the nuclei of gold atoms) at energies up to 100 GeV/n, and polarized protons at energies up to 250 GeV. Since 2000, RHIC has provided hadron collisions with high luminosity to 5 experiments, STAR, PHENIX, PHOBOS, BRAHMS, and PP2PP [4]. In heavy ion operation a greater operational flexibility than at other hadron colliders is required. The particle species and collision energy are changed frequently. The heavy ion program has produced a number of striking results, including the discovery of a fascinating new form of matter. Unexpectedly, this extremely hot and dense matter, often referred to as the strongly interacting quark gluon plasma or sQGP, behaves more like a perfect liquid than an ideal gas. In polarized proton operation, both luminosity and polarization are important. The figure of merit for the experiments is either LP^2 or LP^4 where L is the luminosity and P is the beam polarization. RHIC can deliver vertically polarized beam to

all experiments, and longitudinally polarized beam to STAR and PHENIX. Currently the main goal of the polarized proton program is to reveal the source of proton spin.

Bending and focusing of the ion beams is achieved by the ring magnets [4]. RHIC employs relatively low-field superconducting magnets. At a magnetic field of 3.458 T, the beam energy is 100 GeV/n for fully stripped gold ions, and 250 GeV for protons. The required field is generated with single-layer cosine-theta magnets [72] which for maximum operational flexibility, are contained in vacuum vessels separate for each ring, except those near the collision points. The collider consists of two rings of superconducting magnets, namely dipole magnets for bending the beams, quadrupole magnets for focusing the beams and sextupole magnets for correcting the beam chromaticity. The main components of the magnet system are 288 arc-size dipoles and 108 insertion dipoles, and 276 arc and 216 insertion quadrupoles. In addition to dipoles and quadrupoles, there is an inventory of smaller magnets consisting of 72 trim quadrupoles, 288 sextupoles and 492 corrector magnets at each quadrupole. For polarized proton spin manipulations there are 24 superconducting helical magnets in each ring, grouped into 2 snakes and 4 spin rotators. The arc dipoles have a physical length of 9.728 m (9.45 m effective), are bent with a 4.85 cm sagitta and have a coil aperture of 8 cm in order to accommodate the requirements due to intrabeam scattering. The cold bore beam tube aperture is 69 mm in diameter. The beams in the arcs are 90 cm apart. The magnets are cooled to a temperature of <4.6 K by circulating supercritical Helium, which is supplied by a 24.8 kW refrigerator. The various ring magnets are excited by an appropriate power supply system and protected by a quench protection system. The beam tube in the superconducting magnets is at the temperature of liquid Helium. An extremely good vacuum with an equivalent warm pressure $<10^{-11}$ Torr is obtained, in the absence of leaks into the cold bore. In order to avoid the formation of electron clouds, beam loss and radiation background, a vacuum of about 7×10^{-11} Torr is required in the warm beam tube sections of the insertion regions. The cryostats for the superconducting magnets require a separate insulating vacuum of less than 10^{-5} Torr in order to avoid a heat load due to convection.

1.5 RHIC Machine Protection System

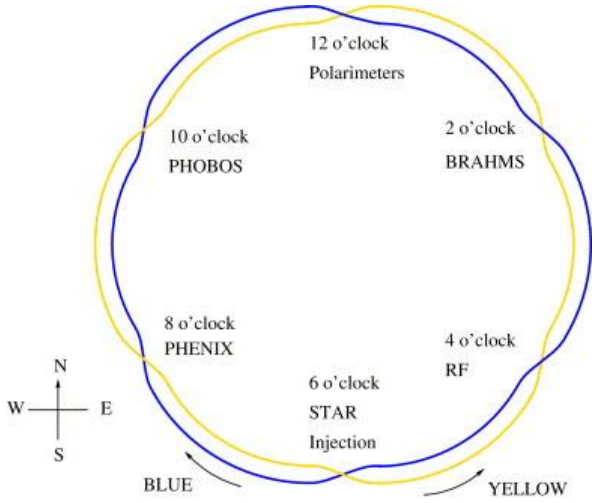

Figure 3: RHIC layout

The deviation from nominal operation of RHIC (Fig. 3) subsystems introduces risks that can lead to leakage of the enormous stored energy of 72 MJ. The stored energy components are summarized in Table 1. The magnet energy can leak in the form of heat at quenching magnets, generating enormous amount of pressure, and severe physical damage to the equipment. The beam energy if leaks can generate ionizing radiation that can damage equipment as well as can raise residual radioactivity.

Table 1: Stored Beam Energy Components

Component	**Stored energy**
Superconducting magnets	70 MJ
Ion beam per ring	350 kJ
Polarized proton beam per ring	900 kJ

The goal of MPS is to monitor the development of non-nominal conditions in the machine, and safely dispose the stored energy in such case. The MPS must protect the machine against damage due to beam losses and/or malfunctioning equipment. At the same time MPS must maximize the operational efficiency and minimize the time needed for interventions and maintenance. The

quantity to be optimized by MPS is the integrated machine performance. The main objectives of the MPS are:

1. Protect the machine equipment from damage by performing an emergency shutdown of the beams and magnets upon detecting signals, which indicate critical and non-nominal conditions.
2. Maximize the machine availability by avoiding false emergency shutdowns, leading to unnecessary machine downtime.

The operation of the collider and achievement of full performance requires continuous monitoring of many beam characteristics for which appropriate beam instrumentation is provided. A large number of support systems facilitate this, including

- Control system for allowing the control and communication among the various collider systems.
- RF system for providing a peak acceleration voltage of 300 kV to the beams
- Superconducting magnet system to generate a field up to 3.458 T for bending and focusing of beams
- Power supply system for supplying current to the superconducting magnets
- Cryogenic system for circulating liquid Helium to cool down the superconducting magnets below 4.6 K
- Vacuum system to maintain the pressure below 10^{-11} Torr to reduce beam interactions with gas molecules
- Beam loss monitoring system watches the leakage radiation coming out of the machine during the operation

Non-nominal conditions are detected with the help of many diagnostic devices installed along the ring. They survey the health of the support systems and the health of the beams. The health statuses are reported to the MPS on the system's current state and on the diagnostics results. Depending on the combined report from all sub-systems concerned, the MPS will perform an emergency shutdown of the beams/magnets or permit further operation.

A critical non nominal condition is a superconducting magnet quench. A quench is an abnormal termination of magnet operation that occurs when part of the superconducting coil enters the normal (resistive) state. This can occur because the field inside the magnet is too large, the rate of

change of field is too large, or due to radiation. The total current flowing in superconducting coils is 6000A. Even a tiny resistive zone can cause a concentrated energy dissipation resulting in hot-spot formation and melting of the coil. The MPS incorporates a Quench Detection System that detects the quenching magnets and generates a trigger to extract the current out of the superconductors.

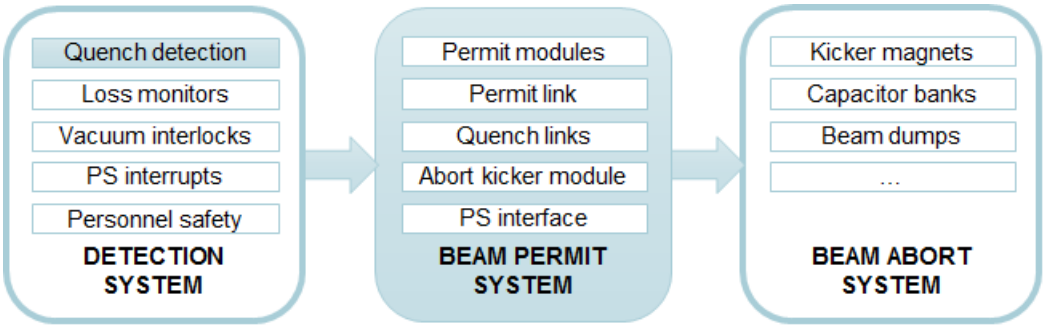

Figure 4: Machine Protection System

The MPS is divided into Detection System, Beam Permit System (BPS) and Beam Abort System (BAS) (Fig. 4).

- The Detection System consists of diagnostic devices that survey the health of support systems and beams, and provides inputs to the BPS called as *Permit and Quench Inputs*, often referred as input triggers.
- The BPS is the centralized safety system that observes these triggers and takes the decision for emergency shutdown or permits the operation. Depending upon the trigger, it commands a beam dump and/or a magnet power dump.
- The BAS receives the abort signal from BPS, and discharges a capacitor bank to kicker magnet coil to create a steering field for taking the beam out of the ring.

The two most vital parts of MPS are the BPS (due to its decision making power) and the QDS (detecting dangerous quench failures). Other parts of MPS are fairly passive. Next two sections explain the details of these two systems.

1.5.1 The Beam Permit System

The Beam Permit System [73] is a centralized safety system that inspects the accelerator support systems of RHIC to allow the beam entry and its existence in the machine, as shown in Fig. 5. It consistently monitors the health of support systems like power supplies, cryogenics, beam position monitors, beam loss monitors, access controls, quench detection, vacuum etc.

Upon sensing an anomaly, it takes action for the safe disposal of stored energy in beams and magnet current. This is done in two ways, namely a beam abort and a quench abort.

1. Beam Abort: The beams in the yellow and blue ring are taken out of the RHIC. The BPS sends signal to the beam abort system to dump the beams. The beams are then steered out of the ring using the kicker magnets. The beam dump signal has to be synchronized with the abort gap to avoid sweeping beams during the transition of kicker's magnetic field. The beam abort occurs when any support system health status is faulty.

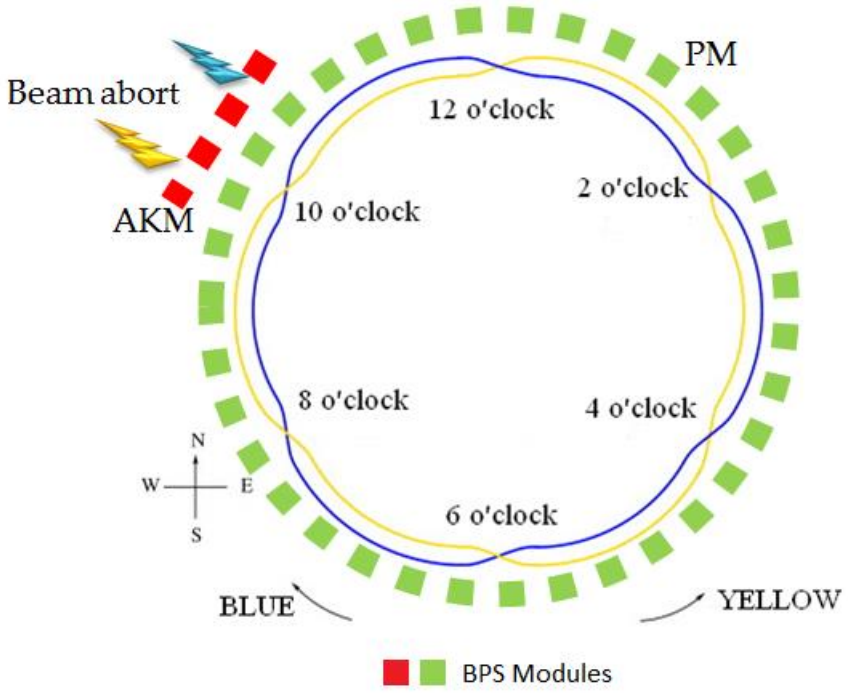

Figure 5: BPS modules around the ring

1. Quench Abort: In addition to the Beam Abort, the current in the superconducting magnets is extracted. This involves the emergency ramp down of the power supplies. The BPS drops the power supply interlock signals to power supplies connected at individual *PM* location around the ring. The quench abort occurs when the quench detection system reports a magnet quench.

The beam is aborted into an internal beam dump at the end of the storage period or in case of equipment malfunction. It is dumped in a single turn (13 μsec) by activating the abort kicker magnet, which deflects the beam horizontally onto a dump block. To compensate for the rise time of abort kicker magnetic field, an abort gap of 1 μs is provided in the beams. The BPS also connects to the power supply interlock system. There are separate blue and yellow magnet quench detection systems, which trigger both a beam dump, and power supply emergency shutdown. However, a magnet quench detection in one beam line does not affect the power supplies in the other beam line.

The building blocks of BPS are Permit Module (*PM*) and Abort Kicker Module (*AKM*), which incorporate various electronic boards based on VME specification. The BPS consists of 37 modules that are spread around the RHIC ring, shown in Fig. 6, first 33 being the *PMs* and the last 4 being *AKMs*. The *PM* concentrates health inputs from various support systems locally and has in-built intelligence to take decisions regarding safety. Abort Kicker Modules (*AKM*) send the beam dump signals to Beam Abort System, synchronised to the abort gap. There are two redundant *AKMs* for each beam.

The modules are connected by three fiberoptic links called the Permit Link, Blue Link and Yellow link. These links carry 10 MHz carrier signals whose presence allows the beam in the ring. The *PMs* generally are connected to each other through all the three links, whereas the *AKMs* only connect to the permit link. The health of the connected support systems is reported to other modules by maintaining the carrier outputs.

The support system health inputs [58] to the BPS can be classified as Permit Inputs (*PI*) and Quench Inputs (*QI*). *PIs* are the support system health inputs and *QIs* are the quench detector inputs. Taken together with the carrier inputs from previous *PM*, any input signal failure will cause its carrier output to terminate. If any support system *PI* fails, the permit carrier output terminates, initiating a beam abort. If *QI* fails, then the blue and yellow carrier outputs also terminate, initiating

a quench abort. The carrier failure propagates around the ring to inform other *PMs* about the occurrence of a fault.

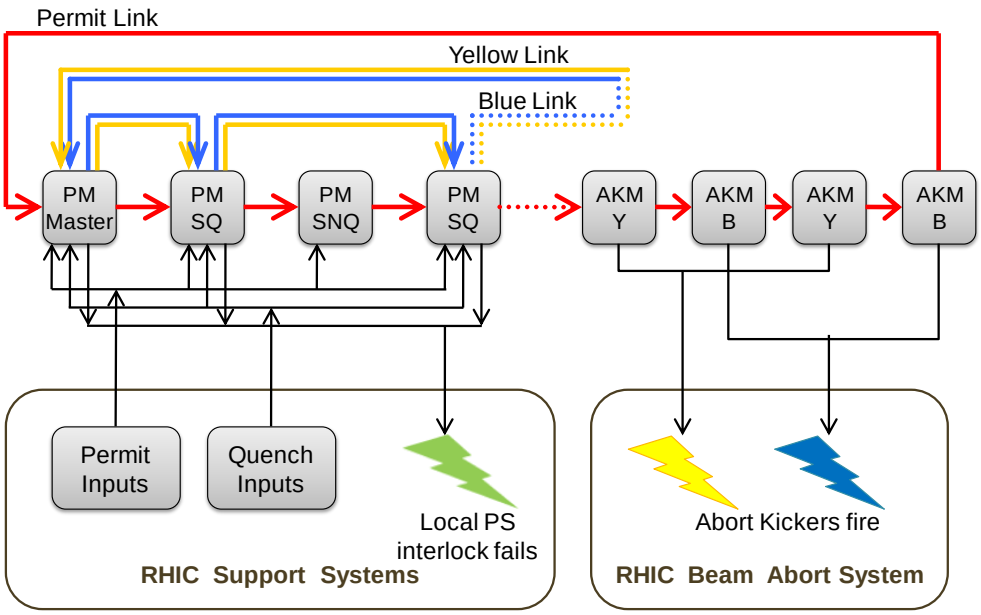

Figure 6: Beam Permit System

The carrier failure ultimately reaches the *AKMs*. The *AKMs* have the permit carrier input, but no health inputs from the support systems. They however have the carrier output and the beam dump output. If *AKMs* see a carrier failure, they wait for the beam abort gap, and then synchronize their dump output signal with the gap.

The beam permit system is also used to purge the beams at the end of the operation cycle.

Permit Module

Permit Module concentrates the support system statuses, and is responsible for taking actions to permit or abort the beam. There are in total 33 *PM* in the ring. Fig. 7 shows the general structure of the permit module, with various boards and components. The thin arrows are the carrier signals, the broad arrows being the permit & quench inputs.

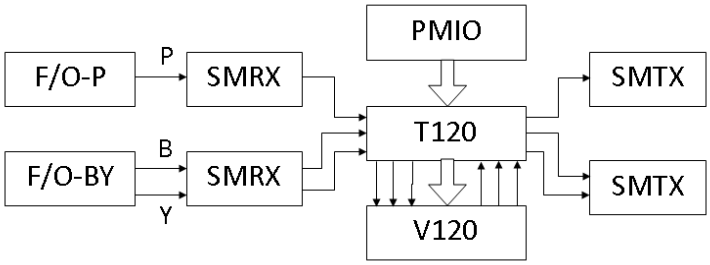

Figure 7: The Permit Module

1. T120 – It is the transition board for V120 through which all the carrier and trigger signals are interfaced to V120. The trigger signals are terminated in T120 and optically isolated in V120. The carrier signals are terminated and galvanically isolated in T120.
2. PMIO – The permit module input-output strip interfaces to the support system statuses and provide permit /quench inputs to the T120 board.
3. SMRX – Single mode fiberoptic receiver converts the carrier signals from optical to TTL. Every board has two channels, so it can accommodate maximum of two carriers. Two SMRX are used, one for permit link, and other for blue & yellow links
4. SMTX – Single mode fiberoptic transmitter converts the carrier signals from TTL to optical. Every board has two channels, so it can accommodate maximum of two carriers. Two SMTX are used, one for permit link, and other for blue & yellow links
5. F/O – P – These are the fiberoptic cables with in-between connectors to previous *PM* for permit link. All the cables and connectors connected 'before' a *PM* are included in the analysis of that *PM*.
6. F/O – BY – These are the fiberoptic cables with in-between connectors to previous *PM* for blue & yellow links. All the cables and connectors connected 'before' a *PM* are included in the analysis of that *PM*. This contains two sets of cables and connectors.

There are four variants of the *PM* as shown in Table 2. The configuration of the boards V120, T120 and PMIO decide the *PM* variant.

Table 2: BPS module variants

Modules	Number
Permit Module: Master (*PM:M*)	1
Permit Module: Slave with Quench detection inputs (*PM:SQ*)	13
Permit Module: Slave with No Quench detection inputs (*PM:SNQ*)	18
Permit Module: Slave without any support system input (*PM:S*)	1
Abort Kicker Module (*AKM*)	4

1. *PM:M* – The Master *PM* generates the three 10 MHz carriers and transmits it to the next slave module. The slave *PMs* receive the carriers and depending upon the input trigger statuses, retransmit the carriers.
2. *PM:SQ* – It is a slave module with both permit and quench inputs. It contains all the three carriers. Consequently, it is able to take action for both beam abort and quench abort.
3. *PM:SNQ* – It is a slave module with only permit inputs. It contains only the permit carrier. Consequently, it is able to take action only for beam abort.
4. *PM:S* – It is a slave module without any input triggers. It contains only the permit carrier. It only monitors the permit carrier and cannot take any action.

Figure 8: The Abort Kicker Module

Abort Kicker Module

The Abort Kicker Module consists of a single board called V125 as shown in Fig. 8. The V125 board contains the control logic that issues abort signals to beam abort system of RHIC. After an *AKM* receives permit carrier failure, it waits for the beam revolution fiducial (an indication for the abort gap) and generates the beam dump signals. If it doesn't receive the fiducial within 32 μs (2.5

beam revolution), the dump signals are sent asynchronously. For the reliability analysis the fiberoptic components connected before an *AKM* are considered in its analysis.

1.5.2 The Quench Detection System

The RHIC superconducting magnets store 70 MJ of peak energy in the form of 6000A of magnet current. In event of a quench [74] this energy can be dissipated in a very small region resulting in the melting of magnet coil and sudden evaporation of liquid Helium which can create dangerous explosive pressures. The RHIC quench detection system [4] [59] [60] monitors various types of superconducting magnets, shunt bus and gas cooled leads continuously to sense the magnet quenches and the gas cooled lead faults. The method to detect quench is by voltage sensing, as shown in Fig. 9. When a quench is determined, the system sends a quench signal for the power supplies to shut down and energy extraction system to operate, thus protecting all essential parts of the RHIC magnet circuit. This signal is fed to the BPS as a quench input trigger.

The QDS is a distributed system separated into twelve subsystems. Each subsystem is a standalone unit that processes its data locally. All subsystems are networked together via the Ethernet, as shown in Fig. 10. Each subsystem is divided into three functional sections. The front-end computer section, ADC/timing-control section, and the low level hardware interface section.

- The front-end computer section consists of a VME Crate controller, a Utility card, a Delay card and a DSP card.
    - Crate controller communicates with the Control System, downloads programs and parameters, upload stored data to users and initialize other VME modules.
    - The Utility card extracts Magnet Currents from the Real Time Data Link (RTDL) and passes them to the DSP card.
    - The Delay card decodes events from the Event Link and synchronizes the Quench Detection System to the 720Hz master clock at the Control system.
    - The DSP card reads the magnet currents from the Utility card, current readback from the 4-to-20 mA card, and the magnet voltage taps signals from the ADC card.
- The ADC/timing-control Card generates a simultaneous sample-and-hold signal to all low-level interface cards

The low-level interface analog cards are Dual Gain Mux Card, Single Gain Mux Card and Digital Output Card that accommodate different input signals, like tap voltage, power supply current etc.

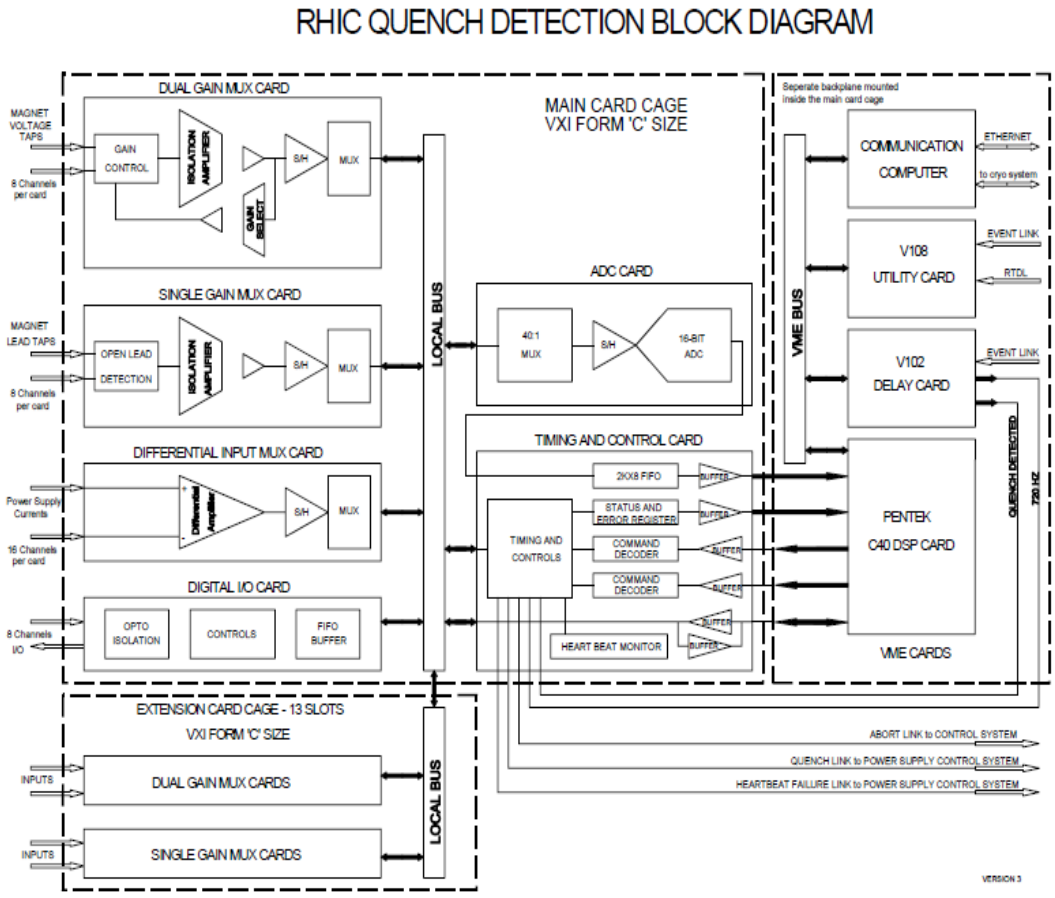

Figure 9: Quench Detection System Block Diagram

Quench detection model

If a magnet quench occurs, the quench detectors are responsible for detecting this state and trip the quench link before a magnet is damaged. The logic for quench detection resides in a DSP board. The function of the DSP card is to read the magnet currents from the Utility card, current readback from the 4-to-20 mA card, and the magnet voltage taps signals from the ADC card once every 1.389ms. Noise component of 60Hz is removed by averaging twelve acquired samples.

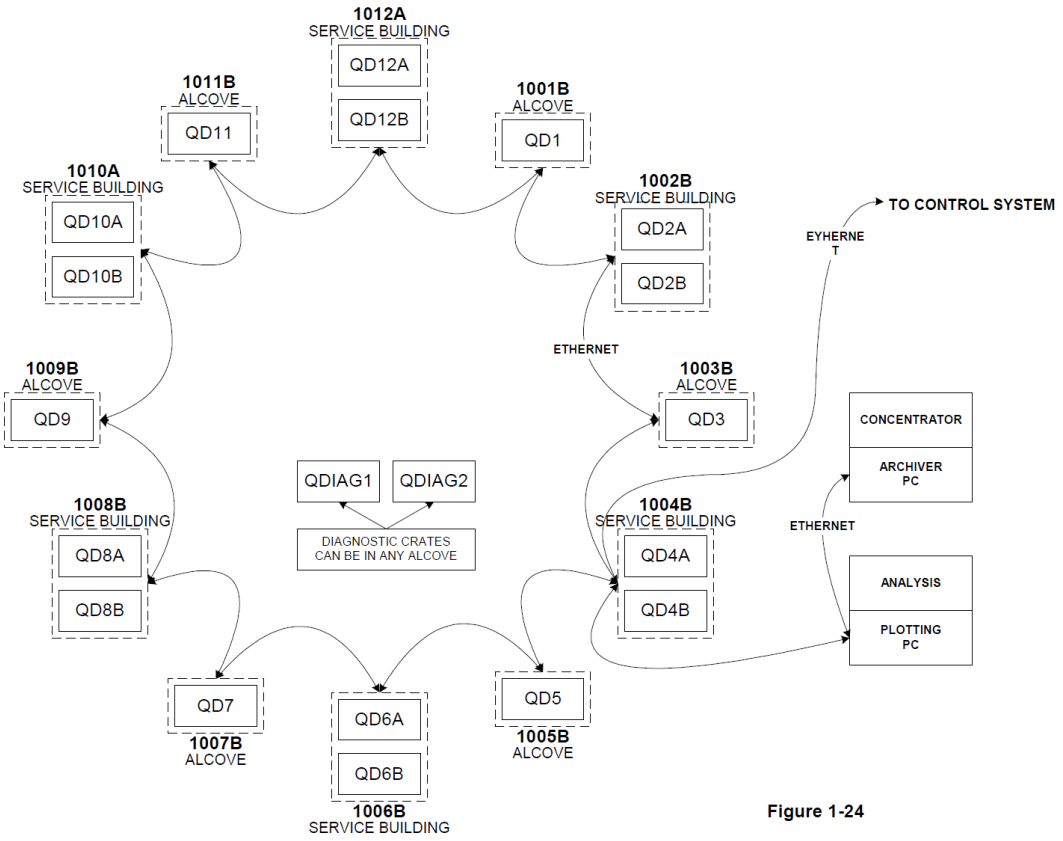

Figure 10: Quench Detection System Layout

Fig. 11 shows the superconducting magnet coil and the gas cooled leads. The magnet is purely inductive when it is in the superconducting state and has a zero resistance. Voltage taps are used to measure the voltage across the magnets, whose leads pass through both the cold region and the warm region, and have an associated resistance. Thus voltage during nominal condition across the tap is

$$V_C = L\frac{di}{dt} + Ri$$

where i is the current through the magnet, L is the inductance of the magnet and R is the lead resistance. The DSP has lookup tables which store the values of L and R, and i is measured from the power supply. It calculates the ideal voltage across the tap from these values as V_C. This voltage is continuously compared to the actual voltage across the tap. When a magnet quenches, a resistance develops on the magnet and the difference between voltages exceeds. Table 3 shows the quench detection thresholds with the sustaining time so as to qualify as a quench.

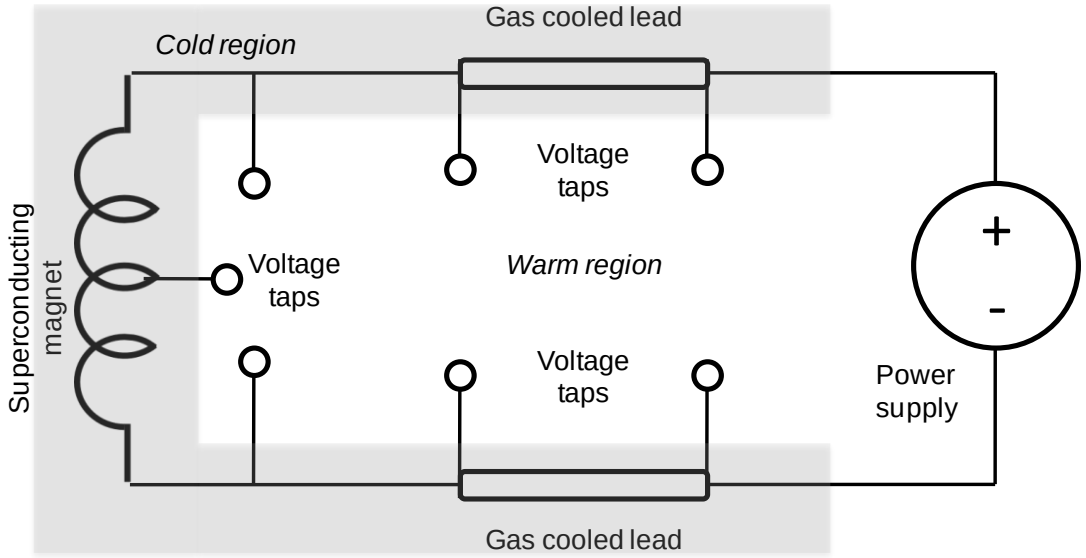

Figure 11: Superconducting magnet and voltage taps

The gas cooled leads carry the current from power supply to the magnet. They have negligible resistance or inductance. The quench here is determined by comparing the readback voltage to a fixed threshold value. If the voltage difference of the magnet or the gas cool lead readback voltage is outside the window specified by Table 3, quench is determined. The DSP card then sends a quench signal to the *QI* of the *PM* via the ADC card to shut down power supplies and activate the energy extraction system. The energy extraction system extracts stored energy from the entire series-connected string of magnets as rapidly as possible to protect buses and diodes from overheating.

Table 3: Quench Detection Thresholds

Voltage difference	Time delay (sec)	Quench event
0 – 24 mV	-	No quench
25 – 50 mV	1.667	Quench
51 – 250 mV	0.3333	Quench
0.251– 1.25 V	0.0835	Quench
> 1.25 V	0.0167	Quench

Chapter 2

Stochastic Reliability Model of Beam Permit System

The RHIC BPS monitors the health of RHIC subsystems and takes active decisions regarding beam-abort and magnet power dump, upon a subsystem fault. The reliability of BPS directly impacts the RHIC downtime, and hence its reliability and availability. This chapter elaborates the assessment of the probability of BPS failures that could lead to substantial downtime, based on survival data obtained from the military handbook [65] and manufacturer supplied failure data for components. A fail-safe condition imparts downtime to restart the machine, while a failure to respond to an actual fault can cause potential machine damage and impose substantial downtime.

The building blocks of BPS are *PM* and *AKM*, which incorporate various electronic boards based on VME specification. This chapter first presents a quantitative FTA [40] of the *PM* and *AKM*, yielding the failure rates of three top failures that can potentially cause significant downtime of the machine. The FTA helps tracing down the top failure of the module to a component level failure (such as an IC or resistor). The fault trees are constructed for all module variants and are probabilistically evaluated using an analytical solution approach. The component failure rates are calculated using manufacturer datasheets and military handbook. The apportionment of failure modes for components is calculated using FMD-97 [66]. This analysis helps understand the importance of individual components regarding the reliability of BPS, and evaluate their impact on the operation of BPS.

Subsequently, the chapter illustrates a stochastic multistate reliability model [41] of the BPS that simulates the functional behavior and interaction of the BPS modules. The BPS modules have exponential lifetime distributions, where the failures rates are calculated from above mentioned FTA. The model is based on the ‘competing risks theory with crude lifetimes’ in which multiple failure modes compete against each other to cause a final failure, and simultaneously influence each other. The model is also dynamic in nature as the structure of the BPS model varies based on the fault trigger location. The model is implemented as a Monte Carlo simulation in Java. This analysis helps quantify the probabilities of the BPS system level failures.

2.1 Failure Modes

BPS malfunction can be potentially detrimental to RHIC equipment. This section elaborates about the failure modes of the BPS modules. These failure modes could translate into BPS system level failure modes that compromise the availability and safety of RHIC. A fail-safe condition occurs when a trigger is generated within the module that causes the carrier termination. This is a *false* failure of the BPS module. When a carrier termination or an input trigger is ignored by a module, and it maintains the carrier output, it is called a *blind* failure of a BPS module.

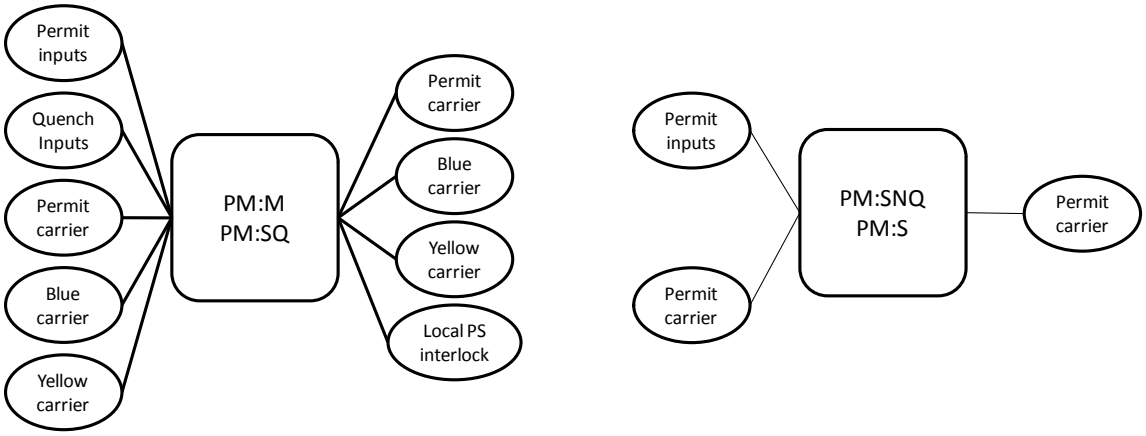

Figure 12: Inputs and Outputs of Permit Module

The state of BPS at any given time depends upon the state of its components i.e. *PMs* and *AKMs*. Fig. 12 shows the block diagram of variants of *PM* (section 1.5.1) with its inputs on the left and outputs on the right. The *PM* can fail in following three failure modes:

1. False Beam Abort (*FB*): The electronic components in the input signal path for the permit inputs or the permit carrier fail within the *PM*. This terminates the permit carrier output initiating a beam abort.
2. False Quench (*FQ*): The electronic components in the input signal path for the permit inputs, quench inputs, permit carrier, blue carrier or yellow carrier fail within *PM*. This terminates its permit, blue & yellow carrier outputs initiating a quench abort.
3. Blind (*B*): The electronic components within the *PM* fail in such a way that real fault in any of the inputs is ignored. This maintains its carrier outputs in spite of a real failure.

The variants *PM:SNQ* and *PM:S* do not have the *FQ* failure mode as there are no quench inputs or blue/yellow carriers.

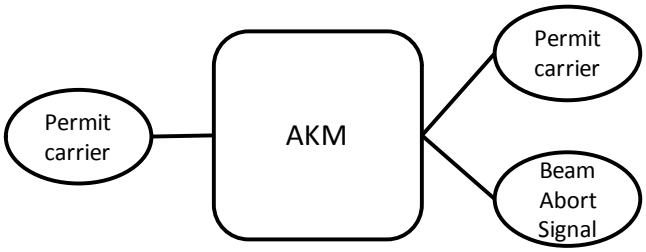

Figure 13: Inputs and outputs of *AKM*

Fig. 13 shows the block diagram of *AKM* with its input on the left and outputs on the right. The *AKM* can fail in the following three failure modes:

1. False Beam Abort (*FB*): The electronic components in the input signal path for permit carrier fail within the *AKM*. This terminates its permit carrier output and generates beam dump signal.
2. Blind (*B*): The electronic components within the *AKM* fail in such a way that the permit carrier failure is seen but the beam dump signal is not generated.
3. Dirty Dump (*DD*): The electronic components within the *AKM* fail in such a way that it cannot synchronize the dump signal with the abort gap, and the beam is swept across the equipment.

Depending on the above failure modes of the BPS modules and their functional dynamics, BPS itself can undergo the following system level states:

1. System No Dump *(SND)*: No trigger arrives that demands the action of BPS
2. System Good Dump *(SGD)*: Input trigger arrives at a module, and causes a beam abort or quench abort.
3. System False Beam Abort Failure *(SFD)*: False trigger generated within a module causes the beam abort.
4. System False Quench Failure *(SMD)*: False trigger generated within a module causes quench abort.
5. System Blind Failure *(SBD)*: Any trigger is blocked in its way, which results in ignored beam abort (or quench abort).

6. System Dirty Dump Failure *(SDD)*: During a beam abort or a quench abort, an AKM failed in *DD* mode in the path, causes the beam to sweep across the equipment.

Significant downtimes are imposed by the *SFD, SMD* and *SBD* failures. The false failure furnishes a downtime to power-up and re-initialize the whole machine. The blind failure represents a failure to respond to an emergency. It is in fact far more dangerous than the false failure as it can actually cause damage to the RHIC sub-systems, inflicting downtime of several months. The *SDD* failure increases the radiation levels inside the machine. All these failures affect the reliability and availability of RHIC.

2.2 Reliability Theory

Definition of Reliability: The reliability [54] of an item is the probability that it will adequately perform its required function for a specified period of time under stated conditions.

Generally, there has been a confusion in distinguishing between a "hazard" and a "risk" [2]. Hazard can be ranked in terms of severity of events, but does not take into account their likelihood. Risk accounts not only for the hazardous events, but also for their likelihood. Reliability evaluation techniques help in the assessment of probabilistic risks that account for severity as well as likelihood.

The variable of interest in reliability evaluation is the system lifetime, which depends upon its components' lifetimes. The lifetimes are related to the Hazard Rate or Failure Rate, which represents number of failures per unit time. The Bathtub curve for hardware systems in Fig. 14 [2] [64] represents a hazard function in failures per unit time as $\lambda(t)$ vs. time. Three phases of life of a product are defined, a higher but decreasing rate of failure at the beginning of the product life, a lower failure rate throughout most of the usable life of the product, and an increasing failure rate toward the end of the usable lifetime.

The failures in the useful life period are random intrinsic failures and this portion has a constant hazard function with $\lambda(t) = \lambda$. The constant hazard rate corresponds to an exponential failure probability distribution function. This exponential distribution provides a good model for an item that is just as likely to fail at any time, regardless of it being new or old. For this reason, the exponential distribution is often used to model electronic components [64] that typically do not

wear out until long after the expected life of the product in which they are installed. Here a used item that is functioning has the same failure distribution as a new item. This property is called the memory-less property.

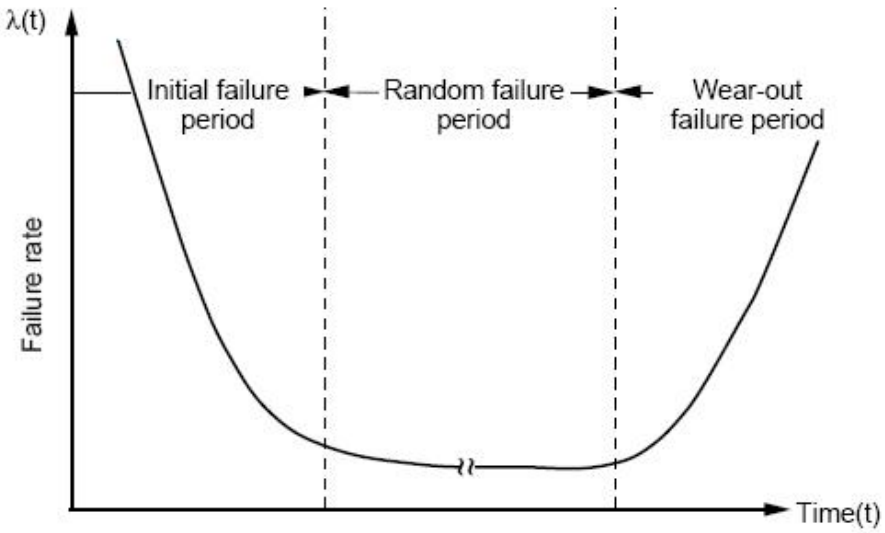

Figure 14: Bathtub Curve for Hardware Reliability

Fig. 15 shows the failure probability density function *f(t)*, the cumulative failure distribution function *F(t)*, the survival function *S(t)* and the hazard function *h(t)* for an exponential distribution [54] with parameter failure rate parameter $\lambda = 2$ and the time of observation as *t*.

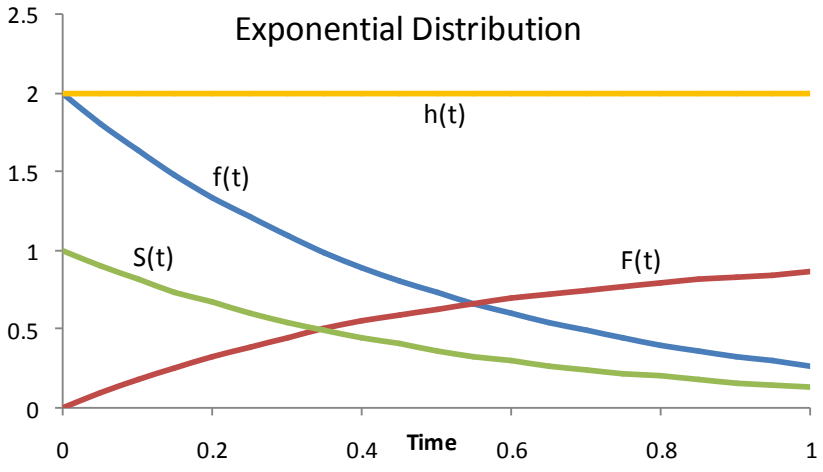

Figure 15: Exponential Distribution for λ = 2

Probability density function $f(t) = \lambda e^{-\lambda t}$

Hazard function $h(t) = \lambda$

Probability distribution function $F(t) = 1 - e^{-\lambda t}$

Survival function $S(t) = e^{-\lambda t}$

2.3 Quantitative Fault Tree Analysis

Fault Tree Analysis [61] [62] [40] is a deductive method that aims at resolving an undesired event into its causes. It involves the translation of a physical system into a structured logic diagram, in which certain specified causes lead to one specified event of interest, called the *top* event. The *top* events are generally catastrophic system states that can result from sub-system faults. The event is then resolved into its immediate, necessary and sufficient causal events, and related by appropriate AND and OR logic. The process is followed until the elementary causes are identified. FTA exhaustively identifies causes of a failure and quantifies the failure probability and contributors. It is used to assess a proposed design for its reliability or safety. Fig. 16 shows an example of FTA.

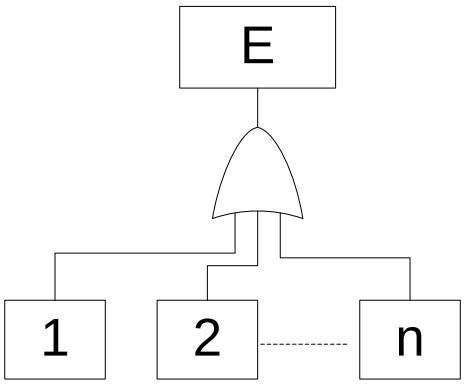

Figure 16: Fault Tree Example

$$S_E(t) = \prod_{i=1}^{n} S_i(t) = \prod_{i=1}^{n} e^{-\lambda_i t}$$

$$\lambda_E = \sum_{i=1}^{n} \lambda_i$$

Here

$S_E(t)$ = survival function of event *E*

i = index for basic events

λ_i = failure rate of event *i*

n = total number of basic events

λ_E = failure rate of event *E*

Since there are no redundant components that have to fail at the same time to cause a higher-level failure, this analysis has fault trees that only contain the OR gates. In this case, the *top* failure will be exponential if all the individual component failures are exponential. Common cause failures are not considered in this analysis thus making all the elementary failures statistically independent.

2.3.1 FTA Implementation for BPS modules

Fault trees [40] have been constructed for the variants of *PM* and *AKM* for their earlier discussed failure modes of *FB*, *FQ*, *B*, and *DD*. These are the *top* failures. The levels of hierarchy in trees represent various stages of detail and the number of levels depends upon the constituent boards and their complexity. At the board level, the circuit is divided into signal paths through which particular inputs and outputs relate to a *top* failure. There are some paths which are common to multiple *top* failures. In such a case, the failure rates are divided among them. As all the trees are composed only of OR gates, the *top* failure rate is a summation of the involved basic component failure rates.

While FTA is very good at showing how resistant a system is to multiple initiating faults, it is not good at finding all possible initiating faults. To ensure this, a lowest level FMEA (Failure

Mode and Effect Analysis) is performed. FMEA is an inductive approach in which individual failure modes of a component are considered, and possible progressions to a system level fault are identified. Here, a single level FMEA is done for all the board components, which defines the immediate consequence of each of their failure modes. This ensures that none of the failure mode of a component is left unexamined. An FMES (Failure Mode Effect Summary) is then prepared which serves as an interface between FTA and FMEA.

Component Failure Rate Prediction

The exponential failure rates for basic component failures are obtained from various sources. The failure rates for the newer components are obtained from the manufacturer datasheets. For older components, military handbook [65] is used. It is a military standard that provides failure rate data for many military and commercial electronic components. It is the most widely known and used reliability prediction handbook. The failure rate is calculated by using the "Part Stress Analysis" method which takes into account the actual operating conditions such as environment, temperature, voltage, current and applied power levels. An environmental factor of G_b and an ambient temperature of 30°C are used throughout. For some of the fiber optic components, the SR-332 handbook [68] is used.

Component Failure Modes Prediction

Quantification for the relative probability of occurrence for each potential failure mode for a component is essential to perform an FTA or FMEA. The FMD-97 [66] provides a cumulative compendium of failure mode data, which lists apportionments of all the tested failure modes. It can be used to apportion a component's failure rate into its modal elements, by multiplying the failure rate to the given failure mode percentage. The normalized distribution data from FMD-97 is used here, which excludes the non-inherent failures like workmanship errors and externally induced errors. Failure mode apportionments for a few components were made available by the manufacturer. The usual failure modes for electronic components are open circuit, short circuit, leakage, functional failure, drift, cracks, voids etc. [66]

Component Contribution to FTA

After preparing FMES, only those component failure modes are passed to FTA that contribute to the *top* failures. These components (or failure modes) are active for real-time BPS actions

(decision to drop carriers). They can be broadly classified into logical devices, terminations, voltage regulation, drivers, receivers, buffers, isolators, PLLs, connectors etc. Following are the considerations for the contribution to *top* level failures:

- Some components are common to all the carrier paths. A malfunction here will affect all the three carriers causing an *FQ*. If the common circuit is in *PM:SNQ*, then it will cause an *FB*.
- A component is ignored if it is:
    - active only during initialization
    - active only after beam-abort
    - used for diagnostics (LEDs, testing ports)
    - has a zero failure rate
    - inactive in a certain board variant
- A failure mode is ignored if:
    - it has an unknown consequence
    - it is an early life failure mode
    - it is a parametric failure.

2.4 Monte Carlo Simulation

Monte Carlo simulation [53] is a broad class of computational algorithms that relies on repeated random sampling to obtain numerical results, and is especially useful for simulating systems with many coupled degrees of freedom. This section illustrates a modular multistate reliability model of the BPS functional behavior, with the modules having exponential lifetime distributions. The model is based on the *competing risks theory with crude lifetimes*, where multiple failure modes compete against each other to cause a final failure. The model is implemented as a Monte Carlo simulation in Java.

2.4.1 Markov State Diagrams for the BPS Modules

The state of BPS at any given time depends upon the state of its components i.e. *PMs* and *AKMs*. The *PM* can fail in three modes namely a *FB*, *FQ* and *B*, which have three independent failure rates as λ_{FB}, λ_{FQ} and λ_{B}. The *AKM* can fail in three modes namely *FB*, *B* and *DD*, which

have three independent failure rates as λ_{FB}, λ_B and λ_{DD}. Theses failure rates are calculated from FTA in section 2.3. Fig. 17 shows the Markov state diagrams for *PM*, *AKM* and input triggers. The input triggers *PI* and *QI* are modeled as Poisson variables. Their time of arrival is also exponentially distributed.

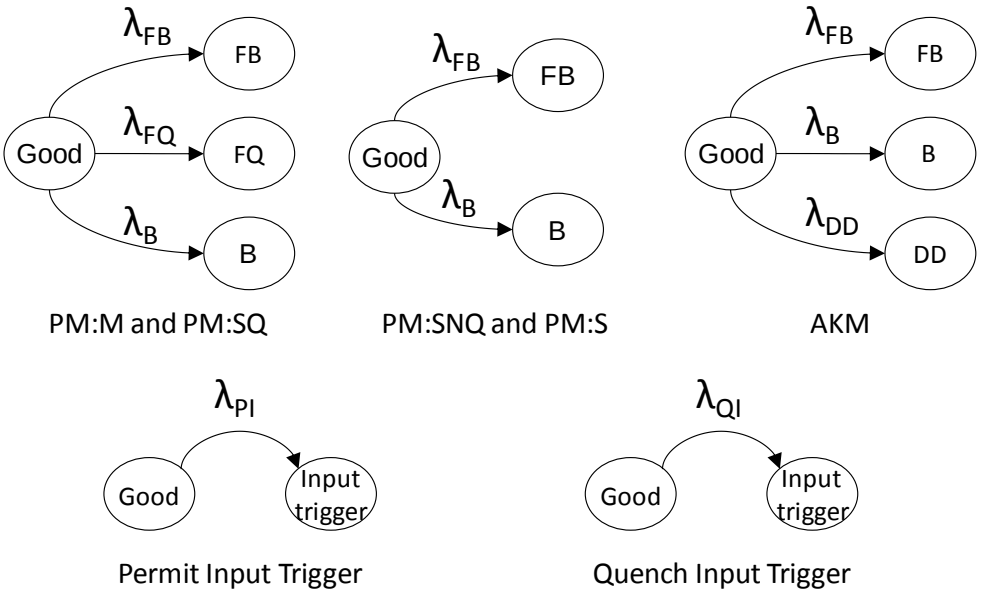

Figure 17: Markov diagrams for BPS modules

2.4.2 Competing Risks with Crude Lifetimes

In competing risks theory [55] [54], several causes of failure or risks compete for the lifetime of an item. The observed outcome comprises of the time of failure *T*, and the mode of failure *C*. Thus the basic probability framework here is a bivariate probability distribution, where *T* is a continuous random variable and *C* is a discrete random variable. Here *T* can assume continuous values between $[0, \infty)$ and *C* assumes discrete values as $\{1, 2... k\}$.

While considering crude lifetimes, each risk is viewed in the presence of all other risks. The lifetimes are analyzed as if all risks are simultaneously acting on the item under examination. A *net lifetime* approach has been previously used in [6] for Monte Carlo simulation of LHC machine protection where all the risks are viewed individually.

The BPS modules are subjected to $j = \{1, 2... k\}$ risks. The hazard rate for j^{th} risk if viewed individually is λ_j. T is the time of failure and t is the time of observation. The crude probability distribution function of risk j is given by

$$F_j(t) = P[0 < Tj < t, Tj < Ti \ \forall \ i \neq j | T > 0]$$

For exponentially distributed T:

$$F_j(t) = \frac{\lambda_j}{\sum_i^k \lambda_i} \left(1 - \ e^{-(\sum_i^k \lambda_i)t}\right); j = 1, 2.., k$$

The probability of failure from risk j is given by

$$\pi_j = \lim_{t \to \infty} F_j(t) = \frac{\lambda_j}{\sum_i^k \lambda_i} ;$$

$$\sum_j^k \pi_j = 1$$

The overall survival function $S_T(t)$ is the probability distribution of survival from all the k risks given by

$$S_T(t) \ = \ e^{-(\sum_i^k \lambda_i)t}$$

For permit modules:

$j = \{FB, FQ, B\}$ for *PM:M* and *PM:SQ*

$j = \{FB, B\}$ for *PM:SNQ* and *PM:S*

For abort kicker modules:

$j = \{FB, B, DD\}$.

For input triggers, $F_j(t)$ can be viewed as the probability of trigger arrival with $j = \{PI\}$ for permit input trigger and $j = \{QI\}$ for quench input trigger. For details on the derivation of these formulae, refer to Appendix A.

2.4.3 The Model

As opposed to the circular configuration of BPS, the Monte Carlo model is cut-out to a linear configuration, starting from the *PM:M* to the last *AKM*. There are two types of states of a module: active and passive. The *false* and *input arrival* are active states that upon inception propagate carrier failure in BPS, and are considered as triggers. The *good* and *blind* states are passive states, which do not propagate any carrier failure, and the module waits in that state.

Inverse Transform Sampling

A two-dimensional random variable has to be generated for simulating a bivariate distribution of *T*. Smirnov transform [75] states that if U_1 is a uniformly distributed random number, and *T* has a cumulative distribution function *F*, then the random variable $F^{-1}(U_1)$ also has a cumulative distribution function equal to *F*. Thus *T* can be generated as $T = F^{-1}(U_1)$ by using computer generated pseudo-random number. The continuous random variable *T* of the bivariate distribution is

$$T = \frac{-1}{\sum_j^k \lambda_j} \ ln\, U_1$$

The discrete random variable *C* that represents the cause of failure due to risk *j*, is generated by using the following equation with another pseudo-random number U_2

$$C = \begin{cases} 1, & 0 \le U_2 \le \pi_1 \\ 2, & \pi_1 < U_2 \le \pi_1 + \pi_2 \\ \ldots & \\ k, & \pi_1 + .. \pi_{k-1} < U_2 \le 1 \end{cases}$$

The above equations for *T* and *C* together generate the bivariate distribution of a module's lifetime.

Simulation Flow

The simulation has individual competing risks models for all the BPS modules. Each iteration starts with generating exponentially distributed random lifetimes given by above equations of *T* and *C*, and the time and mode of failure for each module are recorded. The maximum observation time of simulation is 6 hours, equal to the average store length of RHIC. Thus, all times of failure larger than this are rejected. The arrival of the first trigger (either an input or false) freezes the system state, and the BPS operation is emulated to find the overall system state. The iterations are

repeated until the failure probabilities are constant up to 4 decimal places. The system state is reset after every iteration.

The model is dynamic in nature, i.e. the number of components varies according to the location of trigger. The components before the trigger location are removed from the model.

The simulation is started with the assumption that the system is initialized and beam is established. The simulation stops at the arrival of a trigger. The values of λ for different modules are calculated by FTA. The input trigger rates are calculated from the RHIC historical operational data.

Special Cases

There can be some special cases where the simulation has to be designed specifically to address those issues. For instance, the *PM:SNQ*s do not have the blue and yellow links connected to them. Thus if there is a *PM:SNQ* between two *PM:SQ*s, two paths exist between the *PM:SQ*s. One is through the permit link & *PM:SNQ*, another one through the blue and yellow link. If this *PM:SNQ* goes blind, the carrier failure is still propagated through the blue & yellow links. Thus *PM:SNQ* is bypassed in this case.

In another case, one module can attain only one failure state. After acquiring a state, transition to other state is not possible. However, there can be multiple failed modules in the system at any given time. The false failure propagation can be hindered by a module sitting in blind state. This case is counted in *SBD* failure. More than one trigger can occur at an instant. In such case, the trigger nearest to the *AKMs* is considered. There can be blind modules in the system, but the run ends without the arrival of a trigger. This case is counted in no dumps.

Furthermore, consider next two cases. First, due to multiple blind *AKMs*, only one of the blue or yellow beams is aborted. This case is called a partial dump. Second, power supply interlock failure mode of *PM*, where the beam is maintained but magnet power is dumped. These two cases eventually result in false failures due to beam loss. They are counted in false failures.

2.5 Results

2.5.1 Quantitative Fault Tree Analysis

Fig. 18, Fig. 19 and Fig. 20 show the logarithmic bar charts of *top* failure rates of *PMs* and *AKM* for their variants. The horizontal axis shows the location indices of modules in the ring. The vertical axis shows the failure rate expressed in terms of FIT [67] that is equal to the number of failures expected per billion device-hours of operation.

The failure rates for *PM* are shown for top failure modes as *FB*, *FQ* and *B*. In Fig. 18, the 0^{th} module is *PM:M* and all other are *PM:SQ*. False failures are failsafe conditions that impart downtime to restart the machine. The false failure rates λ_{FQ} and λ_{FB} are mainly contributed by the fiber optic elements like cables, connectors, receivers and transmitters, which have failure rates of the order of 10^2 FITs. Among the three, the λ_{FQ} is highest of all as it has fiber optic elements for two links, blue and yellow. Here the λ_{FB} is approximately half of the λ_{FQ} because it has fiber optic elements for permit link only. The λ_{FB} for *PM:M* is very low as does not have any fiber optic elements connected. Blind failure is a fatal failure that can cause serious damage to equipment. The λ_B is about an order of magnitude less than other two, and is essentially contributed by the optocoupler malfunction in the V120 board. The optocouplers isolate the permit and quench input signals from the power ground. In Fig. 19, the 24^{th} module is *PM:S* and all other are *PM:SNQ*. As seen, there is no *FQ* mode here because there are no quench inputs or blue/yellow carriers connected. The λ_{FB} is higher than in Fig. 18 which represents that the fault in common circuits for carriers will cause an *FB* rather than an *FQ*. The λ_B is slightly lower than that in Fig. 18, as quench inputs are absent and corresponding optocouplers are ignored for the analysis.

The failure rates for *AKM* are shown for top failure modes as *FB*, *B* and *DD* in Fig. 20. The λ_{FB} is very small for all modules except the 33^{rd} as it has fiberoptic elements connected. The λ_B is almost equal to that of *PMs*, and is largely contributed by oscillator malfunction and power failures on-board. The λ_{DD} is also similar to the λ_B, largely contributed by oscillator malfunction and power failures on-board. The *DD* failure increases the residual radiation in the machine, but is less critical than a false or a blind failure.

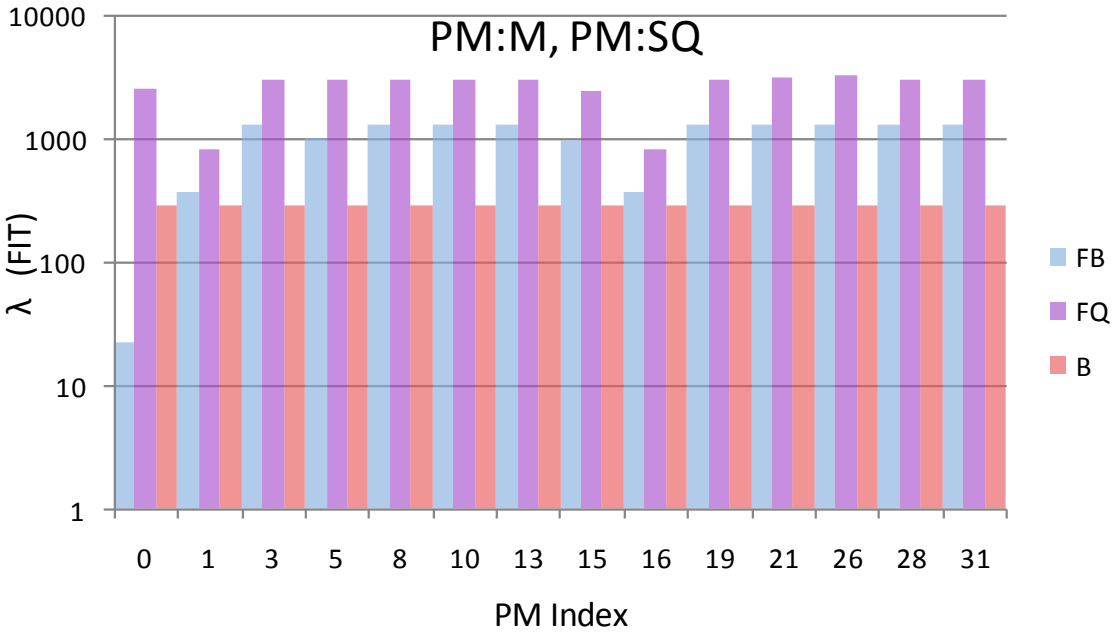

Figure 18: *PM:M* and *PM:SQ* failures

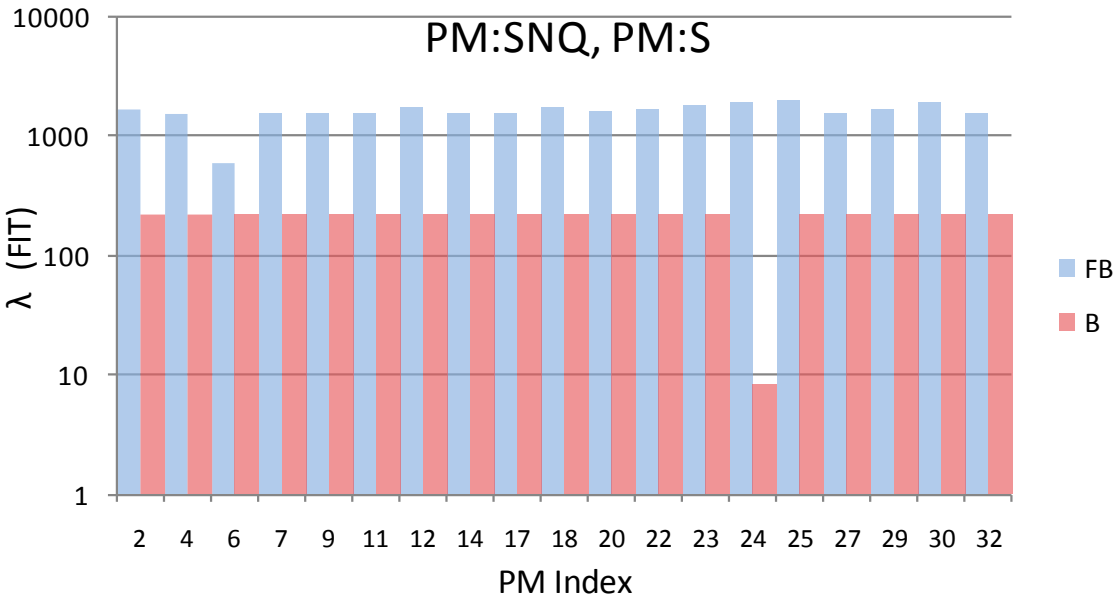

Figure 19: *PM:SNQ* and *PM:S* failures

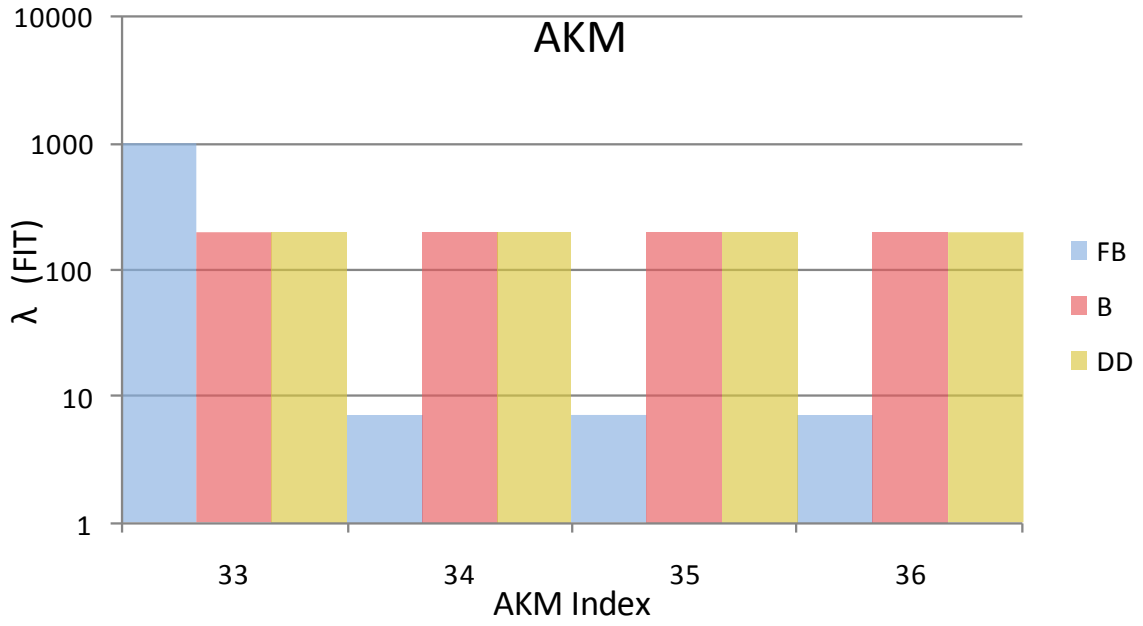

Figure 20: *AKM* failures

This work elucidates the impact of individual component reliability on the reliability of the entire module. The maximum values of λ_{FB}, λ_{FQ}, λ_B and λ_{DD} are 1987, 3332, 290 and 195 FITs. The corresponding MTTFs are 57, 34, 393 and 585 years. On an individual basis, these values are substantially greater than the 20 years' life of RHIC. But due to multiple modules and their operation dynamics, a system failure can occur within the 20 years range. This evaluation is done through the Monte Carlo simulation in section 2.4. The λ_{FB}, λ_{FQ} and λ_B for the *PMs* and the λ_{FB}, λ_B and λ_{DD} for *AKM* calculated here are used as the inputs for the simulation. An overall impact of these numbers on the BPS performance is evaluated.

The military handbook is fairly conservative in its approach as its failure rates are considerably higher than manufacturer supplied failure rates. The first priority is given to the manufacturer's data as it is up-to-date. For components not supplied with manufacturer's data, military handbook approach is beneficial from a safety analysis point of view.

2.5.2 Monte Carlo Analysis

Fig. 21 shows the pie chart for the probability of BPS system states expressed as a percentage of total dumps. As seen, a very small percentage of total failures occur in the system. The failures are further expanded in the second pie to show their relative sizes.

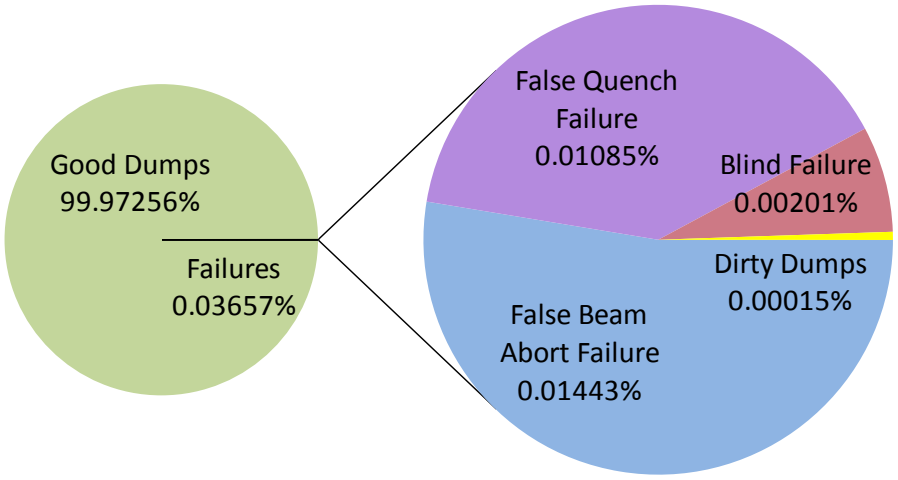

Figure 21: Probability of BPS system states

On an average, the beam operation per year is 165.6 days, calculated from historical data. In the model, each run lasts for an average of 3.5 hrs. This gives the number of runs per year as 1135. According to the pie chart, the MTTF of false beam abort failure, false quench failure, blind failure and dirty dump are 7.2, 9.5, 51.2 and 672 years respectively. The 20-year operational life of RHIC is quite lower than the blind failure MTTF, and so is the risk of a fatal failure. The false failure numbers here are acceptable, as they are failsafe and impose downtime to restart the machine. It is to be noted that the system failures calculated here are induced only due to the BPS failures. There might be other segments of RHIC that can cause a false or a blind failure.

The size of the pie sectors for failures depends on the magnitude of failure rates as well as the number of modules generating that failure. As seen here in Fig. 18, Fig. 19 and Fig. 20, the λ_{FQ} is generally much higher than the λ_{FB}, but due to large number of modules generating *FB* than *FQ*, the sector for false beam abort failure is bigger than false quench failure.

Chapter 3

Analytical Survival Model for Beam Permit System

In chapter 2, a Monte Carlo reliability model was developed to quantify the probabilities of system level failures that provides the numbers for a fixed operating time of RHIC (called the store length). Due to complex behavior of BPS, and consequent complex Monte Carlo simulation, it takes about 17 hours to run 1E9 iterations to generate reproducible results. This chapter explains an analytical multistate reliability model [76] of the BPS that gives insight into the development and propagation of system failures as a function of the store length. Similar to the Monte Carlo model, the individual modules have joint survival distributions defined by competing risks with exponential lifetimes. Modules differ in functionality and input response. The overall complex behavior of the system is analyzed by stochastic mathematics for different failure or survival states of the system. The model structure changes according to the type of failure. The analytical model yields the marginal survival distribution for each system state versus different store lengths. Analysis of structural importance and interdependencies of modules is also examined. The Monte Carlo model in section 2.4 is used for the verification of the analytical model.

3.1 Survival Distribution

The *PMs* and *AKMs* have been analysed for their failure modes in section 2.3. The top level failure of BPS depends upon the states of the *PMs* and *AKMs*. The calculation showed that the top level failures of the modules have exponential survival distribution, which is characterized by a constant hazard function λ. Modules can have *FB*, *FQ*, *B* and *DD* failure states, with failure rates as λ_{FB}, λ_{FQ}, λ_{B} and λ_{DD} resp. The *PMs* have {*FB*, *FQ*, *B*} and {*FB*, *B*} failure modes (green *PM* and grey *PM* resp. in Fig. 22). The *AKMs* have {*FB*, *FQ*, D}. The inputs *PI* and *QI* are modelled as Poisson variable with exponential trigger rate as λ_{PI} and λ_{QI}. The initial state is a Good (*G*) state, where the module performs its intended function properly.

A competing risks model with crude lifetimes [41] [55] is implemented here, where multiple risks compete with each other to cause a final failure. Mathematically if a module is subjected to *j = {1, 2...k}* risks, where $j = \{FB, FQ, B\}$ for *PMs*, and $j = \{FB, B, DD\}$ for *AKMs*. The crude probability distribution function of risk *j* is given by

$$F_j(t) = \frac{\lambda_j}{\sum_{i=1}^{k} \lambda_i} \left(1 - e^{-\left(\sum_{i=1}^{k} \lambda_i\right)t}\right); j = \{1, 2.., k\}$$

The marginal hazard rate for j^{th} risk is λ_j and *t* is the time of observation or the store length. The survival function for the module having competing risks is given by

$$S_T(t) = e^{-(\sum_{i=1}^{k} \lambda_i)t}$$

At any given instant for a module, following expression is always true

$$S_T(t) + \sum_{j=1}^{k} F_j(t) = 1$$

3.2 Analytical Model

The BPS has a ring configuration. A trigger arrival at a module initiates a carrier failure, which returns back to it after traversing all the modules in the system. The functionality of BPS that affects the reliability is to abort the beams and dump the magnet power upon the trigger arrival. The ring configuration is cut out to a linear structure, with inputs and outputs. The start of this structure is the *PM:M* [58] and the end is the *AKMs* that abort the beam. The problem of developing mathematical equations for system states is approached by looking at the states of each module in this system in Fig. 22. These states are of two kinds: trigger state that initiates a carrier failure (*FB*, *FQ*) and passive state where a module waits in that state for a trigger (*B*, *DD*, *G*). *PI* and *QI* are also the triggers to the system that initiate a carrier failure. For this reason, the failure density function *p(t)* (instantaneous probability) is always used for a triggering state and failure distribution function *P(t)* (probability that an event has occurred till now) for a passive state to derive the expressions for the system level failures. For m^{th} module, and j^{th} triggering state where *j= {FB, FQ, PI, QI}*

$$p_j^m(t) = \lambda_j e^{-(\sum_{i=1}^{k} \lambda_i)t} \; ; \; P_j^m(t) = \int_0^t p_j^m(t)$$

For j[th] passive failure state where *j*= *{B, DD}*

$$P_j^m(t) = \frac{\lambda_j}{\sum_{i=1}^{k} \lambda_i}(1 - e^{-(\sum_{i=1}^{k} \lambda_i)t});$$

For passive good state

$$P_G^m(t) = e^{-(\sum_{i=1}^{k} \lambda_i)t}$$

For a module *m*, at any given instant

$$P_G(t) + \sum_j \left(P_j^m(t)\right) = 1$$

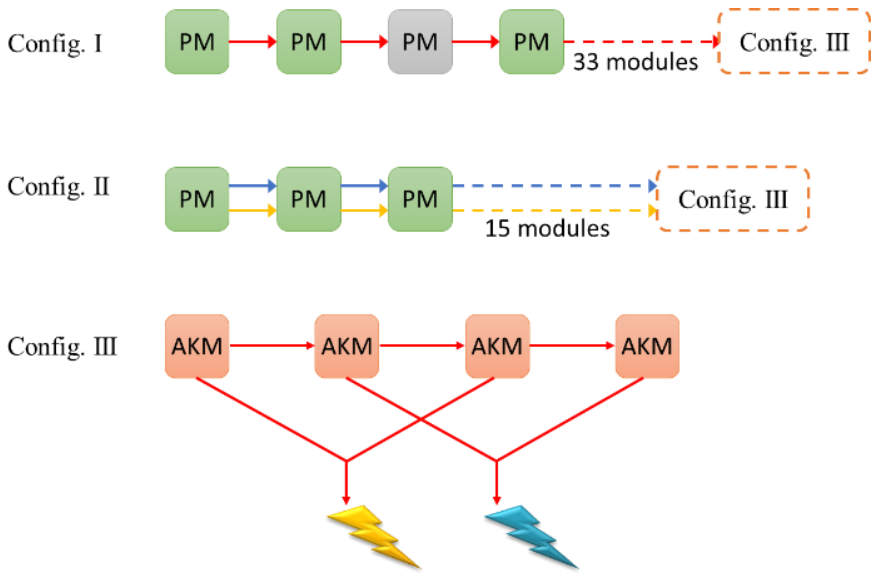

Figure 22: BPS connection diagram

Using above equations for modules' states, the analytical equations are further developed for the system states. The BPS modules are connected by multiple links and some of the modules do not have the blue or the yellow link connected to them. The structure of BPS is simplified (shown in Fig. 6) for different type of system states. Also because *AKM* exhibit redundancy, they are treated as separate entity that receive the signals from rest of the BPS. Consider the following configurations named I, II and III shown in Fig. 22. Config. I shows the path of permit link triggers i.e. *FB* and *PI*. Config. II shows the path of quench link triggers i.e. *FQ* and *QI*. Config. III shows the redundant configuration of the *AKMs* that signals the beam abort system to dump the beams.

To develop the equations for system states, the probability of each module is considered and the path of carrier failure to beam abort system is traversed one by one. The strategy to develop the equations is listed below, related to the system states that can result from the combinations of module states.

1. *SND*: *system no dump* - No trigger generated in I, II and III
2. *SGD*: *system good dump* - Trigger *PI* arrives in I, or *QI* arrives in II. No other triggers are generated anywhere else. Signal goes to the output of III, all modules in the forward path are in *G* state.
3. *SFD*: *system false beam abort dump* - Trigger *FB* arrives in I or III. No other triggers are generated anywhere else. Signal goes to the output of III, all modules in the forward path are in *G* state.
4. *SMD*: *system false magnet quench dump* - Trigger *FQ* arrives in II. No other triggers are generated anywhere else. Signal goes to the output of III, all modules in the forward path are in *G* state.
5. *SBD*: *system blind dump* - Trigger *FB*/*PI* arrives in I, or *FQ*/*QI* arrives in II, or trigger F arrives in II. Signal does not go to the outputs of III, at least one module in the forward path is in *B* state.
6. *SDGD*: *system dirty good dump* - Trigger *PI* arrives in I, or *QI* arrives in II. No other triggers are generated anywhere else. Signal goes the output of III, with at least one output passing through the *DD* state of redundant *AKMs*.
7. *SDFD*: *system dirty false beam abort dump* - Trigger *FB* arrives in I or III. No other triggers are generated anywhere else. Signal goes the output of III, with at least one output passing through the *DD* state of redundant *AKMs*.
8. *SDMD*: *system dirty false magnet quench dump* - Trigger *FQ* arrives in II. No other triggers are generated anywhere else. Signal goes the output of III, with at least one output passing through the *DD* state of redundant *AKMs*.

3.3 Results

The expressions are solved in Mathematica [77] and the time dependent probabilities functions for each system state are calculated. These probabilities are verified with the help of

Monte Carlo simulation reported in [41]. The failure rates of the modules are obtained from [40]. Some of the module failure rates are very small, especially *B* and *DD*, which reflect at the system level failures. Also due to the *AKM* redundancy, the *SDGD*, *SDFD* and *SDMD* failure probabilities are much smaller. The Monte Carlo simulation will need a large number of iterations to verify these results. Thus hypothetical failure rates are assigned to all the modules, with specific high failure rates for *DD* mode to overcome the redundancy effect, and get substantial number of *SDGD*, *SDFD* and *SDMD* states for the verification. Also assumed is a hypothetical store length of t = 0.232 hours. The Monte Carlo simulation is run for 2.4E9 iterations and takes about 40 hrs. to generate results. The probability is expressed as the ratio of system state generated and total no of system runs. Table 4 compares these hypothetical results from the Monte Carlo simulation and the analytical model (7-digit precision)

Table 4: Verification of the analytical model by Monte Carlo results

Abbr.	Analytical	Monte Carlo
$P_{SND}(t)$	0.0149852	0.0149856
$P_{SGD}(t)$	0.0621532	0.0621708
$P_{SFD}(t)$	0.3105783	0.3105881
$P_{SMD}(t)$	0.2494602	0.2494724
$P_{SBD}(t)$	0.2754812	0.2754846
$P_{SDGD}(t)$	0.0087564	0.0087507
$P_{SDFD}(t)$	0.0406134	0.0406134
$P_{SDMD}(t)$	0.0379719	0.0379183
Total (from model)	1.0000000	1.0000000

The individual probabilities of each scenario from the analytical model is very close to the probabilities obtained from the Monte Carlo. The exact sum of all the probabilities from the models is 1 as shown in the Table 4. This verifies that the relative probability expressions for a model considers all possible states in which the BPS can go.

This establishes that the analytical model and the Monte Carlo model both are verified. Next the actual failure rates are substituted in the analytical model and the actual failure probabilities of all the system states is obtained, with the store length equal to 6 hours. as RHIC average store length.

$P_{ND}(t) = 0.143573$

$P_{GD}(t) = 0.856193$

$P_{FD}(t) = \ 0.000123713$

$P_{MD}(t) = 0.000101377$

$P_{BD}(t) = 7.74551\ E - 6$

$P_{DGD}(t) = 1.39145\ E - 6$

$P_{DFD}(t) = 1.99945\ E - 10$

$P_{DMD}(t) = 1.64755\ E - 10$

Fig. 23, Fig. 24 and Fig. 25 show the graphs for the probability densities of three important system level failures (*SFD*, *SMD* and *SBD*) plotted as a function of store length in hours. The probability values above are cumulative values and can be calculated as the area under the curve up to a certain store length.

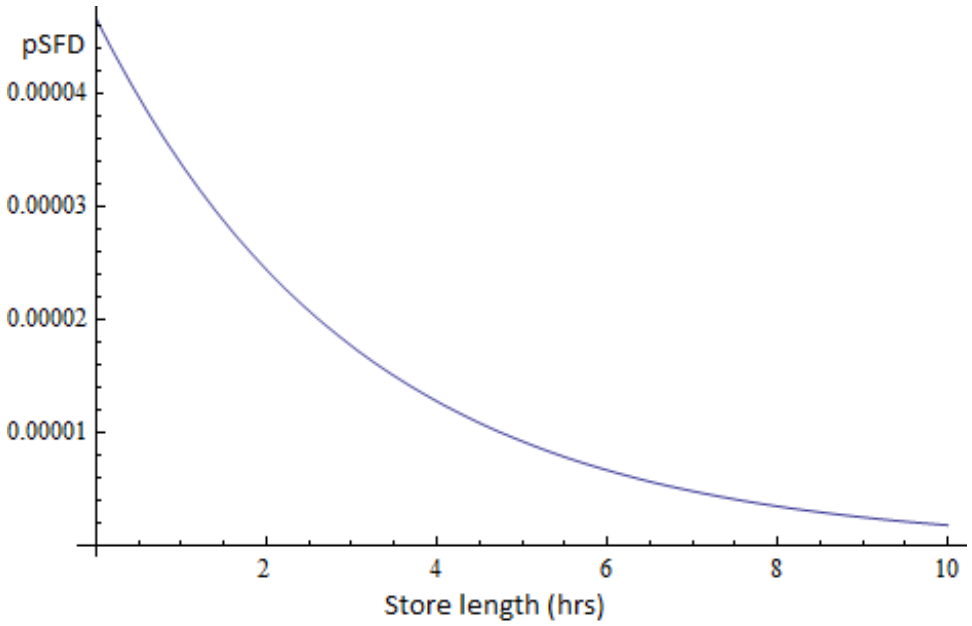

Figure 23: Probability density for *SFD* system failure

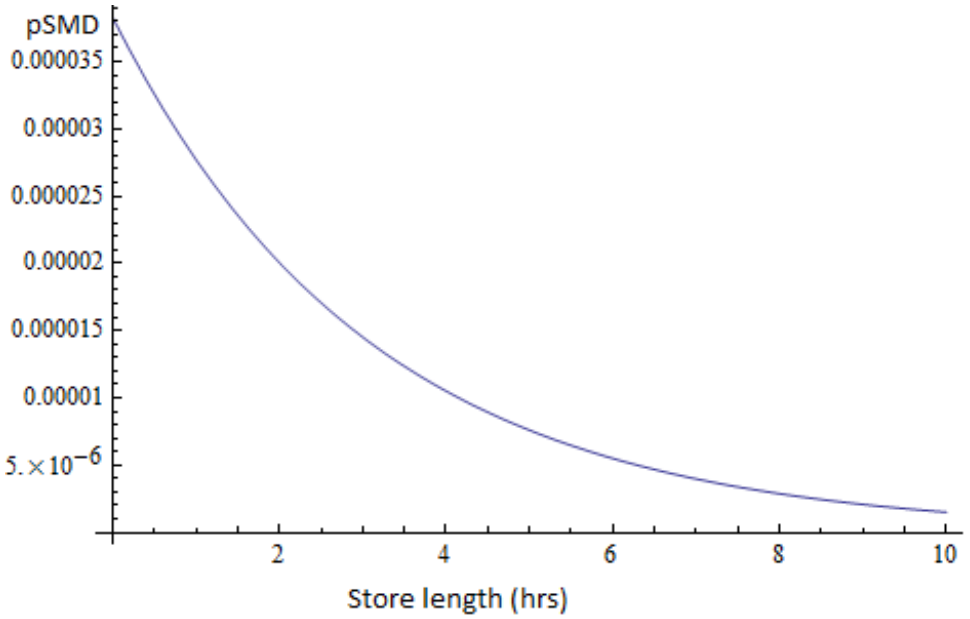

Figure 24: Probability density for *SMD* system failure

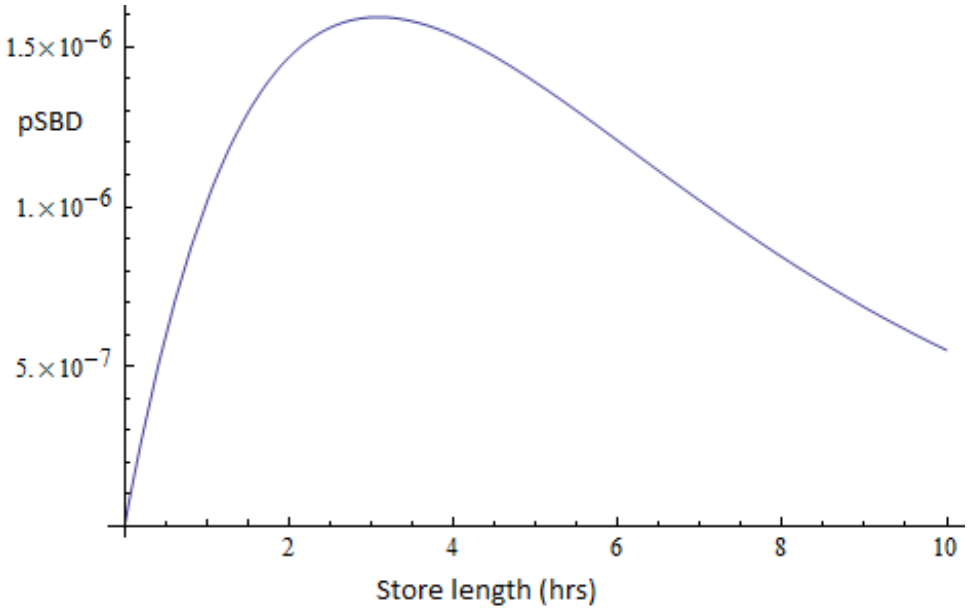

Figure 25: Probability density for *SBD* system failure

3.4 Importance Analysis

There are certain advantages of deducing the mathematical expressions for the probabilities of system level states. It facilitates quicker and easier analysis of the variation in system failure probabilities with changing component failure distributions or *PI*/*QI* trigger rates. This is utilized to analyze the importance of individual modules. Three major system failure states are analyzed here, *SFD*, *SMD* and *SBD*. The procedure is to increase the failure rates of *FB*, *FQ* and *B* modes for each module one by one, and observing the change in the system failure probabilities, which is an indicator of the importance of the module [78]. The importance of the modules is evaluated in two ways.

3.4.1 Structural Importance

First the structural importance of individual models is analyzed which is independent of their failure rates. For this, equal failure rates are assigned for a particular failure mode (*FB*, *FQ* and *B*) for every module. The order of magnitude is kept same as the actual failure rate. The number of *PI* and *QI* inputs are also fixed to the allowable maximum for the modules. The rate of *PI* and *QI* inputs is kept equal. The failure rate of each failure mode for a particular module is increased, and the effect on the system level failure is observed. The most significant influence on a system level failure mode is due to the corresponding module level failure mode e.g. the highest influence of *FQ* mode will be on the *SMD* mode. Thus the increase in module failure mode rate is observed on the corresponding system level failure mode rate. Table 5 summarizes the results for this analysis. The failure mode rate of modules is increased to 1000 times of the original and the % increase in the corresponding system level failure mode is recorded. This % increase directly indicates the structural importance of a module. The store length in the simulation is also increased to 20 hrs.

Table 5: Structural Importance of Modules

Module	Type	% increase in *SFD* from *FB*	% increase in *SMD* from *FQ*	% increase in *SBD* from *B*
0	*PM:M*	2746.62	7064.35	9.92
1	*PM:SQ*	2746.62	7064.35	20.03
2	*PM:SNQ*	2746.62		9.25

3	*PM:SQ*	2746.62	7064.35	33.26
4	*PM:SNQ*	2746.62		15.48
5	*PM:SQ*	2746.63	7064.35	46.49
6	*PM:SNQ*	2746.63		21.71
7	*PM:SNQ*	2746.63		24.83
8	*PM:SQ*	2746.63	7064.38	62.84
9	*PM:SNQ*	2746.63		31.06
10	*PM:SQ*	2746.65	7064.38	76.07
11	*PM:SNQ*	2746.65		37.29
12	*PM:SNQ*	2746.65		40.41
13	*PM:SQ*	2746.65	7064.38	92.42
14	*PM:SNQ*	2746.65		46.64
15	*PM:SQ*	2746.66	7064.38	105.65
16	*PM:SQ*	2746.66	7064.38	115.76
17	*PM:SNQ*	2746.66		55.99
18	*PM:SNQ*	2746.66		59.11
19	*PM:SQ*	2746.66	7064.42	132.11
20	*PM:SNQ*	2746.68		65.34
21	*PM:SQ*	2746.68	7064.42	145.34
22	*PM:SNQ*	2746.68		71.57
23	*PM:SNQ*	2746.68		74.69
24	*PM:S*	2746.68		74.78
25	*PM:SNQ*	2746.69		77.90
26	*PM:SQ*	2746.69	7064.42	164.89
27	*PM:SNQ*	2746.69		84.13
28	*PM:SQ*	2746.69	7064.42	178.12
29	*PM:SNQ*	2746.69		90.36
30	*PM:SNQ*	2746.69		93.48
31	*PM:SQ*	2746.71	7064.42	194.47
32	*PM:SNQ*	2746.71		197.68
33	*AKM*	2746.71		0.0005
34	*AKM*	2746.71		0.0005
35	*AKM*	2746.71		0.0970
36	*AKM*	-0.99		0.0005

The structural importance is dependent on the location of the module in the BPS. The start of the BPS model is the *PM:M* module and at the end are *AKM* modules (Fig. 22). For the *SFD* and *SMD* modes, it is seen that the importance slightly increases as the position moves towards the end of the model. Closer a module is towards the end, lesser are the chances for a triggering state like

FB or *FQ* to be blocked by a blind module. In this case the contribution will be made towards *SBD* failure by a *FB* or *FQ*.

The *SMD* mode is not influenced by the *PM:SNQ* and *PM:S* modules, as they do not have the blue and yellow link connected. Due to the same reason, when a triggering state like *FQ* or *QI* travels through the blue or yellow link, the *PM:SNQ* and *PM:S* modules are bypassed. This is observed in the *SBD* mode column. The gray cells in Table 5 are for the *PM:SNQ* and *PM:S* modules. For these modules it is seen that the increase in *SBD* rate is lesser than that in *PM:M* and *PM:SQ* modules. In general, there is an increase in failure rate as the module gets closer towards the end for both categories of *PM*. But this increase in importance with position is quite significant as compared to the *SFD* and *SMD* modes. This is because a blind module is able to block the triggering states coming from all the preceding modules. Thus the importance also depends on the number of preceding modules. For module *PM:S* (#24) there is only a slight increase in the importance for *SBD*, as it does not have any *PI* or *QI*, and hence no contribution to increase in blind failure due to these inputs. Module #32 is *PM:SNQ*, but the importance is comparable to *PM:SQ* because it does not get bypassed due to the BPS configuration.

The *AKM* modules also do not influence the *SMD* mode as they don't pass yellow and blue carrier link. For the *SFD* mode, the last *AKM* (#36) has the least increase in failure rate due to the redundancy and last position, so that it is rarely accessed due to a redundant module before. For the *SBD* mode, the importance is very less because of the redundancy.

3.4.2 Overall Importance

In this section, combined effect of failure rate magnitude and structural position is assessed for each module. Now the actual failure rates are assigned to all the failure modes. The number of *PI* and *QI* inputs and their arrival rates are also changed as per the real configuration of the BPS. Similar to the section 3.4.1, the failure rate of each failure mode for a particular module is increased, and the effect on the system level failure is observed. The increase in module failure mode rate is observed on the corresponding system level failure mode rate. Table 5 summarizes the results from this analysis. The failure mode rate of modules is increased to 100 times of the original and the % increase in the corresponding system level failure mode is recorded. This %

increase directly indicates the overall importance of a module. The store length in the simulation is set to the actual value of 6 hrs.

Table 6: Overall Importance of Modules

Module	Type	% increase *SFD* from *FB*	% increase in *SMD* from *FQ*	% increase in *SBD* from *B*	Importance order for modules		
					SFD	*SMD*	*SBD*
0	*PM:M*	4.660787	661.2013	49.54987	25	26	31
1	*PM:SQ*	78.16236	219.4443	91.42187	24	21	28
2	*PM:SNQ*	355.7662		58.01542	30	5	26
3	*PM:SQ*	282.3042	805.5447	114.4752	23	31	21
4	*PM:SNQ*	329.5159		75.42421	18	19	32
5	*PM:SQ*	214.1246	810.1926	179.4006	12	8	19
6	*PM:SNQ*	125.3935		133.4423	2	13	30
7	*PM:SNQ*	333.9625		139.2444	22	3	16
8	*PM:SQ*	283.7867	807.0953	233.1892	29	10	29
9	*PM:SNQ*	329.5167		162.4553	20	28	15
10	*PM:SQ*	287.1743	804.7723	298.1158	7	0	27
11	*PM:SNQ*	329.5175		203.0698	17	15	25
12	*PM:SNQ*	377.1487		208.8731	32	16	23
13	*PM:SQ*	282.3058	805.8051	336.5432	27	1	22
14	*PM:SNQ*	329.5175		232.084	11		13
15	*PM:SQ*	213.7027	650.616	401.4699	14		20
16	*PM:SQ*	78.16317	219.4452	416.8401	9		10
17	*PM:SNQ*	332.0589		295.9055	4		18
18	*PM:SNQ*	380.3254		295.9081	10		17
19	*PM:SQ*	283.5765	807.6142	462.9455	21		8
20	*PM:SNQ*	342.0093		319.1189	8		14
21	*PM:SQ*	286.7532	834.4654	527.8734	28		12
22	*PM:SNQ*	355.1349		353.9327	19		11
23	*PM:SNQ*	382.8668		359.736	31		5
24	*PM:S*	404.4579		13.14155	26		9
25	*PM:SNQ*	420.7569		365.5433	13		7
26	*PM:SQ*	282.3074	860.5413	558.6267	3		6
27	*PM:SNQ*	329.5199		377.1513	5		3
28	*PM:SQ*	283.5781	795.9971	623.5547	15		1
29	*PM:SNQ*	350.6907		411.965	33		4
30	*PM:SNQ*	398.1085		417.7696	6		2
31	*PM:SQ*	282.3082	808.3905	646.6184	16		0

32	*PM:SNQ*	329.5207		499.9218	1		24
33	*AKM*	210.7402		0.000258	0		33
34	*AKM*	1.483272		0.000258	34		34
35	*AKM*	1.483272		0.000258	35		35
36	*AKM*	0		0.000258	36		36

The failure rates of the failure modes of each module are shown in Fig. 18, Fig. 19 and Fig. 20. Apart from the influence of structural placement of modules as discussed in section 3.4.1, the overall module importance is highly dependent on the failure rate. Alongside structural placement also plays a key role in determining the overall importance. The modules which are in the path of propagation of multiple failures have higher importance. Nearer a module is to the abort system output, higher is its importance. This is because probability of it being bypassed in failure propagation is small. The *AKMs* have lower importance due to the redundancy incorporated. The components that are major contributors to the higher failure rate are discussed in section 7.2.3.

Chapter 4

Bayesian Reliability Model for Beam Permit System

Bayesian Analysis provides a statistical framework for updating prior knowledge as observational evidence is acquired. It can handle complex and realistic models with flexibility. In section 2.4, a multistate reliability model is developed to study the failure characteristics of the BPS that incorporates manufacturer supplied failure data and military handbook data. Over the course of its 15 years of operation, RHIC has brought forth operational failure data. This part of the dissertation work aims towards the integration of earlier reliability calculations with operational failure data using Bayesian analysis. This chapter discusses the Bayesian inference of the BPS reliability using a two-parameter Weibull survival model, with unknown scale and shape parameters. As the joint posterior distribution for Weibull with both parameters unknown is analytically intractable, the Markov Chain Monte Carlo methodology with Metropolis-Hastings algorithm is used [79] [80] to obtain the inference. Selection criteria for the Weibull distribution, prior density and hyperparameter are also discussed.

4.1 Bayesian Statistical Domain

Bayesian statistics [79] is branch of mathematics that deals with updating current knowledge about a system or process when new information is acquired. Statistical analysis follows two major approaches, namely the frequentist approach and the Bayesian approach. In the widely used frequentist approach, the probability distribution of an event is calculated by observing its occurrence over a large period of time, and the distribution parameters are assumed to be constant over time. In contrast, Bayesian approach keeps updating the probability distribution as new data arrives. The parameters of the distribution are treated as random variables that are modified according to the new information gathered. Bayesian technique becomes quite important when there are two sources of information about a system or process that indicate different results, and both sources hold significance to the inference.

The underlying framework for Bayesian analysis is Bayes theorem. Bayesian analysis involves the continuous form of the Bayes theorem [79], which is represented as

$$\pi(\theta|x) = \frac{L(\theta|x) \times \pi(\theta)}{g(x)}$$

The unknown parameter is θ, which defines the probability distribution of any process and is subject to change with the arrival of new information. Variable x is the new source of information in the form of data observations. The term $\pi(\theta)$ is called the prior distribution of θ, which can be elicited by using another parameter(s) called the *hyperparameter(s)*. $L(\theta|x)$ is the likelihood function for θ which is calculated by gathering new data. The term $\pi(\theta|x)$ is called the posterior distribution of θ, which is a combination of both prior and data likelihood function. $g(x)$ is the unconditional distribution of the variate *x* that acts as a normalizing factor in the equation. Because $g(x)$ is independent of θ:

$$\pi(\theta|x) \propto L(\theta|x) \times \pi(\theta) \quad (1)$$

This equation forms the foundation for Bayesian analysis discussed in this chapter. The selection of prior distribution and data distribution (likelihood function) is discussed in subsequent sections.

The Monte Carlo reliability model in section 2.4 simulates the progression of basic component failures to the system level catastrophic events, and helps characterize the failure rate and structural importance of each basic component of the BPS. This model takes a profound view in the reliability characteristics of the BPS. However, it uses military handbook [65] and manufacturer supplied failure data which provides basic reliability information as a point estimate for the exponential survival distribution, and can be conservative.

RHIC has been operational for last 15 years, and has gathered hardware failure data over this time period. This data represents the true failure characteristics of BPS from a system level perspective. However due to high inherent reliability of BPS, failure data on every component is not available, hence it is not possible to take a deeper look into the system failure behavior through this data.

Each of these reliability information sources provide important information about the BPS reliability, with their own limitations. Thus both of them need to be considered collectively. Bayesian analysis is a good candidate for combining these two information sources to get a combined inference about the system failure characteristics.

4.2 Preliminary analysis

Preliminary analysis is needed to find the suitability of Bayesian analysis to this problem and for choosing the distribution appropriate to the information sources that are available. Two sources of information are analyzed here, the results from a Monte Carlo model [41] and the historical failure data obtained from the RHIC control hardware maintenance records.

4.2.1 Source 1: Monte Carlo Simulation Results

The Monte Carlo model defines the propagation of component failures to the system level, depending upon the states of other components and the structure of the system. As the component failures were taken from the military handbook [65] and the manufacturer supplied failure data, they provided point estimate for the hazard rate λ, with exponential survival distribution. These exponential failures might evolve as a different distribution on the system level. The four system level failures modes in the Monte Carlo model are combined to a single failure for applying Bayesian analysis. Next the failure rate pattern of this single failure of BPS is analysed.

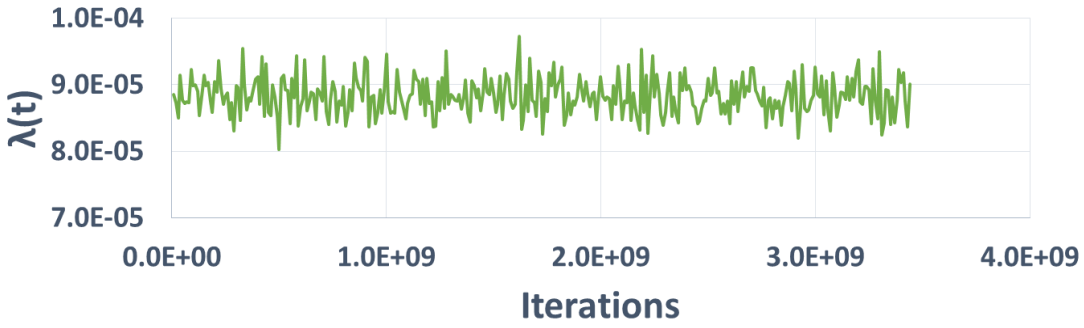

Figure 26: Detection for NHPP failures

First check is to find if the failure rate follows the Non Homogenous Poisson Process (NHPP) [81], for which specialized Bayesian analysis is needed. The interval failure rates are plotted to see

if they are time varying, and whether follow a typical distribution. The number of failures in an interval of 10^7 hours is calculated, and the failure rate is plotted for each interval in Fig. 26. The rate is noisy but has a constant mean over the time. Thus it is obvious that the Monte Carlo model failure is not an NHPP.

Next, a suitable failure distribution function for the Monte Carlo model has to be found. The simulation is run for 1.3E9 iterations and the total failures are recorded as point processes. The times between failures are fitted with Exponential, Weibull and Gamma distributions with the forms specified in [54] using MATLAB® [82]. The goodness of fit is estimated by Akaike Information Criterion (AIC) and Bayesian Information Criterion (BIC) [83].

Table 7: Monte Carlo model failure distribution

Distribution	Parameter	Point estimate	AIC	BIC
Exponential	Scale: λ	8.831e-5	3141125.52	3141136.15
	Shape: α	1		
Weibull	Scale: λ	8.829e-5	3141127.47	3141148.72
	Shape: α	1.00046		
Gamma	Scale: λ	8.84e-5	3141127.44	3141148.66
	Shape: α	1.00106		

As seen in Table 7, the AIC and BIC are smallest for the exponential distribution, which indicates that the exponential distribution is the best fit to the overall system failure. The failure rate is λ and the shape parameter is α. Following is the probability density function for the exponential distribution for the Monte Carlo model:

$$f(x) = \lambda e^{-\lambda x}$$

Here

$f(x)$ = probability density function

x = times between failures from Monte Carlo model (in hours)

λ = scale parameter = 8.831e-5

Although the military handbook [65] is quite old, its applicability to the BPS can justified as RHIC has been running since 1997, which was contemporary to the release of this version of military handbook.

4.2.2 Source 2: Historical failure data

Past 15 years of hardware failure data of BPS has been analyzed, and the system level failures that are similar to the ones analyzed by the Monte Carlo model are selected. Overall 16 data points for the time between failures are found owing to the high reliability of BPS. To analyze the distribution of this data, Exponential, Weibull, Gamma and Lognormal distributions are fitted using MATLAB® and goodness of fit is estimated using AIC and BIC, shown in table 8.

Table 8: Historical failure data distribution

Distribution	Parameter	Point estimate	AIC	BIC
Exponential	Scale: λ Shape: α	1.20E-04 1	322.9279	323.7005
Weibull	Scale: λ Shape: α	0.000171 0.627457	317.6438	319.189
Gamma	Scale: λ Shape: α	6.03E-05 0.503074	318.1511	319.6963
Lognormal	Mean: μ Variance: σ	7.7676 1.99141	319.0121	320.5573

Looking at the Table 8, it is seen that the AIC and BIC are now smallest for the Weibull distribution, asserting that the BPS has a Weibull survival distribution with decreasing failure rate. Following is the probability density function of Weibull distribution for the historical data:

$$f(x) = \alpha\lambda^{\alpha}x^{\alpha-1}e^{-(\lambda x)^{\alpha}} \quad (2)$$

Here

$f(x)$ = probability density function

x = times between failures from historical data (in hours)

λ = scale parameter = 0.000171

α = shape parameter = 0.627457

The historical data distribution represents the actual failure characteristics of the system, even if the Monte Carlo model suggests that the system follows exponential survival distribution.

4.3 Bayesian Reliability Model

The parameters of the posterior distribution reflect the tradeoff between the prior distribution and the data distribution (incorporated using likelihood function). This tradeoff level is determined by the relative strength of the prior and data distributions. The influence of either can be changed by altering the hyperparameters. It is often desirable to choose a prior of a form such that the posterior distribution calculated is mathematically tractable. One of the techniques is to employ a *conjugate prior* that yields a posterior of the same form as the data distribution [79], but with different parameters. The posterior parameters specify the adjustment between the prior and the data.

For the Bayesian model of BPS, the prior information is an exponential distribution and the data is a Weibull distribution with shape parameter less than 1. It is thus assumed that the prior information is also a Weibull distribution with shape parameter equal to 1. Also the scale parameters of both information sources are different. Thus a Bayesian model needs to be chosen for the Weibull distribution with both shape and scale parameters unknown. To implement this, first a conjugate prior distribution is chosen that is suitable to the Weibull distribution of the data. There is no best way to define a prior distribution for the Bayesian analysis [79]. The following sections outline the development of the Bayesian model step by step.

4.3.1 Data Distribution

Vidakovic [80] suggests a model for the Bayesian inference of Weibull distribution that is unknown in both shape and scale parameters. This model is followed throughout in this analysis. Following is the Weibull distribution used in [80]

$$f(x|\alpha,\eta) = \alpha\eta x^{\alpha-1}e^{-\eta x^{\alpha}}$$

Here

$f(x|\alpha,\eta)$ = probability density function

x = times between failures (in years)

$\eta^{-1/\alpha}$ = scale parameter

η = transformed scale parameter

α = shape parameter

This form does not have explicit posteriors for α and η. A Bayesian inference is drawn for these two parameters. The likelihood function for the Weibull distribution specified above is

$$L(\alpha, \eta|x) = \prod_{i}^{k} \alpha\eta x_i^{\alpha-1} e^{-\eta x_i^{\alpha}}$$

Here

$L(\alpha, \eta|x)$ = likelihood density function of data points

x = times between failures (in years)

η = transformed scale parameter

α = shape parameter

k = number of data points

The parameters α and η are treated as variables in the likelihood function for Bayesian analysis, and have *[0, ∞)* support. The most probable values of α and η are obtained by parameters of Weibull distribution fitted on the historical data. They are calculated by converting the λ and α parameters from the Weibull distribution of historical data in Eq. 2.

$$\alpha = 0.6275, \eta = 1.2904 \quad (3)$$

Fig. 27 plots the three dimensional likelihood function density with α and η as variables. Note that α and η values from Eq. 3 correspond to the maximum likelihood point, plotted as a red dot.

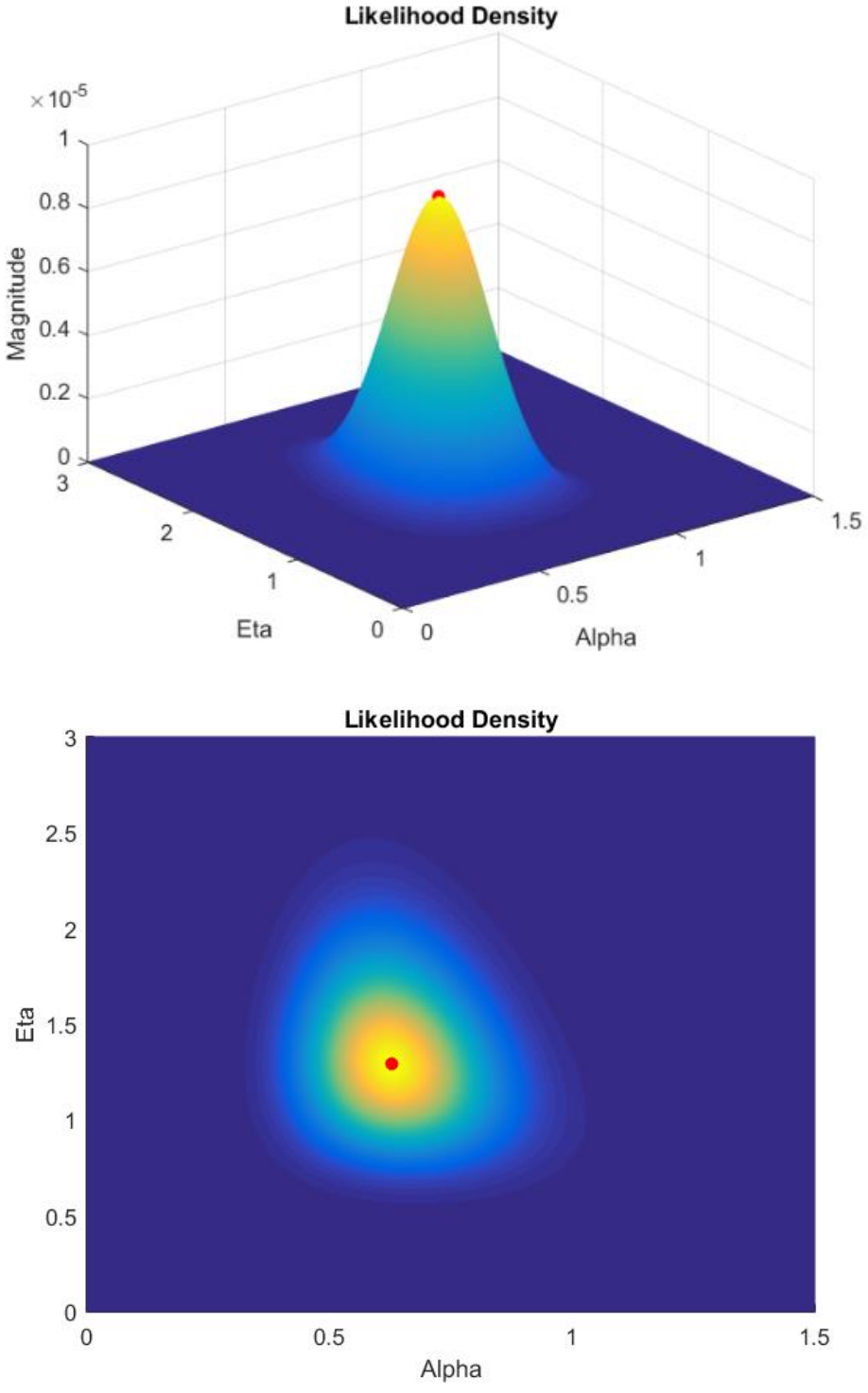

Figure 27: Likelihood function plot with α, η, with 3D and top view

4.3.2 Conjugate Prior Distribution

A conjugate prior distribution is proposed for the Weibull distribution in [80]. This is a joint distribution for α and η, with a hyperparameter β.

$$p(\alpha, \eta) \propto e^{-\alpha} \eta^{\beta-1} e^{-\eta\beta} \tag{4}$$

Here

$p(\alpha, \eta)$ = prior probability density function

η = transformed scale parameter

α = shape parameter

β = hyperparameter

Note that only the kernel (omitting the proportionality constant) of the prior distribution is used here. This is explained later in the posterior inference. The prior parameter λ (and α = 1) representing the exponential distribution (Weibull with shape as 1) in Table 7 are converted to α and η.

$$\alpha = 1, \eta = 0.7741 \tag{5}$$

These are the point estimates of α and η. The joint distribution of α and η needs to be defined so that it best represents the beliefs about the prior information. The hyperparameter β is chosen to be equal to 3. The reason for choosing β is explained below. The 3D prior density from Eq. 4 is plotted with α and η as variables in Fig. 28. Note that the magnitude on the plot is unnormalized. The point estimates from Eq. 5 are plotted as a red dot on the same figure. Note that in this case, this point does not correspond to the peak of magnitude in the plot.

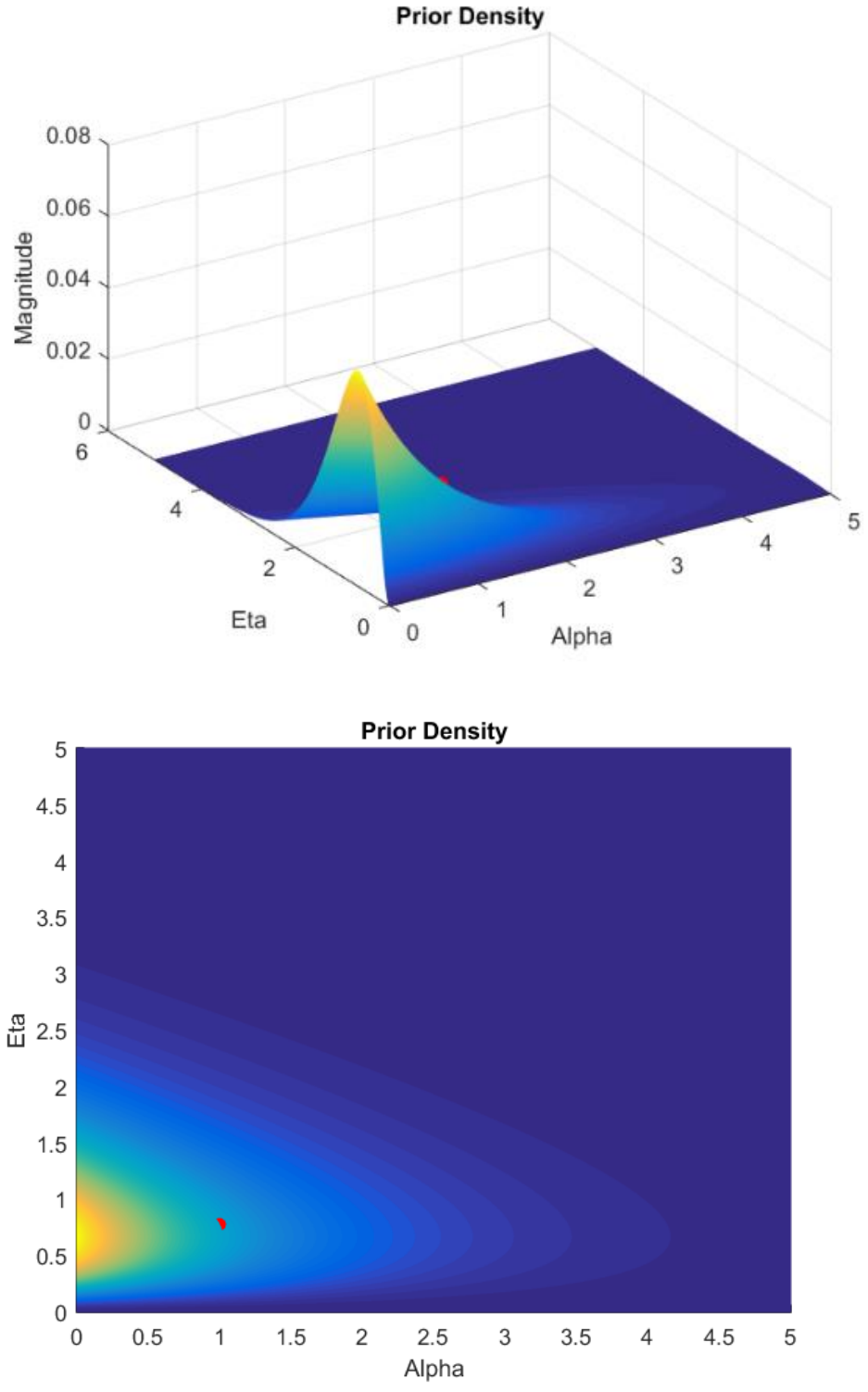

Figure 28 : Prior density plot with α, η with 3D and top view

For getting clarity into this, refer to the Fig. 29, the 2D prior density for η with constant $\alpha = 1$ at the top and the 2D prior density for α with constant $\eta = 0.7741$ at the bottom.

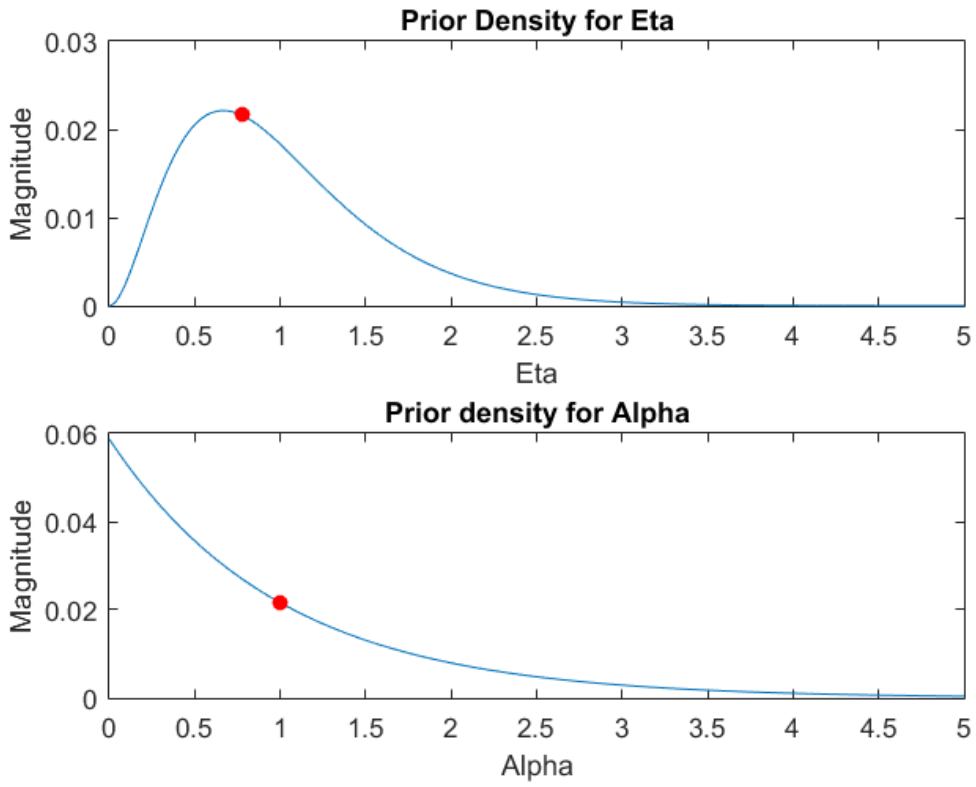

Figure 29: 2D Prior densities for α, η

In Fig. 29 top figure, the point estimate lies almost on the peak of the density distribution which signifies the high confidence in the value of scale parameter of the prior obtained from the Monte Carlo model. But in Fig. 29 bottom figure, the point estimate does not lie on the peak, rather much lower than the highest magnitude point. This is chosen because the shape parameter is a system characteristic, which is less likely to change. For the data distribution it is seen that α is much less than one in Eq. 3. Thus it is reasonable to express more confidence in the lower values of α than the one obtained from the Monte Carlo model. Thus the prior density is higher for smaller values of α.

4.3.3 Posterior inference

The posterior distribution is a fusion of the prior and data distributions that contains all the information of the parameters of the system, in this case α and η. From Eq. 1, the proportionality equation (or kernel) for posterior is obtained as:

$$p(\alpha,\eta|x) \propto \alpha^{k}\eta^{k+\beta-1}\left(\prod_i^k x_i\right)^{\alpha-1} e^{(-\eta\sum x_i^{\alpha}-\alpha-\eta\beta)}$$

Here

$p(\alpha,\eta|x)$ = posterior probability density function

x = times between failures (in years)

η = transformed scale parameter

α = shape parameter

k = number of data points

As this is a mathematically intractable joint distribution of α and η, it is not possible to obtain independent and identically distributed samples directly from this unnormalized kernel. Metropolis Hastings (MH) algorithm is used which is a type of iterative Markov Chain Monte Carlo (MCMC) technique [79]. The parameters α and η are calculated as sample averages of realizations of Markov chains, so one has to ensure that the Markov chain has converged before drawing the samples. To generate the random samples of α and η, a "proposal density" is used, given the samples from previous iteration. Following proposal density is suggested in [80].

$$q(\alpha',\eta'|\alpha,\eta) = \frac{1}{\alpha\eta}\, e^{\left(\frac{\alpha'}{\alpha}-\frac{\eta'}{\eta}\right)}$$

Here α',η' are the new samples and α,η are the previous samples. In MH algorithm, samples are drawn from the proposal density. Individual samples are then accepted or rejected as per the acceptance probability given by:

$$a\big((\alpha',\eta'),(\alpha,\eta)\big) = min\left\{1, \frac{p(\alpha',\eta')/q(\alpha',\eta'|\alpha,\eta)}{p(\alpha,\eta)/q(\alpha,\eta|\alpha',\eta')}\right\}$$

There is a typical advantage of MH algorithm that it need not consider the full conditionals because the normalizing factors cancel in the ratio of acceptance probability equation. For more details on the MH algorithm refer to [79] [80].

4.4 Results

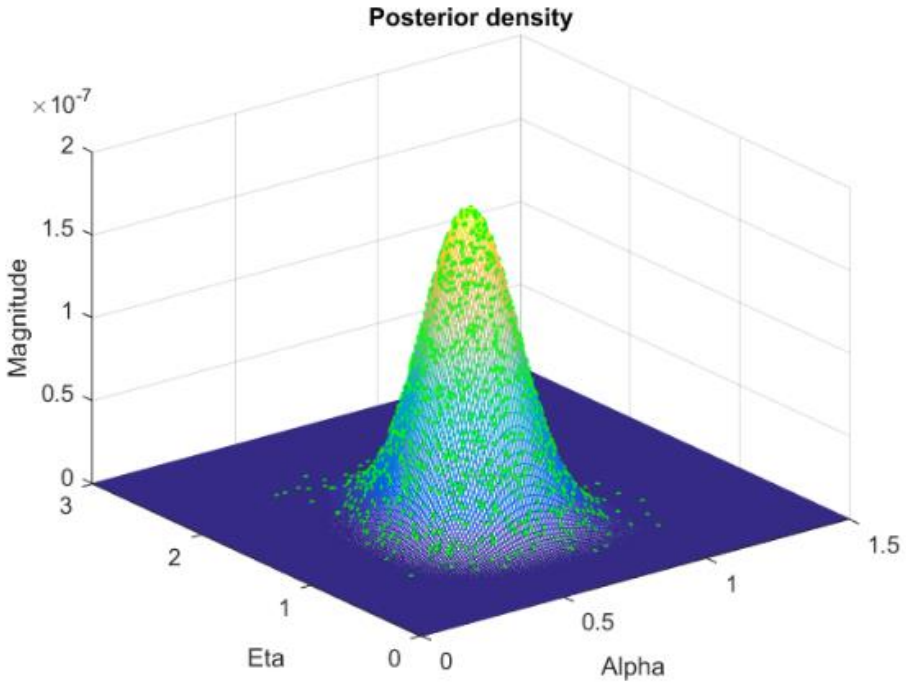

11

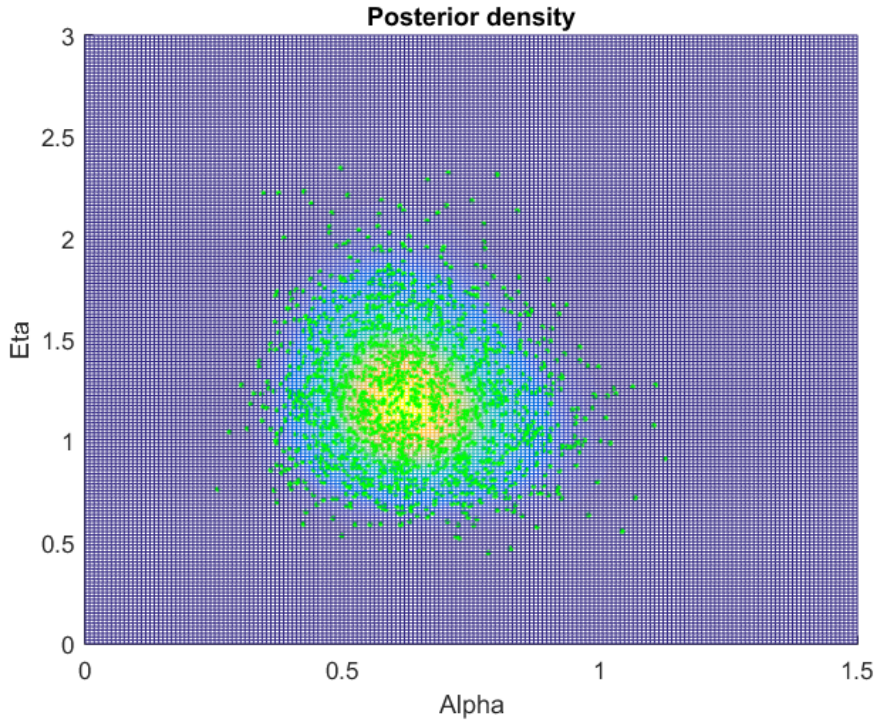

Figure 30: Posterior density for α, η, 3D and top view

After running 25K iterations of the MH algorithm on the posterior density, initial 5000 samples are rejected to allow the Markov chain convergence Fig. 30 shows the samples (green dots) obtained from the MH algorithm, and a connecting surface is plotted. To obtain the values of α and η from the posterior, samples obtained from the MH algorithm are observed. Fig. 31 and Fig. 32 show the samples of α and η and their histograms.

As seen, the subsequent sample generation looks stationary [81], thus it can be said that the Markov chains have converged. Also the histograms in Fig. 32 are unimodal, thus the means of the samples represent the meaningful inference for α and η parameters.

Following values of α and η are obtained for the posterior from the sample means

$$\alpha = 0.6327, \eta = 1.2225 \tag{6}$$

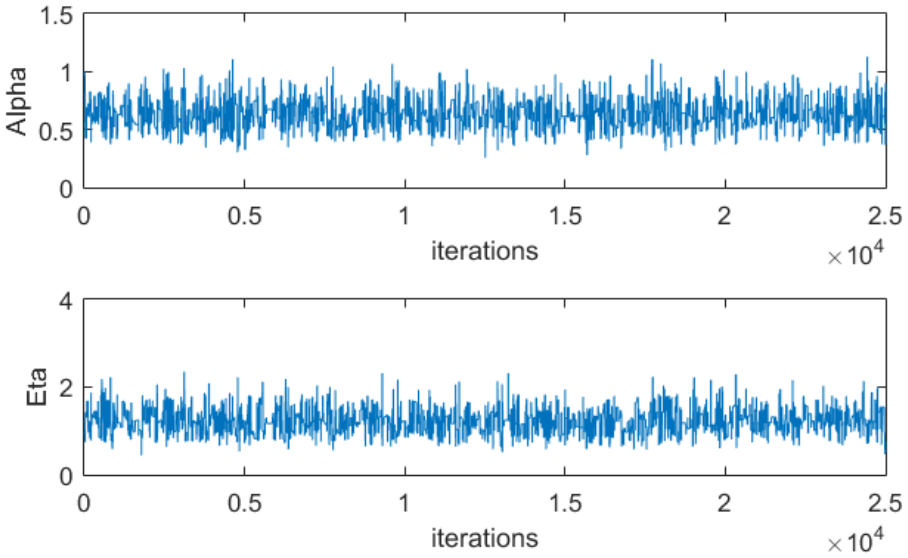

Figure 31: α, η samples from MH algorithm

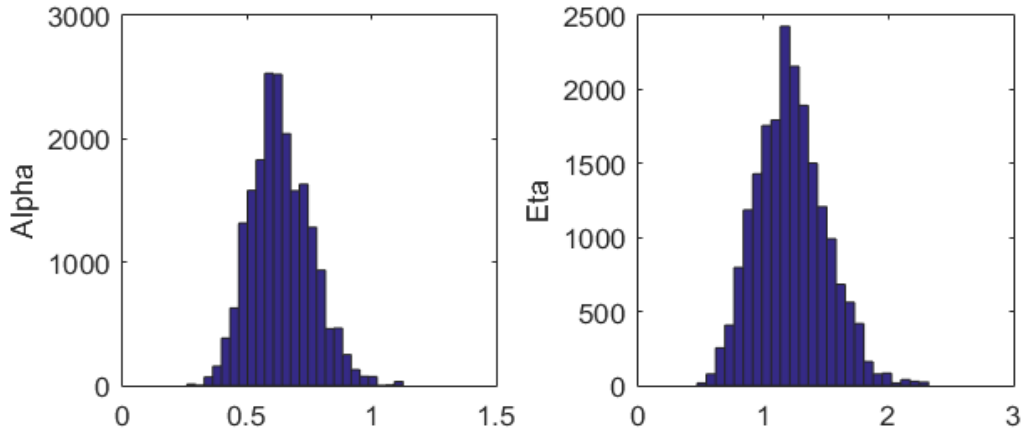

Figure 32: α, η samples' histogram from MH algorithm

4.5 Discussion

Fig. 33 shows the cumulative failure distribution function of the prior, data and posterior distributions for Weibull using the parameters in Eq. 3, Eq. 5 and Eq. 6. According to the discussion on choosing the hyperparameter β in section 4.3.2, low confidence is expressed in the value of alpha being 1. This can be seen in Fig. 33 where the posterior shape is more like the data distribution, i.e. the relative strength of the data distribution is much more than the prior distribution.

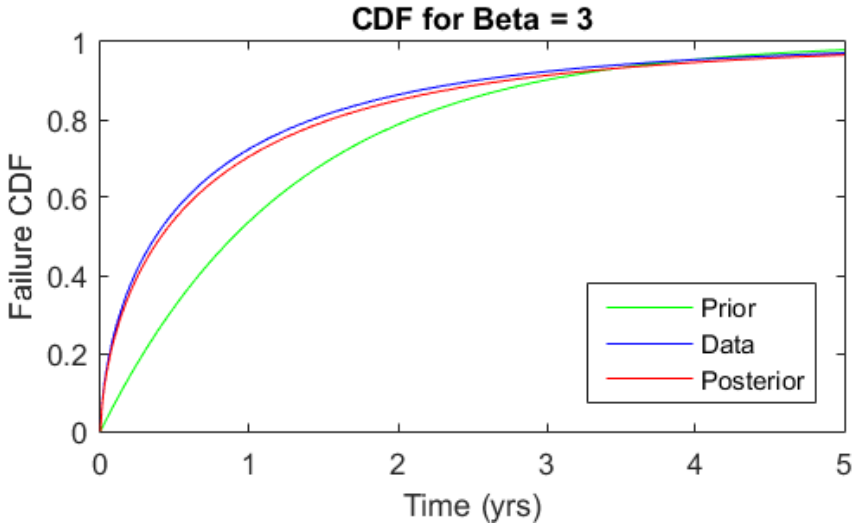

Figure 33: Cumulative failure distributions for β=3

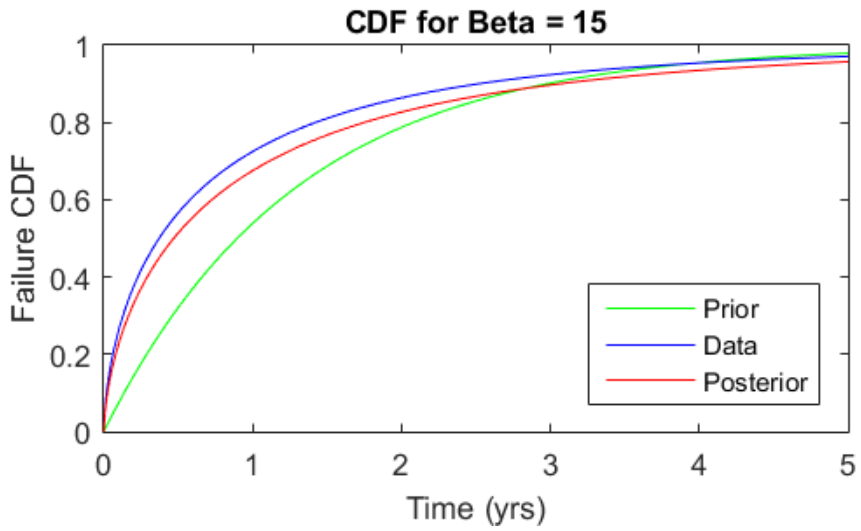

Figure 34: Cumulative failure distributions for β=15

To illustrate the concept of relative strength of the prior and the data, the confidence in prior is increased by increasing the hyperparameter value. Fig. 34 shows the prior, data and posterior distribution for β equal to 15. The prior strength is now increased that is apparent on the posterior, which is now closer to the prior as compared to Fig. 33. The posterior parameters for β = 15 are a higher value of $\alpha = 0.6404$ and lower value of $\eta = 1.1249$. For this analysis, the value of β = 3 is upheld, because it represents high confidence in the actual machine failure data, with a mild influence of the Monte Carlo model results.

Chapter 5

Nonlinear System Identification for Superconducting Magnet Inductance

Superconducting magnets in RHIC generate magnetic fields up to 3.458 T that are used to confine the particle beams in defined trajectories. Due to several reasons as specified in [84], the superconducting magnets can quench causing development of resistive zones. The operating current in RHIC dipole magnets is above 5000A, which if dissipates in the resistive zone can result into serious damage. To detect an emerging quench, an electrical tap is provided across a certain number of series connected superconducting magnets to monitor the voltage across them. A magnet model is stored in a DSP that calculates the expected nominal voltage across the tap as $V = L\, di/dt$ and compares it to the measured tap voltage. Here L is the inductance of magnet circuit and I is the magnet current. A deviation of more than 25mV is sensed as a developing quench. The quench protection assembly then activates, taking the current out of the magnet circuit and initiates beam abort. A superconducting magnet behaves as a pure inductance. The magnet model outlines the variation in inductance vs the magnet current, considering saturation and hysteresis. For high availability and reliability of RHIC, L needs to be determined with precision to avoid false quench triggers.

The Quench Detection System (QDS) of RHIC detects the superconducting magnet quenches by voltage sensing. The real-time voltage across the superconducting magnet is compared with a predicted voltage from the behavioral model, a deviation from which triggers the quench event and energy extraction. Due to the limitations of the magnet model, many false quench events are generated that affect the RHIC availability. This chapter is targeted towards remodeling the magnets through nonlinear system identification [43] for the improvement in QDS reliability. The nonlinear electrical behavior of the superconducting magnets is investigated by statistical data analysis of magnet current and voltage signals. Many data cleaning techniques are employed to

reduce the noise in the observed data. Piecewise regression has been used to examine the saturation effects in magnet inductance.

5.1 Introduction

The RHIC superconducting magnets store an energy of 70MJ in the form of magnet currents during a full energy run. The superconducting magnets are susceptible to quenches that lead to development of tiny resistive zones. An operating current near 5000A (for a dipole magnet) can dissipate this enormous energy at this tiny resistive point causing catastrophic damage.

To safeguard against such failure, QDS as explained in section 1.5.2 is employed. It monitors the superconducting magnets to detect the developing quenches and sends the magnet power dump signal and beam abort signal to the BPS. Voltage sensing is employed for recognizing the developing quenches. The QDS consists of DSPs which store the electrical behavioral model of the superconducting magnets. The actual magnet output is compared to the model output, and a deviation is sensed as a developing quench, which generates a quench trigger.

The superconducting magnets exhibit a highly nonlinear behavior due to saturation and hysteresis of steel yoke [4]. Due to mathematically intractable nature of this behavior, the magnet model parameters are manually calibrated, which inhibit the accurate tuning of the model. Also tuning consumes valuable time when RHIC is running at 4K temperature. Inaccuracies introduce deviation in the model output, which leads to false failures, and resulting in unnecessary machine downtime. Thus to improve QDS reliability, it is necessary that the model truly imitates the superconducting magnet behavior. The aim of this work is to facilitate automatic generation of accurate magnet models through nonlinear system identification that will improve the reliability and availability of QDS. Fig. 11 shows the electrical circuit model for QDS.

5.1.1 Original magnet model

The superconducting magnet circuit's electrical behavior is modeled as a pure inductor with a series resistor. The pure inductor represents the superconducting magnet and the resistance represents the current leads to the magnet. The model is

$$V_c = L\frac{dI}{dt} + RI$$

Here I is the current through the magnet, L is the nonlinear magnet inductance, R is the lead resistance and V_c is the calculated voltage from the model. This voltage is compared to the observed voltage V_o across the magnet in real time. When a quench develops, additional resistance will appear causing V_o to deviate from V_c. The minimum of a 25mV difference between these two triggers a quench event. The parameter L is highly nonlinear in nature. It exhibits saturation i.e. its value decreases with increasing current. Also the *L vs. I* curve changes with the change in applied current ramp waveform. The DSP model stores lookup table for *L vs. I* values, which have to be updated manually every time a new current waveform is introduced. A manually calibrated *L vs. I* lookup table is plotted in Fig. 35. This gives a rough idea of the nonlinear behavior of L.

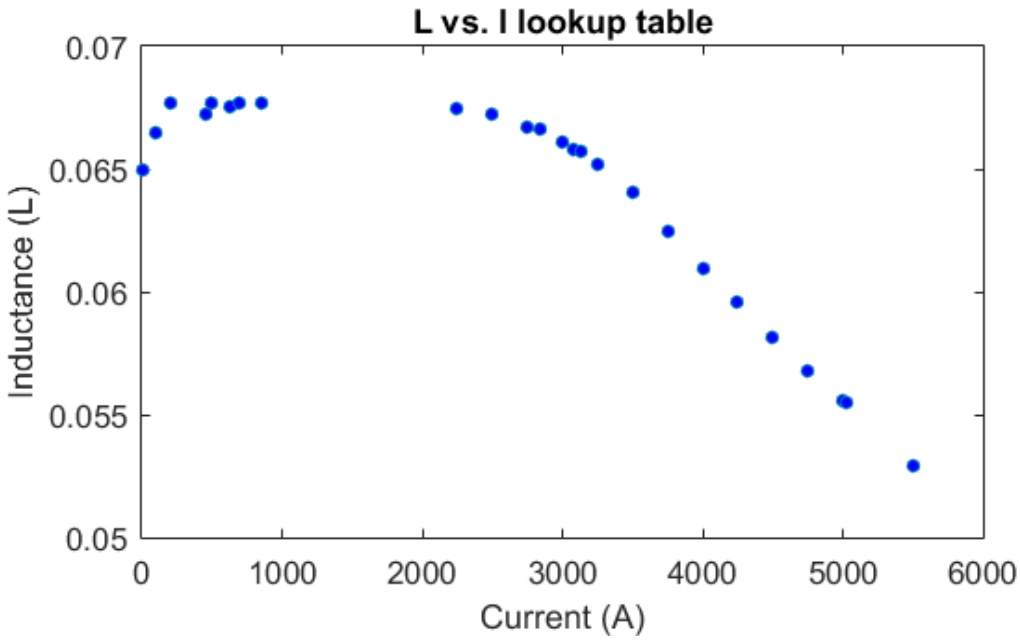

Figure 35: L vs. I lookup table values

5.2 System Identification

The aim is to find an accurate inductance variation with the current change to construct accurate *L vs. I* tables to be used in the DSP model. The magnet current and voltage data for a

magnet tap named *B1DSD9_5VT* is used for this analysis. For this particular voltage tap that is connected across dipole magnets, the *R* value is zero, so the model reduces to

$$V_c = L\frac{dI}{dt} \tag{7}$$

One of the techniques that can be applied to solve for *L* is the linear regression, where the explanatory variable is the first derivative of the current and the response variable is voltage. The voltage and current data from RHIC database is mined using custom algorithm written in MATLAB® [82], which is found to be quite noisy. Particularly if the derivative of current is taken, noise is highly amplified. Thus the data needs to be cleaned first. The frequency spectra of the current and voltage data are analyzed first, and their variation over time through spectrograms shown in Fig. 36.

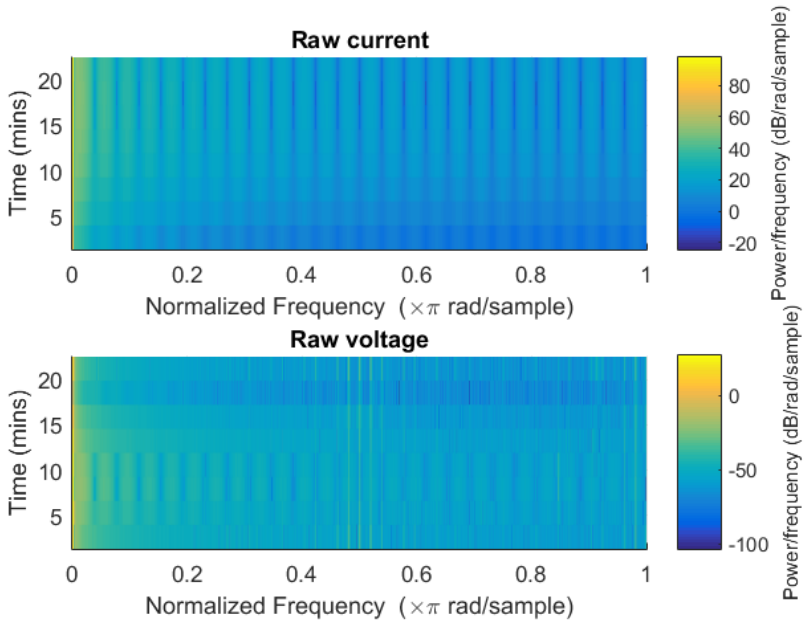

Figure 36: Spectrograms of voltage and current signals

Next a filter with suitable frequency characteristics derived from the spectrogram in Fig. 36 is used to filter the voltage and current data. The noise in the first derivative of current is now eliminated. Fig. 37 shows the filtered (green) and raw (black) signals for the magnet current, first derivative of the current and voltage signals. The periodic noise and spikes in the data are now removed.

Now the data is ready for analysis after the preliminary processing. Consider the *dI/dt* waveform in Fig. 37. There are certain portions of the current where the first derivative of the current is either zero or has very low value. For a good fit of the linear regression model, the explanatory variable should have a substantial magnitude. Thus to apply the regression algorithm using Eq. 7, small or zero values of *dI/dt* and corresponding values of *V* are eliminated from the data. A customized data classification algorithm is developed to segment and identify the regions in current waveform where the first derivative is non-zero, second derivative is non-zero etc. The segmented portions of the magnet current are shown in Fig. 38.

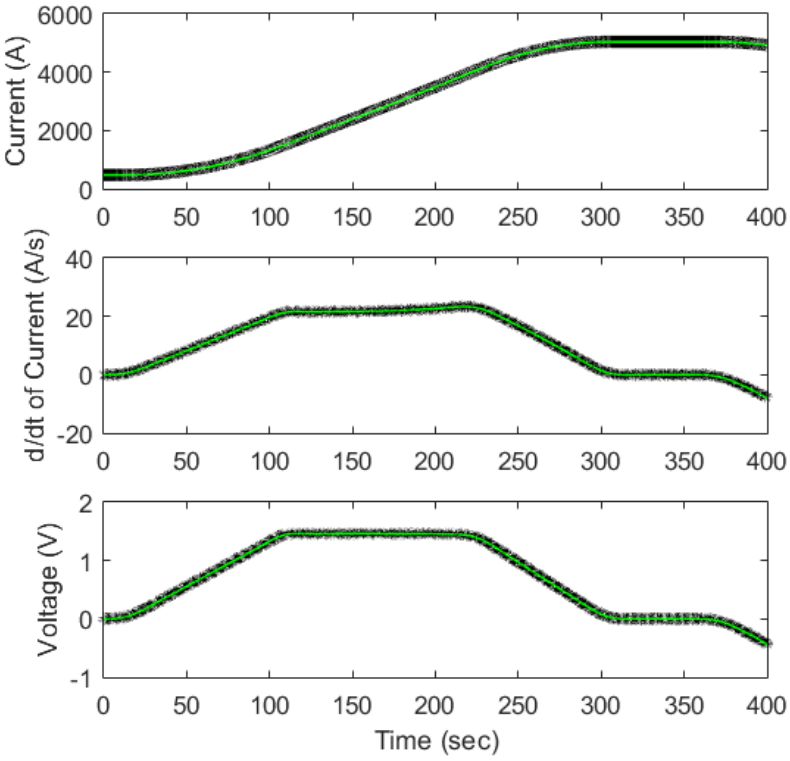

Figure 37: Raw and filtered I, dI/dt and V

Eq. 7 is used for regression in the regions where the first derivative exists. Next the nonlinear variation of *L* with increasing current is addressed. One method to deal with this is to use piecewise regression, where the current is divided into very small data sets, and regression is applied to each set for finding the *L* value. The *L* is assumed constant for this small dataset. These values of *L* with

I are plotted in Fig. 39 that show the saturation characteristics of *L* similar to Fig. 35, but with much smoother variation.

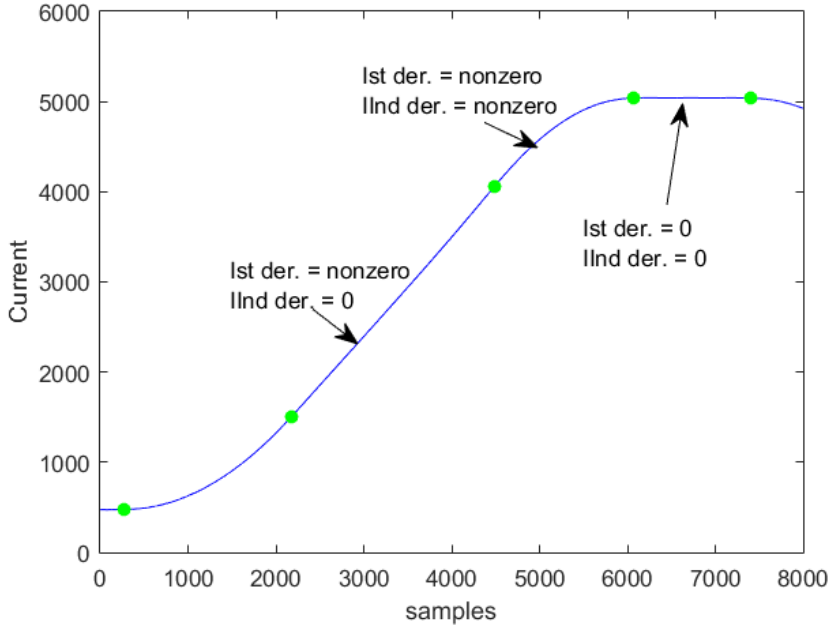

Figure 38: Current segmentation

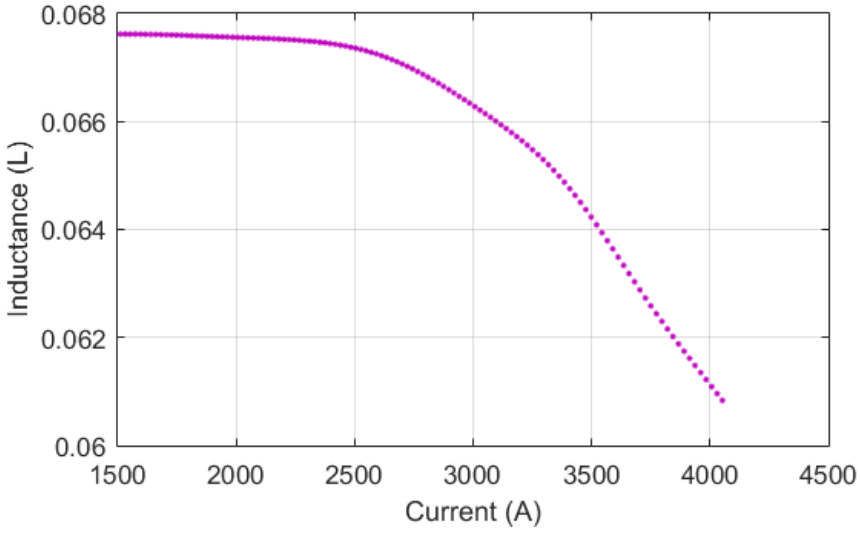

Figure 39: L vs. I curve from piecewise regression

5.3 Field Testing

Before testing the model in the field, the residuals obtained from the above analysis are studied. The residuals between the filtered voltage and the calculated voltage are shown in Fig. 40. As seen the maximum value of the residuals is about 8mV, which is well below the 25mV limit. Thus the *L vs I* values could be safely tested in the field.

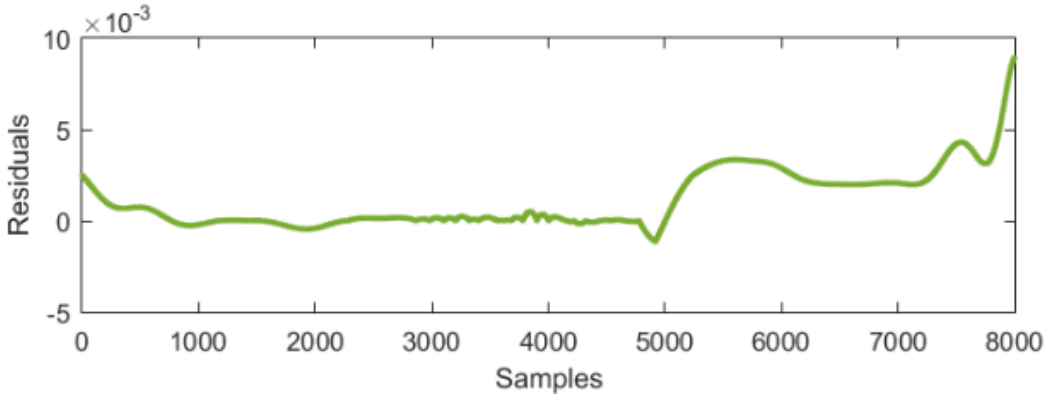

Figure 40: Residuals between the filtered and fitted voltage

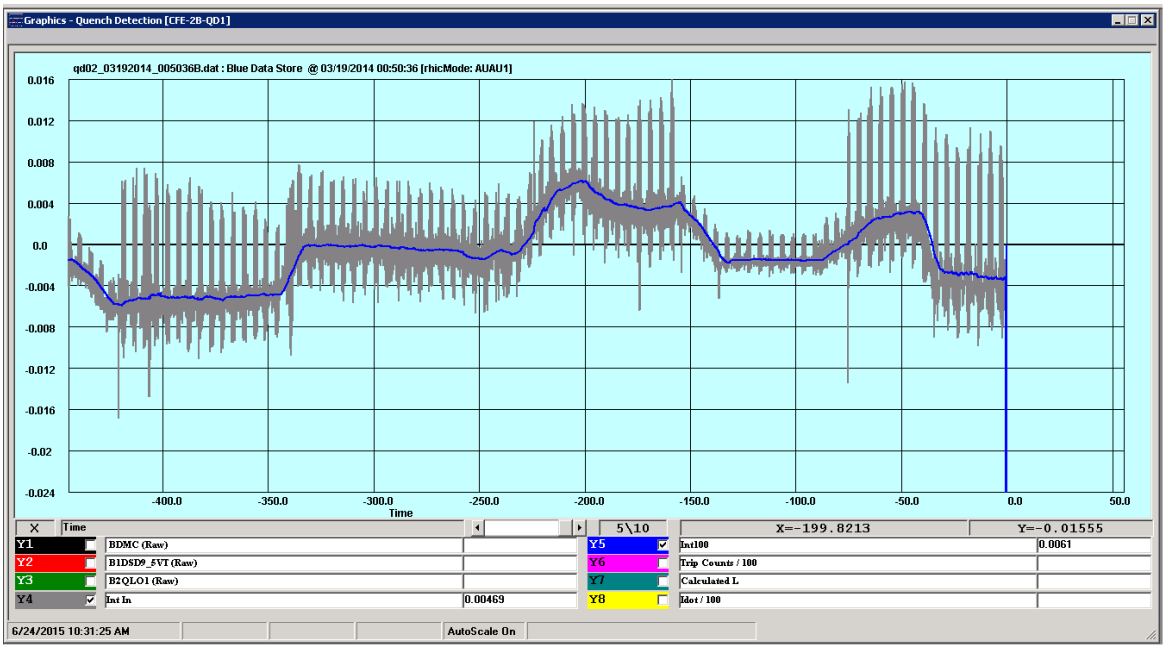

Figure 41: Field testing, quench trigger signal

The piecewise regression generates a smooth curve of about 200 data points for *L vs. I* curve (Fig. 39). However, the DSP model can only store 35 values of *L vs. I* data. It interpolates the *L* values for in-between *I* values. For employing the model in the field, *L vs. I* tables for DSP are generated using this data, and a screen shot from the field testing on the same voltage tap is shown in Fig. 41. The difference signal (in blue) is the moving average of 100 values of the actual voltage difference (in grey), which is used for triggering quench event in case it goes beyond 25mV. The maximum value of the trigger signal is found to be 6mV which is well below the 25mV level.

5.4 Discussion

To further improve the model, the remaining variability in the residuals has to be analyzed. As seen in Fig. 41, a pattern is seen in the residuals. This variation depicts a dependence on the second derivative of current, which is shown in Fig 42.

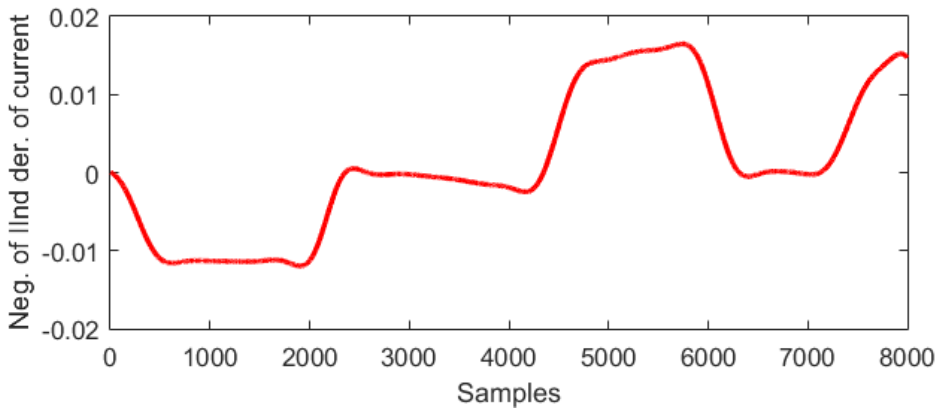

Figure 42: Negative of 2nd derivative of current

To accommodate this variance, the magnet model can be modified as the following equation.

$$V_c = L\frac{dI}{dt} + X\frac{d^2I}{dt^2}$$

Here X is a coefficient of second derivative of current, which can be a constant throughout the data, and might not need piecewise regression. This X parameter can be modeled as an additional eddy current component and/or parasitic capacitance in the magnet electrical circuit. For accurate analysis of such higher order terms, frequency response analysis can be performed for the magnets.

Chapter 6

Mathematical Model for Saturation and Hysteresis of Superconducting Magnet Inductance

As explained in chapter 5, a model based quench detection scheme is employed in RHIC for the protection of superconducting magnets. The quench detector model replicates the nominal electrical behavior of the superconducting magnets. A deviance of the magnet behavior from the model is detected as 'quench'. The RHIC dipole magnets are cosine theta magnets [72] that typically operate beyond saturation magnetization of the yoke. The quench detector model takes care of the saturation phenomenon by using lookup tables for the variation in inductance with applied current. The saturation curve for the magnet was obtained in chapter 5 that represented the decrease in inductance with increasing current.

The applied current ramps for the magnets are varied during the machine run-modes, which causes a change in the *L vs I* curve. Due to indeterminate nonlinear effects of saturation and hysteresis on the inductance, lookup tables for the inductance have to be modified manually with the introduction of a new ramp. In this chapter, a nonlinear mathematical model [44] is conceptualized that quantifies the change in magnet inductance with saturation and hysteresis, as the applied current ramp changes. First a mathematical equation is formulated to describe the saturation effect on inductance with applied current. Second, memory effect of hysteresis is conditioned over the saturation model with change in current ramp. The overall fitted mathematical model shows good compliance with the data. The empirical derivation of the mathematical model is based on analysis of historical data of RHIC magnets.

6.1 Problem Formulation

RHIC superconducting magnets are cosine theta magnets featuring cold steel yoke, and typically operate beyond the saturation magnetization of iron. Saturation effects are significant

[72] due to the placement of yoke inside the cryostat, directly surrounding the superconducting coil. The saturation of yoke causes the inductance of a magnet to decrease at higher currents.

The most dominant saturation effect is seen in the dipole magnets when they undergo current ramp cycle, characterized by a bottom and top level of the applied current [4]. The top level is typically 5093A in full energy runs corresponding to a magnetic field of 3.458T that drives the magnet into saturation. Fig. 43 shows a typical *L vs I* table stored in the DSP for a voltage tap named *B2DSA4_A3VT* (different from the one in chapter 5), for an up and down ramp. The *L* curve follows slightly different paths while ramping up and down, a typical effect of hysteresis.

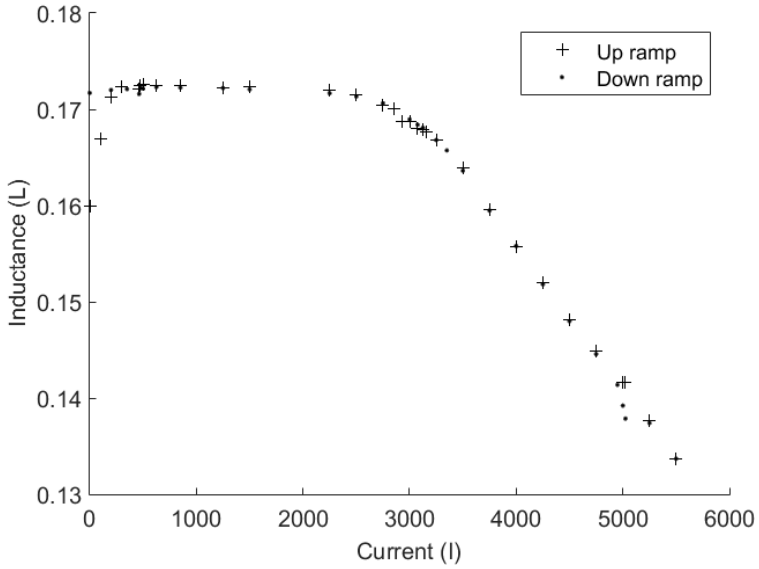

Figure 43: Lookup table data for L vs I saturation, for up and down ramp

When a magnet undergoes a specific ramp, the *L vs I* curve remains pretty same. As the ramp levels are altered, the curve changes, now with a different value of *L* for the same *I*. This is again due to hysteresis. RHIC operates on different particle energies, so the ramp cycle keeps changing. Due to indeterminate nature of *L* change, the lookup tables have to be calibrated manually to accommodate the changes due to hysteresis, for all 408 dipoles and numerous other magnets. This consumes precious time while RHIC is running at 4K temperature. Also, *L* has to be fine calibrated with a very tight tolerance to keep the voltage difference in the 25mV window. Limited accuracy of manual calibration increases the number of false failures. The aim is to develop a mathematical

model describing saturation and hysteresis behavior. This will facilitate the forecasting of more accurate *L vs I* tables so as to avoid the aforesaid problems.

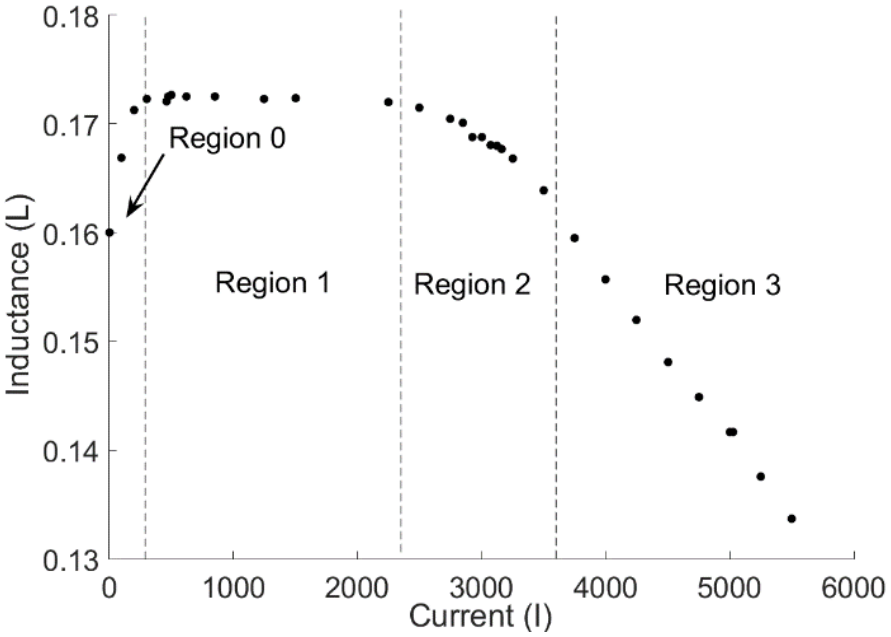

Figure 44: Magnetization as a function of applied field

To delineate a model for saturation and hysteresis together, first the saturation model is developed and then hysteresis phenomena is conditioned over it as a variation in model parameters. It is first necessary to understand the saturation behavior. Looking at Fig. 44, it is seen that *L* exhibits a regional behavior. *L* is linear in region 1 and 3, smoothly changing slopes in-between regions. This type of regional linear behavior cannot be accurately modeled by a finite degree polynomial. Also, it is apparent from RHIC operational experience that the change in *L* curve due to hysteresis has a memory and is related to the change in applied current cycle. The following sections explain the approaches followed to understand the *L vs I* variation. The formulation of saturation and hysteresis model is done step by step.

6.2 Saturation Model

For developing the saturation model, the magnet tap current and voltage data is first analyzed to find the underlying saturation characteristics of inductance as explained in chapter 5. The model is then tested on an analogous quantity 'transfer function' to check the goodness of fit.

6.2.1 Equation for Inductance Saturation

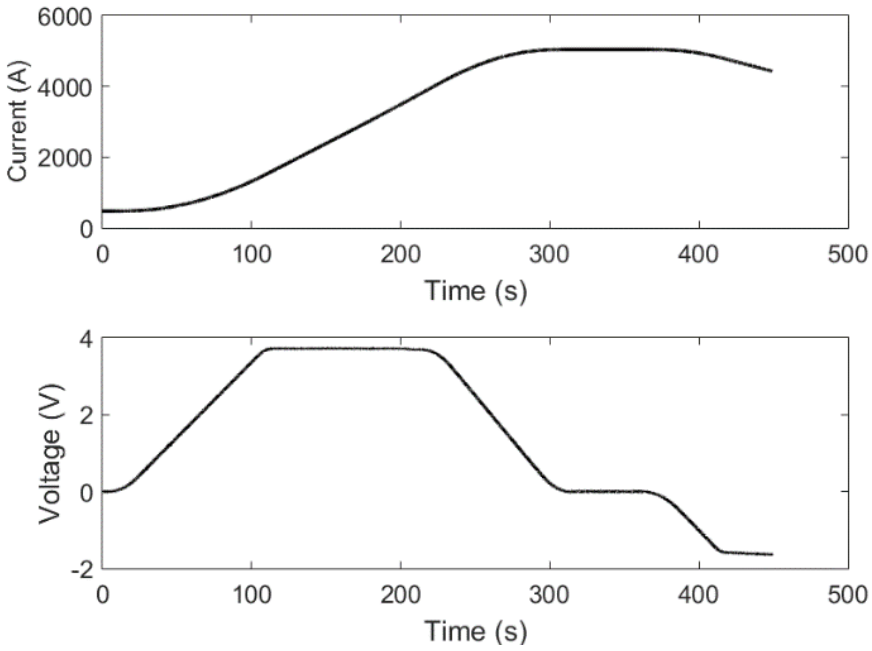

Figure 45: Magnet current ramp and the voltage developed across the tap

This section explains the mathematical model devised for the saturation effect. The inductance is obtained by analyzing the current and voltage data for the magnet tap named *B2DSA4_A3VT* that is connected across six dipole magnets. The relationship now becomes $V = L(I)\, dI/dt$ where V is the tap voltage, I is the tap current and $L(I)$ is the magnet inductance as a function of tap current. For practical purposes it is assumed that these magnets are identical in design. Across the tap, the magnets are connected in series and hence equal current flows through all of them. The equivalent inductance of the circuit is a series combination of all six inductances with similar saturation characteristics and hence it is assumed as a single inductance undergoing saturation. Fig. 45 shows the current and voltage signal across this tap. Fig. 46 shows the *L vs I* curve obtained

as per the method explained in chapter 5. Inductance decreases with increasing current in a nonlinear fashion. This *L vs I* data is obtained from piecewise regression. The curve is divided into regions 1, 2 and 3.

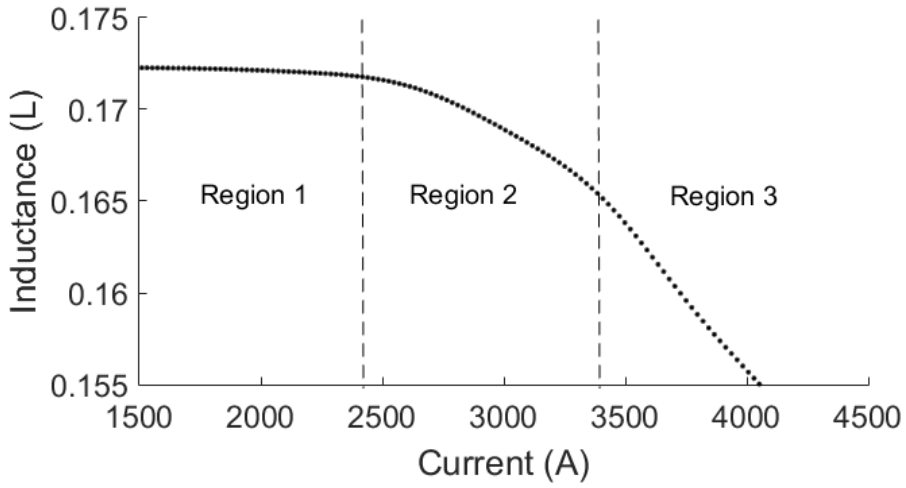

Figure 46: Saturation effect on inductance with increasing current.

Approaching the mathematical model, it is seen that the *L* stays pretty constant in region 1 i.e. for the lower values of current. This can be modeled by a constant term. After a certain current (around 2400A), the *L* value curves down and attains a linear fall. A combination of logarithmic and exponential term is used here to model such kind of regional behavior. If the linear regions are extended, then their intersection point is defined as the saturation corner current. Hereby, a new mathematical model is proposed that explains the saturation in *L* as a function of *I*. The equation is

$$L = L_0 - \frac{b}{a}\ln\left(1 + e^{\left(\frac{I - I_S}{b}\right)}\right) \tag{8}$$

Where:

L_0 = constant inductance in region 1

I_s = saturation corner current, where the asymptotes to linear regions 1 and 3 intersect.

a = inverse of the slope of linear region 3

b = defines the curvature of region 2

I = magnet current as a variable

For $I<<Is$, the logarithmic term in the Eq. 8 is negligible, and hence $L=L_0$. When $I>>Is$, then the second term becomes a linear term and $L=L_0-(I-I_s)/a$. The b term appears at two places in the equation. In this way the slope of region 3 is dependent only on the parameter a. If b is not used at both places, then b and a do not control the curve shape independently, especially in region 2 and 3. For modeling hysteresis, all four parameters of the equation have to be independent of each other, as explained in section 6.3. Fig. 47 explains how the four parameters independently control the curve shape. Equation parameter are varied one by one, with other parameters kept constant.

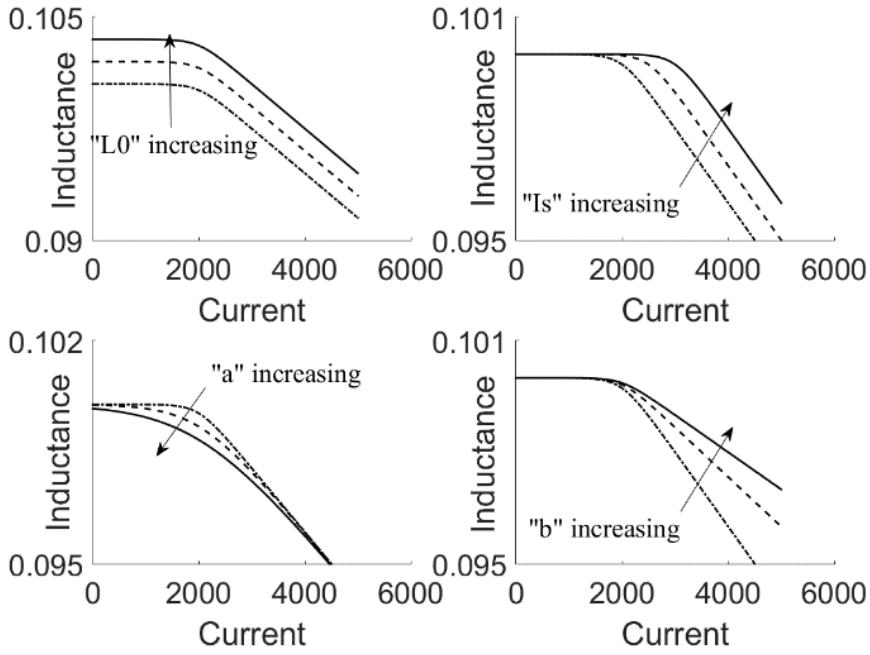

Figure 47: Variation of equation parameters

To fit the proposed equation on the *L vs I* data, nonlinear regression is used in MATLAB® with trust region algorithm [82]. Fig. 48 shows the fitted curve vs the data at the top, and the residuals at the bottom.

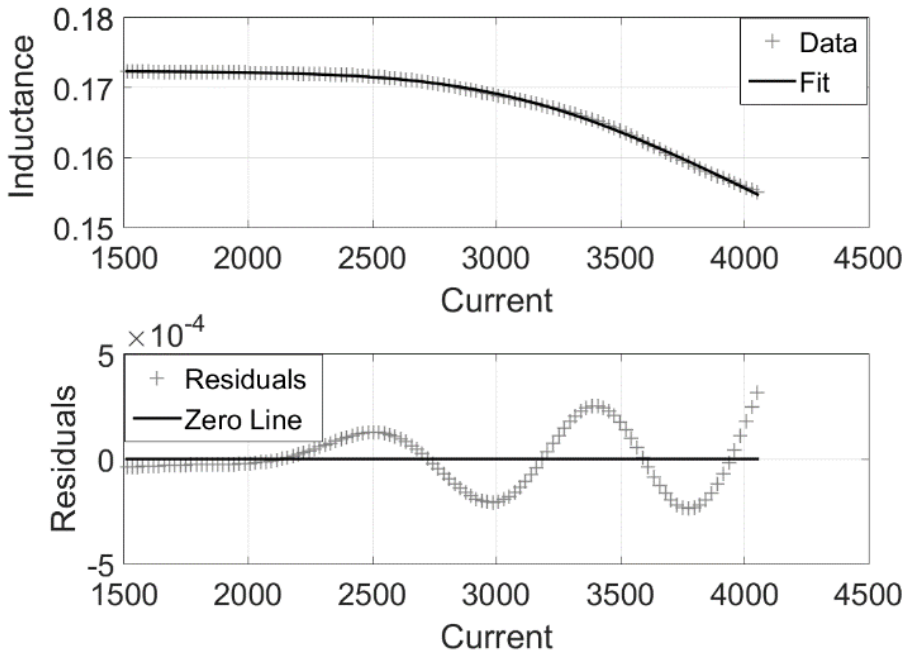

Figure 48: Top – *L vs I* data and fitted equation, Bottom – residuals of the fit

The fitted equation parameters and the goodness-of-fit statistics for this data set are:

Model: $L = L_0 - \frac{b}{a}\ln\left(1 + e^{\left(\frac{I-I_S}{b}\right)}\right)$

Coefficients (with 95% confidence bounds):

L_0 = 0.1724 (0.1723, 0.1724)

I_s = 3123 (3091, 3156)

a = 5.373e+04 (5.184e+04, 5.563e+04)

b = 331 (315.7, 346.4)

Goodness of fit:

SSE: 1.873e-06

R-square: 0.9994

Adjusted R-square: 0.9994

RMSE: 0.0001293

Here *SSE* stands for Sum of Squares due to Error and *RMSE* stands for Root Mean Squared Error. Variance of 99.94% in data is explained by the equation, which is a good fit. It is to be noted that above equation is valid only for low saturation of the magnet. As the magnet saturates more and more, the field contribution due to the coil starts increasing and that of the yoke becomes constant. At very high currents the magnet saturates fully and the inductance becomes constant. The model can be extended for higher saturation by adding other terms in Eq. 8. RHIC magnets are however never driven to high saturation. The main task here is to model the magnet behavior in the operating range of the superconducting magnets. This equation can be extended for higher saturation by further analysis if the data becomes available.

Though the magnets across the voltage tap have the same design and are very precisely constructed [4], slight variations in the construction are unavoidable. As this curve is a summation of the L saturation curves for six superconducting magnets, small differences in individual saturation curves can be apparent on the residual plot. The unexplained variance in R-square statistic could be due to other factors that sift through the regression, like transient response, eddy currents, parasitic capacitances and mutual inductances in the magnet circuit. Nonetheless Eq. 8 is a good fit to the data available. To verify this equation, an analogous quantity to the inductance of the magnet is analyzed.

6.2.2 Verification of Saturation Model

The verification of the saturation model is done by alternative interpretation to the inductance of the magnet. The inductance of the magnet is proportional to the product of square of the transfer function $f_t(I)$ and the effective length $l_{eff}(I)$ of the magnet as shown by [4] [43] [85] [45] [86]. Both the transfer function and the effective length are a function of the magnet current.

$$L \propto (f_t(I))^2 * l_{eff}(I)$$

$$f_t(I) = \frac{B_0}{I}$$

Here B_0 is the average dipole magnetic field inside the magnet, and I is the magnet current. At very high saturation, the effective length changes a little, but this effect can be neglected for the RHIC magnets as the they are not driven to high saturation. Thus inductance is equivalent to $(B_0/I)^2$.

Fig. 49 and Fig. 50 show the square of the transfer function of the magnet plotted against the magnet current for an individual arc dipole magnet *DRG112* for up and down current ramp [87].

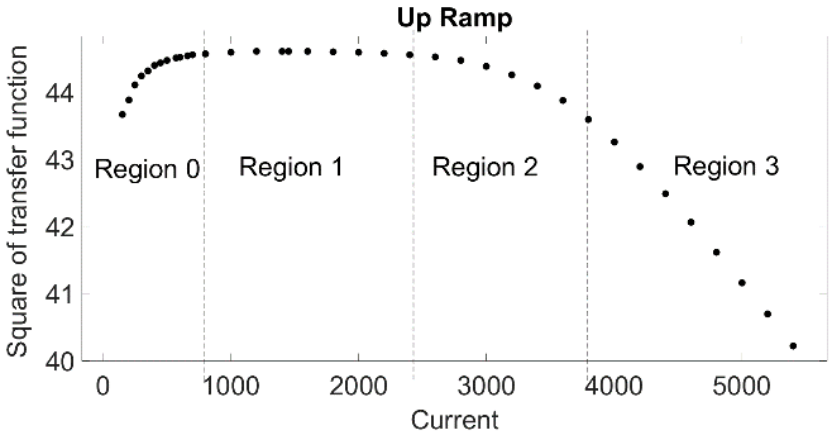

Figure 49: Magnetization curve for up ramp.

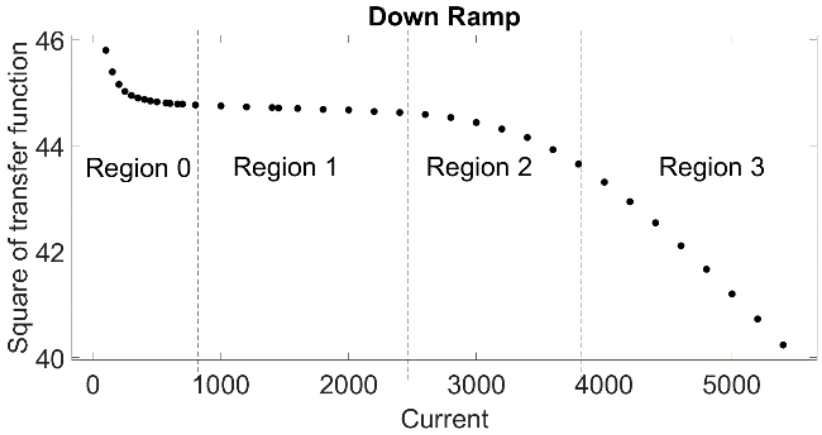

Figure 50: Magnetization curve for down ramp.

The transfer function is measured as the mean of the magnet transfer function over the length of the magnet, with the current linearly ramped at 80A/sec between 100A and 5400A. These curves are segmented in 4 regions: 0, 1, 2 and 3. Variations in regions 1, 2 and 3 of Fig. 49 and Fig. 50 are same as in Fig. 46 and correspond to Eq. 8. These curves are smooth and free from the summation of saturation characteristics of different magnets. Thus it can serve as a baseline for the model in Eq. 8. However, in region 0, a small initial fall during the up ramp and a small rise during the down ramp is observed. This is another regional behavior which is modeled by adding

other exponential terms to the equation for up and down ramp separately. For up ramp the equation modifies to

$$L = L_0 - \frac{b}{a}\ln\left(1 + e^{\left(\frac{I-I_S}{b}\right)}\right) - e^{\frac{-hI}{g}} \tag{9}$$

Where *h* and *g* are constants defining region 0 shape. For down ramp the same exponential term is added to the equation. Moreover, for the down ramp, a slight slope is seen in region 1. This can be modelled by an extra term *m*I* inside the logarithmic term to represent the slope.

$$L = L_0 - \frac{b}{a}\ln\left(1 + mI + e^{\left(\frac{I-I_S}{b}\right)}\right) + e^{\frac{-hI}{g}} \tag{10}$$

Here *m* is a constant to model the slope of region 1. The same fitting algorithm is used here as explained in section 6.2.1. Fig. 51 and Fig. 52 show the fitted curves (on top) and residuals (on bottom) for Eq. 9 and Eq. 10 on the data of Fig. 49 and Fig. 50. Also shown are the equation parameters and goodness of fit.

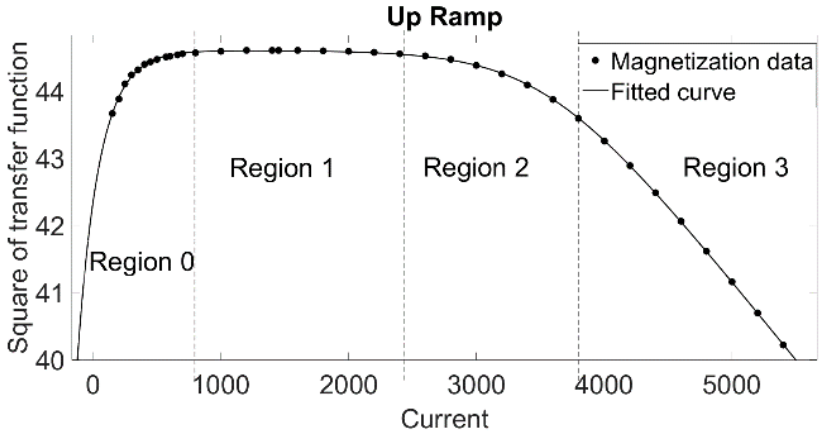

Figure 51: Magnetization curve for up ramp with fitted equation

Coefficients (with 95% confidence bounds):

L_0 = 44.61 (44.6, 44.62)

I_s = 3550 (3529, 3571)

a = 423.2 (417.5, 428.9)

b = 413.7 (400.1, 427.3)

h = 0.005364 (0.00517, 0.005558)

g = 0.4732 (0.455, 0.4915)

Goodness of fit:

SSE: 0.00299

R-square: 0.9999

Adjusted R-square: 0.9999

RMSE: 0.009822

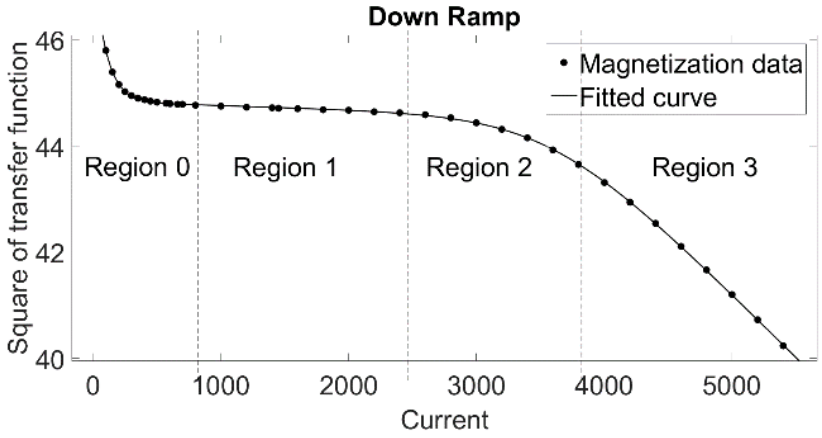

Figure 52: Magnetization curve for down ramp with fitted equation

Coefficients (with 95% confidence bounds):

L_0 = 44.84 (44.83, 44.86)

I_s = 3482 (3452, 3512)

a = 419.3 (412.6, 426)

b = 385.4 (365.2, 405.7)

h = 0.01025 (0.009721, 0.01079)

g = 0.3751 (0.3529, 0.3972)

m = 9.202e-05 (7.246e-05, 11.16e-05)

Goodness of fit:

SSE: 0.003489

R-square: 0.9999

Adjusted R-square: 0.9999

RMSE: 0.01061

The slope of region 1 is negligible, so it can be ignored. The goodness of fit is almost perfect hence it can be said that saturation phenomena can be described precisely with the Eq. 9 and Eq. 10.

6.3 Memory Model for Hysteresis

The hysteresis [88] of the magnets is conditioned over the saturation model of section 6.2. As the current ramp applied to magnets is changed, the saturation curves also change, now with different value of inductance for the same current, however the shape of the curve remains the same. The saturation model of section 6.2 is fitted on these new curves, where the change due to hysteresis is reflected as the change in the equation parameters *L0, Is, a* and *b.* This change in equation parameters is related to the change in current ramp characteristics for the hysteresis model. It is necessary that these saturation equation parameters are independent of each other, so that the change in each parameter can be related independently to the current ramp changes (as stated in section 6.2). To incorporate memory in the model, the parameters of the previous current ramp are used along with the present current ramp. The region of interest for the hysteresis model is when RHIC is operational with the particle beams circulating inside the machine. During this state, magnet currents are generally in the region 1, 2 and 3 from Fig. 44. Thus to establish the hysteresis model, the Eq. 8 is chosen, with four parameters L_0, I_s, *a* and *b*, and omitting the parameters *h* and *g* associated with region 0. These four parameters completely define the behavior of *L vs I* during RHIC operation. The hysteresis models for up and down ramps are established separately.

The current and voltage data for the voltage tap *B2DSA4_A3VT* is analyzed for all the current ramps of RHIC operation, from year 2000 to 2014 [89]. The equation parameters for all these data sets are obtained and they are categorized according to the *run modes*. In a particular run mode, the current ramp cycle for a dipole magnet is unaltered, thus the equation parameters during that time period have minimal variance. Fig. 53 shows the equation parameters for all current ramps during run mode *2B* in year 2011, and the associated small variance.

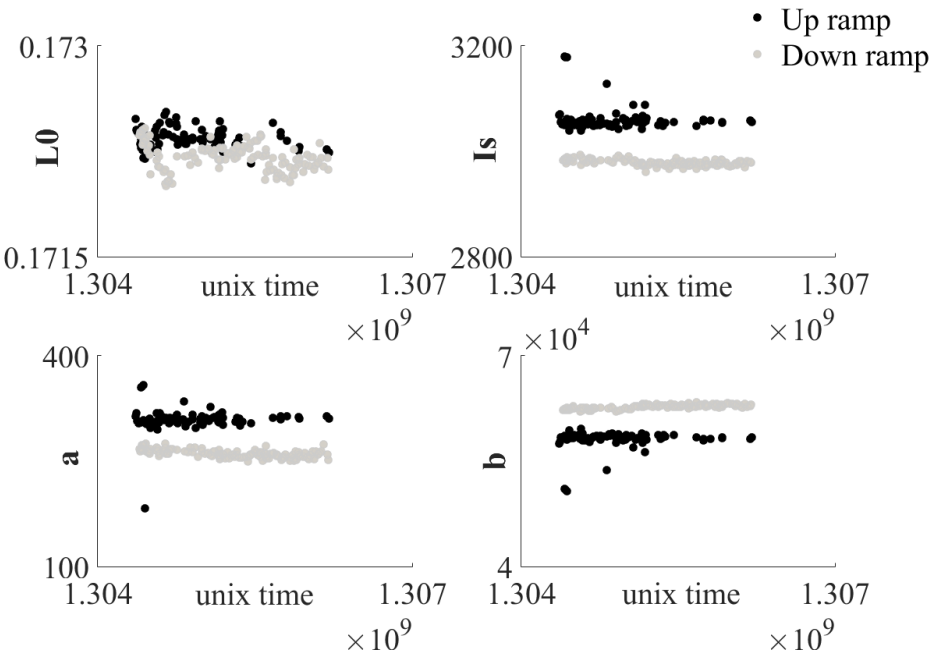

Figure 53: Saturation equation parameters for run mode 11-2B

However, there are some outliers for the equation parameters that denote the current ramp cycles during the cycling of dipole magnets. To reduce the effect of outliers, the medians of these equation parameters are chosen as explanatory variables representing a particular mode in the memory model [70]. Not all run modes are *energy run modes* that drive the magnets into saturation. Overall 8 data points are generated for the memory modeling, pertaining to run modes where the magnets were driven well beyond the saturation corner current, and well fitted saturation equation parameters were obtained for this analysis.

After obtaining the values of equation parameters for individual run modes, they need to be related to the ramp characteristics. A ramp is characterized by its flat top level, flat bottom level and ramp rate. Fig. 54 shows a typical ramp with its characteristics.

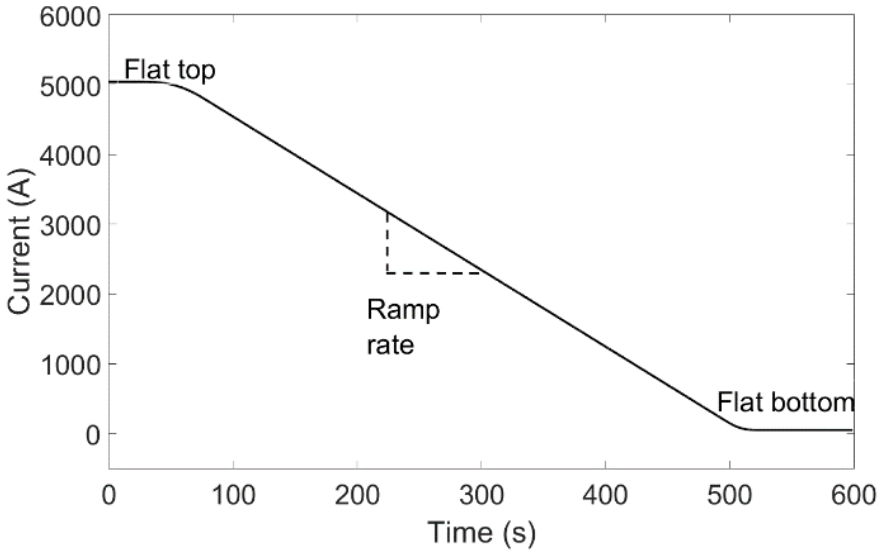

Figure 54: Typical down current ramp.

The ramp rate is fixed during the machine operation. Also the magnets are always driven to flat bottom current of 50A, irrespective of different current level at which particle beam is injected in RHIC. So only the flat top current is variable with the ramp type. This serves as the first explanatory variable in the hysteresis model.

The *L vs I* curve of the magnet is dependent on the current ramp that is being applied to the magnet. Moreover, it is observed that this curve also has a memory, i.e. the curve will depend on the ramp type that was used preceding to the present current ramp [90]. The difference between the present ramp flat top and the previous ramp flat top as serves as the second explanatory variable that incorporates memory. Quadratic stepwise regression in MATLAB® [82] is used for each saturation equation parameter, chosen as the response variable and the above two as explanatory variables. The models are shown in Table 9 and Table 10 for the saturation equation parameters for the up and down ramp of the magnet circuit across the *B2DSA4_A3VT* voltage tap, with the goodness of fit as indicated. Variable *x* is the present flat top ramp, and variable *y* is the difference between present and previous ramp flat top.

Table 9: Memory model for up ramp

Regression model for up ramp parameters
$L_0 = c_0 + c_1 x + c_2 x^2$
c_0 = 0.147, c_1 = 1.05e-5, c_2 = -1.09e-9
Goodness-of-fit: R^2 = 0.924
$I_s = c_0 + c_1 x + c_2 y + c_3 xy + c_4 x^2$
c_0 = -3.41e4, c_1 = 15.44, c_2 = -0.827, c_3 = 1.6e-4, c_4 = 1.6e-3
Goodness-of-fit: R^2 = 0.998
$a = c_0 + c_1 x + c_2 y + c_3 xy + c_4 x^2$
c_0 = 2.89e6, c_1 = -1.169e3, c_2 = 55.76, c_3 = -0.01, c_4 =0.12
Goodness-of-fit: R^2 = 0.999
$b = c_0 + c_1 x + c_2 y + c_3 xy + c_4 x^2$
c_0 = -1.26e4, c_1 = 5.38, c_2 = -0.227, c_3 = 5.36e-5, c_4 = 5.61e-4
Goodness-of-fit: R^2 = 0.996

Table 10: Memory model for down ramp

Regression model for down ramp parameters
$L_0 = c_0 + c_1 x + c_2 y + c_3 xy + c_4 x^2$
c_0 = 0.25, c_1 = -3.22e-5, c_2 = -1.01e-5, c_3 = -2e-9, c_4 = 3.29e-9
R^2 = 0.925
$I_s = c_0 + c_1 x + c_2 y + c_3 xy$
c_0 = 3.73e3, c_1 = -0.148, c_2 = -0.158, c_3 = 3.14e-5
R^2 = 0.995
$a = c_0 + c_1 x + c_2 y + c_3 xy + c_4 x^2$
c_0 = -2.06e5, c_1 = 97.91, c_2 = -15.51, c_3 = 0.003, c_4 = -0.009
R^2 = 0.999
$b = c_0 + c_1 x + c_2 y + c_3 xy$
c_0 = 834.05, c_1 = -0.115, c_2 = 0.31, c_3 = -6.15e-5
R^2 = 0.933

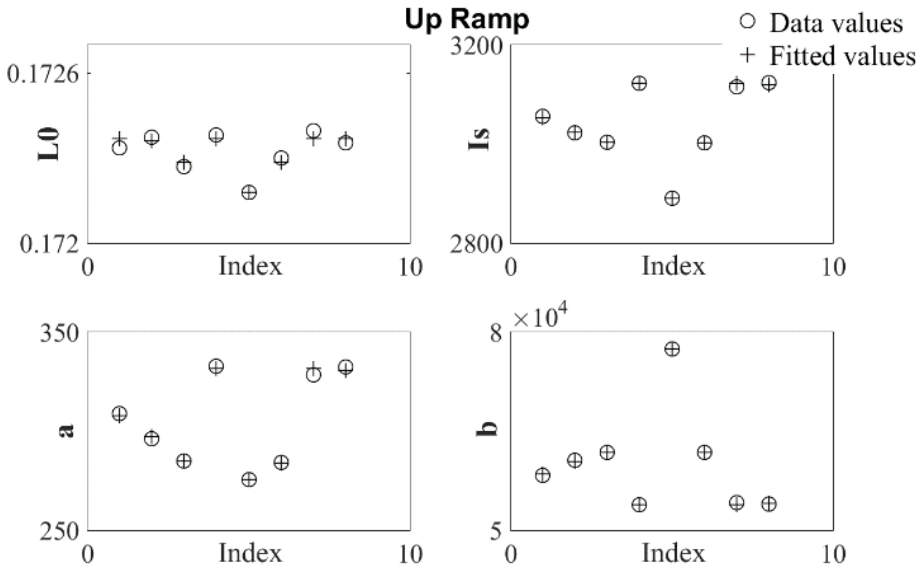

Figure 55: Up ramp equation parameter data and fitted memory model

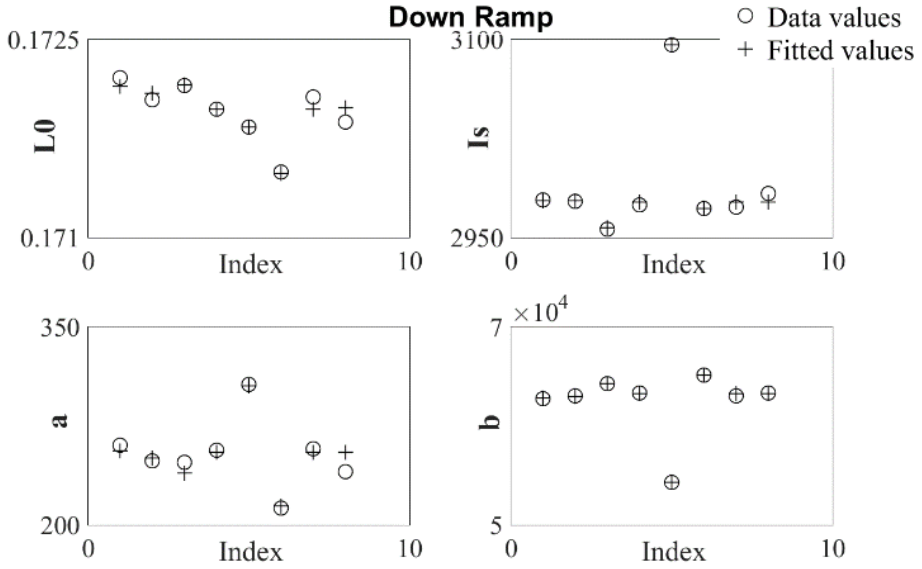

Figure 56: Down ramp equation parameter data and fitted memory model

Fig. 55 and Fig. 56 show the equation parameters data vs the fitted values through the above model. The regression models above are a good fit to the data. Thus it is established that the hysteresis modifies the *L vs I* curve in such a way that it reflects as a change in the saturation equation parameters. And this change is quantifiable in terms of the applied current ramp

characteristics, both present and past. However, it is difficult to parameterize this hysteresis model because of the small data set available.

The saturation and hysteresis behavior can now be predicted for RHIC magnets, if future ramp parameters are specified. This will help reduce the manual calibration effort required for *L vs I* lookup tables every time a new ramp cycle is introduced.

This combined model is valid only for the low saturation where the inductance corresponding to the high current values keeps a constant negative slope. High saturation can be modeled by adding similar exponential or log of exponential terms in the saturation equation (Eq. 8) that can help define the regional behavior. This is contingent upon the availability and further analysis of data for high saturation region. And subsequently a similar approach can be followed for developing a memory model for the extra parameters. More information on the magnetic material of RHIC magnets is given in [4] [91].

Chapter 7

Future Collider eRHIC: Vision Towards the Design of Machine Protection

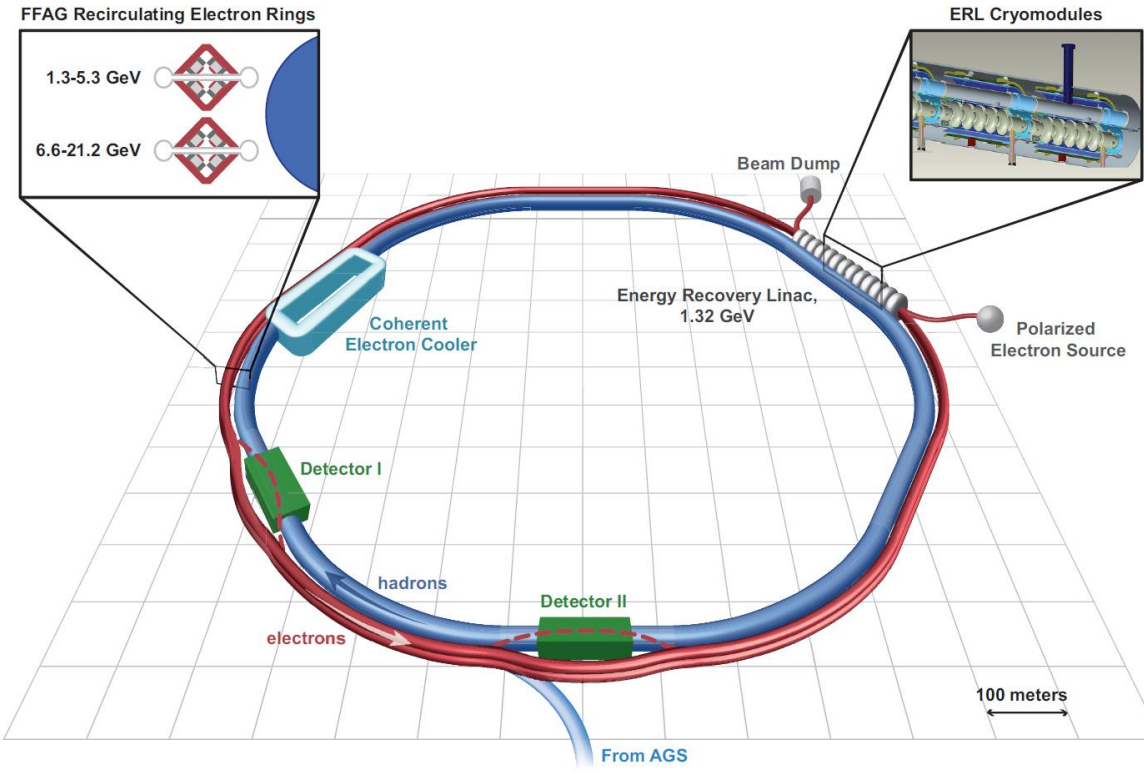

Figure 57: eRHIC layout

The electron-ion collider, eRHIC [92] [93] at Brookhaven National Laboratory (Fig. 57), is an upcoming major research project that will be built on the existing RHIC facility. The mission of eRHIC is to advance the long-term vision for Nuclear Physics to discover and understand the emergent phenomena of Quantum Chromodynamics (QCD), the fundamental theory of the strong interaction that binds the atomic nucleus.

The exploration of nucleon structure and nuclear interactions at high energies in recent decades has brought forth many discoveries. It has opened new avenues for the study of fundamental properties of strongly interacting matter and the role of QCD in the formation and structure of our natural world. A broad consensus now exists that calls for a new facility like eRHIC to collide high-energy beams of electrons with beams of nucleons and heavy ions. Such a facility should have the specific capabilities to explore the structure of QCD matter featuring

1. Sufficient intensity to access the gluon dominated regime
2. Polarized beams to enable a complete picture of the spin structure of the nucleon
3. Electromagnetic probes having unprecedented statistical precision at high enough energies

7.1 Introduction to eRHIC

The eRHIC [93] is based on the existing RHIC hadron facility with its two intersecting superconducting rings, each 3.8 km in circumference. A polarized electron beam with an energy up to 21 GeV would collide with a number of ion species accelerated in the existing RHIC accelerator complex, from polarized protons with a top energy of 250 GeV to fully-stripped uranium ions with energies up to 100 GeV/u. Using the present significant margin of the RHIC superconducting magnets, the maximum beam energy could be increased by 10 or more percent. The eRHIC design is based on using one of the two RHIC hadron rings and a multipass Energy Recovery Linac (ERL). Using an ERL as the electron accelerator assures high luminosity of the beam. Most of the electron accelerator components, including the injector, the ERL and the recirculation passes, will be located inside the RHIC tunnel. eRHIC will be able to provide electron-hadron collisions in up to three interaction regions. To reach the required performance, eRHIC will employ several novel technologies such as a polarized electron gun delivering a current of 50 mA, strong hadron beam cooling using Coherent electron Cooling (CeC), high current multi-pass ERL, and acceleration of polarized He to high energy. The accelerator design of the electron-hadron collider has been developed to fulfill the following eRHIC physics goals [72].

- Hadron species: polarized protons (up to 250 GeV), polarized $^{3}He^{+2}$ ions (up to 167 GeV/u), heavy ions (typically $^{197}Au^{+79}$ or $^{238}U^{+92}$ ions, up to 100 GeV/u)

- Polarized electrons: in the range from 2 GeV up to 21 GeV
- The luminosity: 10^{33} - 10^{34} $cm^{-2}s^{-1}$ in terms of e-nucleon collisions

The key goal of the eRHIC accelerator design [92] has been to achieve the required high-energy, high-luminosity performance at a realizable machine construction cost. For the hadron part of the machine, eRHIC takes advantage of the existing RHIC accelerator complex, including the full suite of injector systems for polarized protons and fully stripped heavy ions. The new electron accelerator is achieved through a cost-effective design, taking advantage of significant recent advances in accelerator technology. As shown in Fig. 57, the eRHIC facility uses one of the RHIC hadron beams (the clockwise moving "blue" beam), with a high energy electron beam counter-rotating in the same tunnel, and collisions occurring in two intersection regions occupying the present experimental areas of the STAR(IR6) and PHENIX (IR8) detectors. The major eRHIC accelerator components are:

- The 12 MeV injection complex includes a high-current polarized beam injector and 12 MeV linear accelerator. A beam dump for disposing of the 12 MeV decelerated beam is also located in this area.
- The 1.322 GeV Energy Recovery Linac is 120 m long and consists of a string of superconducting 422 MHz cavities. The use of energy recovery technology in the main accelerator linac is essential to reach a high value (50mA) of the electron average current. Additional RF cavities (844 MHz) are used to replenish the beam energy loss caused predominantly by synchrotron radiation. Also, 2.1 GHz cavities are utilized for reducing the beam energy spread.
- Two vertically stacked recirculation beamlines run around the RHIC tunnel circumference, outside of the hadron ring. The optics of each of the beamlines is based on a Fixed Field Alternating Gradient (FFAG) lattice, which is capable of transporting beams of different energies within a common vacuum chamber. The first FFAG beamline transports electrons with energies from 1.3 GeV to 6.6 GeV. The second FFAG beamline is used to pass beams in the 7.9-21.2 GeV range. The magnetic structure of both beamlines is based on permanent magnets.
- A spreader and a combiner are placed either side of the ERL for proper distribution and matching of the electron beams of different energies between the ERL and FFAG

beamlines. Both the spreader and the combiner have arms that will be used for transport of beams of particular energies, for optics matching, path length correction and betatron phase adjustments.

- A cooling device achieves cooling of the proton and ion beams. The device will employ the Coherent Electron Cooling technique for efficient cooling in longitudinal and transverse planes.
- The electron-hadron collisions occur in two interaction regions. Near these interaction regions electrons are extracted from the FFAG beamline using a septum magnet and directed into a dedicated beamline towards the experimental detectors. The interaction regions include superconducting magnets and provide strong beam focusing. Crab cavities are employed to prevent loss of luminosity.

7.2 The eRHIC Machine Protection

The eRHIC machine protection systems will be modeled on the design of the RHIC machine protection systems [31], although adapted to the eRHIC requirements. The machine protection systems will include a beam permit system that has inputs from loss monitors, power supplies, superconducting RF monitors, vacuum chamber heating monitors, water temperature, quench detectors, access controls systems, vacuum monitors, and longer term beam lifetime or slow loss monitors. Beam aborted from eRHIC will go into one of three beam dump systems, depending on the energy and what part of the acceleration/deceleration cycle a given beam is in. As there will be more systems participating in eRHIC operation, the number of input-output channels can scale to 10 times. In general, the eRHIC systems and the RHIC systems are independent. An interlock that dumps the electron beam does not need to cause the beam in RHIC to be aborted and a RHIC beam abort does not need to cause an electron beam abort. There are three systems associated with the machine protection and beam abort systems; the beam permit link, the abort kicker systems, and the beam dumps. The beam permit link is the interface to the network of devices that participate in the beam permit. The kicker systems monitor the beam permit link and will abort the beam if the permit carrier is dropped.

7.2.1 Machine Protection Requirements

Since eRHIC uses an ERL [31], the electron beam current in the ERL must remain balanced throughout the acceleration/deceleration process. So eRHIC will be brought on by slowly ramping the electron beam current until it meets the required intensities for operation. Once eRHIC is on and electrons are cycling through the systems, it remains on indefinitely. This is different from RHIC, which injects, ramps, stores, and then dumps the beams at the end of a store.

eRHIC beam losses can be classified into one of five groups [94]

- Ultra-fast Losses occur in < 6 turns, or 77 μsec
- Fast Losses occur in > 77 μsec & < 10 msec
- Intermediate Losses occur in < 10 sec
- Slow Losses occur in < 100 sec
- Steady State Anything > 100 sec

For Ultra-fast losses only passive components can protect equipment (e.g., absorbers). For eRHIC there will be collimation systems, which will mainly be intended to reduce experiment background radiation but will also be the limiting aperture during collisions. For fast losses the beam loss monitors can be used to protect systems by triggering a beam abort when the losses exceed thresholds. Intermediate losses may not exceed fast loss monitor thresholds but could still deposit too much heat into a cryogenic system, so the quench protection system will cause an abort when a superconducting magnet or RF cavity quenches. When fault times are slow enough, preemptive systems, such as automatically reducing beam currents, are being considered, avoiding actual beam aborts all together. For intermediate or slow beam losses, such systems can be employed. Understanding how much damage a given amount of deposited energy can cause is strongly dependent on the energy density (Joules per unit volume) as well as the time to deposit that energy in some given material [95]. However, some fault scenarios for eRHIC have been evaluated making it clear that the beams will have the potential to do significant damage.

Table 11: eRHIC beam energy content

Parameter	e^-	p	$^2He^3$	$^{79}Au^{197}$	$^{92}U^{238}$	Unit
E	10	250	167	100	100	GeV/n
n_b	180	111	111	111	111	
I_b	3.6	2	6	6	6	10^{10}
E_d	62*	89	178	107	107	kJ

*Assumes 6 turns, each with 180 bunches.

Table 11 shows how much energy each of the different eRHIC beams will deposit when dumped [30] [31]. In this table E is the energy of the beams in GeV/nucleon, n_b is the number of bunches in a dump, I_b is the intensity per bunch in units of 10^{10} nucleons, and E_d is the amount of energy deposited, in kilo-joules, when these beams are dumped. The positive ion beams are dumped at high energy at the end of a store as well as during a beam abort event. The electron beams will only be dumped at the high energies when there is a beam abort event. For normal operations the electrons are dumped at low energy. While the electron beams do not deposit as much energy as the hadron beams, they are still at levels that could be damaging to equipment. Note that the planned intensities for protons and ions for eRHIC are much lower than RHIC currently achieves. Slow and steady state losses are not anticipated to be significant. Individual electron bunches only exist in eRHIC for 160 microseconds. Beam losses can come from the Touschek effect, in which intrabeam particles collide with large angle scattering. Intrabeam scattering from Coulomb interactions (both small and large angle scattering) will also occur in eRHIC, but this is more likely to change beam distributions and not cause beam loss. Losses can also occur from beam-gas interactions, which are predicted to be at tolerable levels. There are two types of these interactions, elastic scattering and Bremsstrahlung, in which particles scatter from nuclei. The eRHIC BPS will be similar to the RHIC system, but with a single carrier link (or set of links) for all systems. In addition, certain systems will need to have faster and more sophisticated protection than the standard RHIC BPS can provide.

7.2.2 Risks and Responsibilities of MPS

The eRHIC will incorporate systems related to acceleration and collision of both positive particles and electrons. This hybrid design will introduce the complexities and risks associated with both an electron and a positive ion accelerator. Also eRHIC will use novel technologies like superconducting RF, coherent electron cooling device, energy recovery linac systems, Gatling electron gun for high current generation and other supporting systems. In addition to the machine protection issues of RHIC, following challenges [96] [92] [93] are foreseen for eRHIC:

Particle Beams and Synchrotron Radiation

- At a given bunch intensity, the eRHIC hadron bunch is much denser than the RHIC bunch due to cooling. This higher charge density can result into intense beam losses in case of beam deviation, that calls for more sensitive equipment for beam loss monitoring and orbit deviation. These should be able to detect the onset of unsafe losses.
- A luminosity upgrade is possible in the future for eRHIC. This will allow increased bunch repetition rate and for further increase of beam intensities. This will require faster response times for the machine protection to protect against the beam loss risks.
- The high energy electron beam, if deviates and strikes any surface, can result into secondary emission, and can result into higher radiation due to particle shower. The MPS should consider this secondary emission for critical components. The beam loss can also result into overheating of vacuum chamber and can adversely affect the superconducting elements. It can also affect the electronic hardware and permanent magnets.
- The acceleration of electrons will result into significant emission of synchrotron radiation or the Bremsstrahlung radiation. This radiation will be highest in regions where the beam takes a curved path. The limit on acceptable synchrotron radiation power is 3 MW. Similar to the electron beam, synchrotron radiation can also result into overheating of vacuum chamber and can adversely affect the superconducting elements. It can also affect the electronic hardware and permanent magnets.
- To reduce the civil construction component of the machine construction cost, all major electron accelerator components will be placed in the existing RHIC tunnel. This will call for machine protection for all these components that will be subjected to high energy ionizing radiation.

- Space Charge Compensation: The electro-magnetic interactions among charged particles, the so-called space charge forces may adversely affect the beam's stability. More importantly, this force usually is nonlinear, so introducing an additional tune spread to the circulating particles, and thereby increasing the beam losses due to the machine's non-linear resonances. The space-charge force falls quadratically with the beam's energy, and thus other nonlinear effects, such as beam-beam interactions, usually dominate high-energy colliders. However, future electron-ion colliders, such as eRHIC, are designed to operate with a range of energies. This effect should be monitored and protected against in the MPS.
- These collective effects have been recognized as most important for eRHIC: energy losses and energy spread due to collective effects, multi-pass beam breakup instability due to high order, modes of SRF cavities, and the fast beam-ion instability. MPS should be able to monitor their effect and take an action.

FFAG Beamlines and Permanent Magnets

- The FFAG lattice allows 16 beam re-circulations using only two magnet beamlines, thereby reducing the number of magnets, vacuum chambers, peripheral support equipment, and beam instrumentation devices as compared to the more standard case of separate re-circulation passes for individual beam energies. This will increase the complexity of the system in terms of orbit control, magnet technology, beam optics matching, that needs to be protected carefully.
- Permanent magnet technology is used in the FFAG beamline magnets. This eliminates the need for many power supplies. But the magnets need to protected well from the synchrotron radiation and particle beam radiation. Magnetic performance is especially important for the high-energy ring where large gradient magnets are required. This should be very closely monitored by the MPS.
- The corrosion resistance for permanent magnets will be critical as the RHIC tunnel is not very well insulated from the outside environment and especially during the summer, humid conditions are possible. The machine protection should be able to monitor this slow deterioration in the magnet performance.

- The thermal stability is a major concern for the permanent magnets, which also needs to be closely monitored by the MPS. Sophisticated temperature compensation system can also be employed that will trigger the MPS.
- The MPS should also monitor the magnetic flux loss due to neutron radiation.

Gatling Cathode Gun Injector System

- The eRHIC Gatling gun is a 20-cathode gun where the bunches originating from different cathodes are merged into one sequence using a magnetic combiner. The cathodes have a limited lifetime, requiring cathode processing and "activation" between periods of photoemission. To have a practical operating lifetime between activations the gun cathodes require an extremely high operating vacuum levels. The degradation of quantum efficiency will limit practical operating lifetime, which will require an extreme vacuum-compatible mechanism to exchange cathodes and a means of reprocessing and activation that is part of the gun system. The machine protection system should get specific updates on the vacuum inside the gun, as well as the metrics on the cathode lifetime and performance.
- The funneling combiner dipole magnet is a nontrivial development in itself requiring a magnetic field to rotate at 450 kHz. Developing in house expertise in the preparation of high quantum efficiency photocathodes is also challenging. Both of these systems can entail specialized protection system.

Superconducting RF Technology

High eRHIC luminosity demands high electron beam current accelerated in a linear accelerator operating in the continuous wave (CW) mode. Operation of the linac in CW mode calls for the use of superconducting RF technology (SRF). Otherwise the power dissipated in the cavity walls would become unacceptably high. Various SRF cavities will be used in eRHIC. A 704 MHz superconducting cavity has been developed at BNL for high-current applications. A 84 MHz SRF low frequency cavity will be used for energy-spread modification. A third harmonic (253 MHz) SRF cavity will be used to fine-tune the longitudinal phase space modification. The booster linac will employ a 422 MHz SRF cavity to accelerate the beam for injection into the main ERL.

- SRF cavities should have a stringent protection against developing quenches. Similar to the modeling of the superconducting magnets of RHIC, if an electrical model of the cavity

is to be employed, then the model should incorporate fine parasitic components. Inaccurate modeling or omission of such components for quench detection model can impact the safety and availability of eRHIC. The determination of such components can be done by frequency response analysis after the field installation of cavities.

- The energy deposition in the SRF needs to be very low for their proper operation [96]. If the beam is aborted by the MPS, excessive beam loss in the cavities has to be avoided.
- The SRF system needs to be turned on /off in a controlled fashion so that the field in the cavities does not become too large [96]. Field and phase monitoring and beam loss monitors will trigger the beam extraction and removal of RF power drive that should be administered by MPS.

Beam Dump System

A dump beamline transports the decelerated 12 MeV beam from the main ERL to the beam dump. The beamline consists of a dipole magnet, which is a part of the spreader, and two rastering quadrupoles, which disperse the beam over the beam dump surface. The beam dump has to be able to absorb a 600 kW heat load from the 12 MeV electron beam. The beam dump will be made of aluminum instead of copper to reduce neutron production. The dump consists of two sections: the body and an outer shell, containing the cooling water. The interior shape is designed to distribute the scattered electrons as uniformly as possible around the cooled surface. It should also monitor the temperature of the dump and the formation of hotspots.

7.2.3 Knowledge Base from RHIC MPS Analysis

The RHIC MPS will be an integral part of the eRHIC MPS, moreover the additional systems for eRHIC machine protection will be designed on the basis of RHIC machine protection [31] [30]. The reliability analysis in this dissertation will facilitate a knowledge base for designing the eRHIC MPS. The basic advantages offered by this methodology will be documentation of knowledge, intelligent decision support, reasoning and explanation for the design of eRHIC MPS. This section discusses the important findings and suggestions regarding the reliability of RHIC MPS that will be valuable to implement for the eRHIC MPS to enhance its performance.

The RHIC BPS has a circular topology, where a trigger originates at a certain module and then propagates all around the ring up to the beam abort system. A failed module in the path can

either hinder the trigger or cause unnecessary shutdown. Due to a long path, it causes latency in the trigger propagation to the abort system. One of the techniques to reduce the latency and dependence on the modules is to propagate the trigger in both clockwise and anti-clockwise direction, so that the trigger propagates half of the ring at the most. Similar scheme is adopted at CERN [97]. Fig. 58 shows the trigger propagation in both directions.

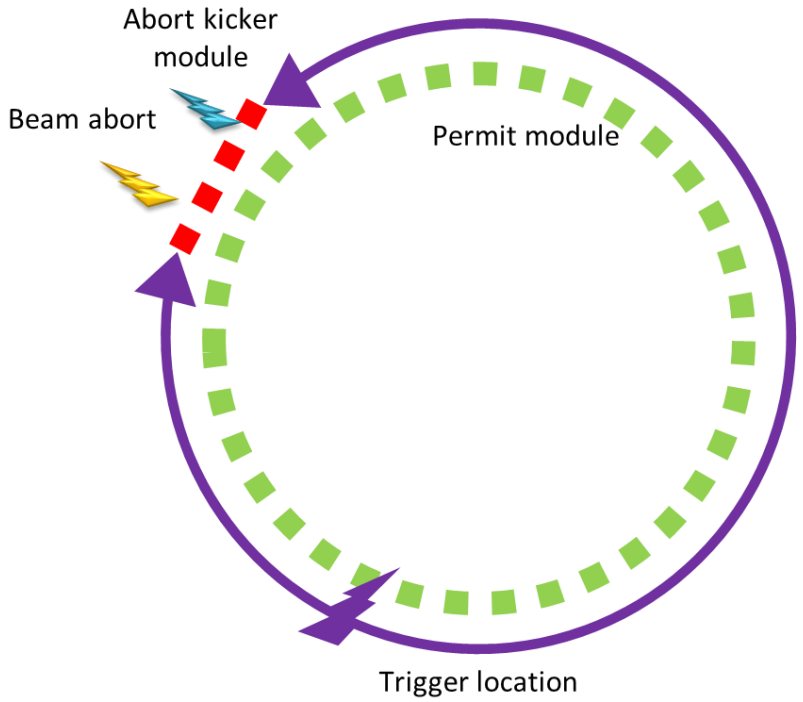

Figure 58: Bidirectional trigger propagation for eRHIC BPS

The biggest disadvantage of a circular topology is that a propagation blocking module can compromise the safety of the system. To improve the trigger propagation a star topology can be used. Here each module connects to the abort kicker with a point-to-point connection. The path of propagation is shortest, hence the latency issues are greatly reduced. The central abort kicker system can then communicate the trigger arrival to other *PMs*. The star topology is easy to design and implement. An advantage of the star topology is the simplicity of adding modules. The disadvantage is that every module can communicate to other module only through the central module(s), which needs to be very reliable. Fig. 59 shows the star topology for the BPS.

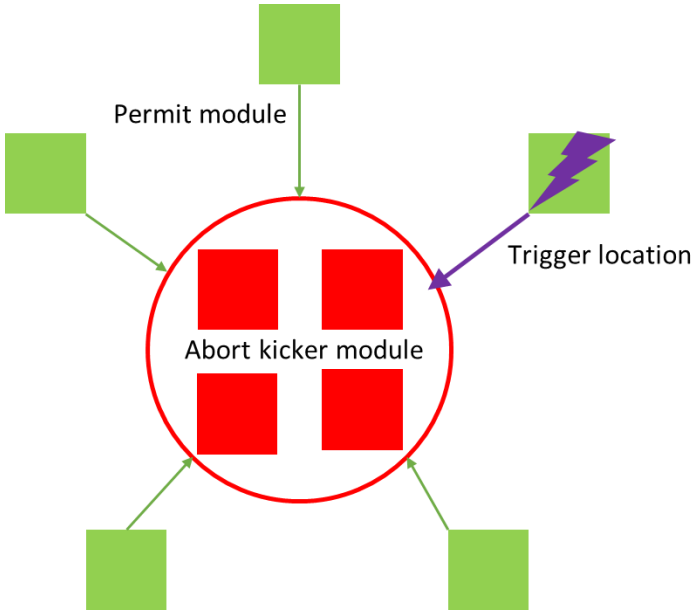

Figure 59: Star Topology for eRHIC BPS

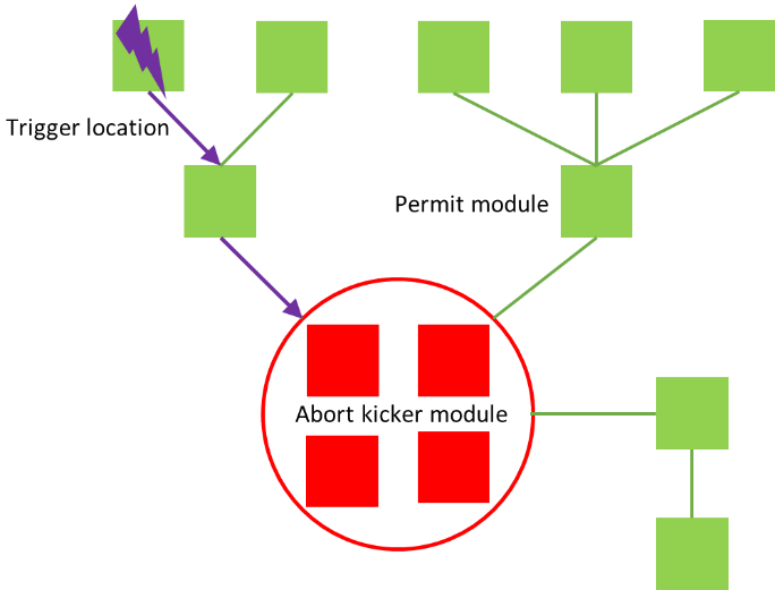

Figure 60: Tree topology for eRHIC BPS

Another topology called as the tree topology can be used, to have a hierarchical configuration of the beam permit system. Two related subsystems (say quench detection system and magnet power supply system) can be placed on the same branch of the tree, so that they communicate

effectively to each other, and a trigger can be sent through the trunk of the tree to the *AKMs*. Also the failure on one branch will not affect the other branch. This topology is also easy to expand by adding new leaf modules. Fig. 60 shows the tree topology for eRHIC BPS.

Other than this, the paths of permit link blue link and yellow link can be made totally independent of each other so that the failure of one does not affect the other link. Also redundant links can be used that run different frequency carrier signals.

As seen in section 3.4.2, the importance of the modules is highly dependent on the failure rate. Some of components can escalate the failure mode rates for individual modules. Pertaining to *FB* and *FQ* failures, fiber optic components are the major contributors. Fiber optic receiver and transmitter have a very high failure rate, that can drop the carrier causing false failure. The failure rate for the optical fibers are proportional to their length. The fiber optic connectors severely degrade with increasing mating-unmating cycles. Other electrical pin connectors also have a significant failure rate.

For *B* failure mode, the most critical components are the optocouplers that isolate the *PI* and *QI* inputs from BPS. These optocouplers can fail to switch state, which means that a trigger from the subsystems can be missed by the BPS causing a blind failure. Also there are 8 optocouplers onboard that raise the *B* failure mode to a high value. Alternative components should be considered for these specific components, or redundancy should be employed. Employing redundancy at component level is more effective than redundancy at the system level [54].

The superconducting systems are very expensive and critical systems for the operation of RHIC and eRHIC. They are specifically designed for high power applications, where normal electrical systems cannot be employed due to the resistive limits. But the superconducting systems are susceptible to quenches which can lead to catastrophic failure of the system. Temperature variations, radiation, overcurrent can initiate a quench, which needs to be precisely detected. The superconducting RF protection is discussed in section 7.2.2. Modeling of superconducting magnets should be done carefully to consider the saturation, hysteresis and parasitic components together for increased reliability of the QDS. While logging the data for current and voltage of superconducting magnets, related information regarding the applied current waveform

information, both the previous ramp and the present ramp should also be logged. This will help easy forecasting of the magnet inductance by the memory model as explained in chapter 6.

As the eRHIC systems are anticipated to scale up to 10 times of the RHIC systems, a real time comprehensive data analysis system needs to be employed. This system attempts to relate the field variables in the event of a system failure, and should be able to find the cause of the failure. It should also be able to predict a failure ahead of time by making associations with chain of events that typically occur before a failure. This could be another approach towards enhancing the reliability to a new level.

Conclusion

Due to high damage potential of the energy stored in RHIC during operation, it is very necessary to evaluate the premises under which this energy could dangerously leak causing damage to the machine. This dissertation addresses the important questions regarding the reliability of the RHIC machine protection, which is the most vital system for the operation of the RHIC. Two parts of the MPS play a pivotal role in protection: the BPS and the QDS.

RHIC BPS has been extensively studied for its reliability characteristics. Using failure data handbooks [66] [65] and manufacturer supplied failure data, a stochastic reliability model for BPS has been developed. This model encompasses the quantitative fault tree analysis [40], Monte Carlo simulation [41] and the analytical survival model [76]. The fault tree analysis helps identify and quantify the failure modes associated with BPS modules. The Monte Carlo model simulates the evolution of these failure modes to a system level perspective. The analytical survival model probes deeply into the failure probability distributions and provides a faster way to analyze the system failures with change in the system configuration. This model is verified through the Monte Carlo model.

The stochastic reliability model provides many insights into the BPS reliability performance metrics. This includes the marginal probability values of various system level catastrophic events, marginal probabilities of failure modes of individual modules, importance of each component with respect to its failure rate and structural placement, paths of failure propagation and bottlenecks in the system. This helped understand very fine failure dynamics of BPS. However, it uses the military handbook which is quite conservative in its approach.

On the other hand, the historical failure data of BPS provides the actual failure aspects of the system. This helps to quantify the overall system failure distribution that emerged as a Weibull failure distribution with decreasing failure function. It represents the real survival behavior of the BPS. However due to high the reliability of BPS, a small data of only 16 failures points till date is obtained, which does not allow to take a profound look into the system.

Thus it is necessary to emphasize the importance of both the information sources, the stochastic reliability model and the historical failure data. The Bayesian reliability model [42] facilitates a good way to coalesce these two sources to furnish the most informed inference about the BPS reliability, with flexibility to regulate the influence of either of the information sources according to the confidence in them.

The RHIC quench detection is the most crucial element of the machine protection as it is responsible for containment and safe disposal of the largest portion of the stored energy in RHIC. The reliability of RHIC QDS relies on the calibration of superconducting magnet model that detects the unsafe quench conditions. This requires an explicit modeling of the magnet electrical behavior. Statistical analysis concepts are utilized to reveal the underlying saturation characteristics of the magnet, and the model is validated using field testing [43].

Going further, a new mathematical model is developed that interprets the nonlinear effects of saturation and hysteresis of the superconducting magnets [44]. The mathematical formulation for saturation is based on empirically modeling the regional behavior of the inductance with changing current. It shows a good compliance with an analogous quantity called magnet transfer function. For hysteresis modeling, the focus is on the change in the saturation equation parameters with ramp change, and these changes are related to the existent current ramp and previous current ramp, thus incorporating the memory. The goodness-of-fit establishes the validity of the model. This model will be used for automated forecasting of the *L vs I* tables which will eliminate the need for manual calibration, thus cutting the valuable man-hours while the entire RHIC system has been cooled down to temperature of 4K.

The eRHIC [98] is an upcoming extension of RHIC machine, which will have an additional electron accelerator. RHIC machine protection will be an integral part of the eRHIC. Also, a new machine protection will be designed for the electron accelerator subsystems. The complexity of eRHIC systems are estimated to scale up by an order of magnitude, that necessitates more stringent reliability requirements. This dissertation formulates the knowledge base and renders intelligent decision support towards the eRHIC machine protection design.

Appendix A: Derivation of the competing risks formulae

Let's assume a case where *j* is *{FB, FQ, B}*. The results obtained here are generalized for *j = {1, 2... k}* risks as defined in section 2.4.2. The crude probability distribution function of risk *FB* is given by:

$$F_{FB}(t) = P[0 < T_{FB} < t;\ T_{FB} < T_{FQ};\ T_{FB} < T_B\ \ |T > 0]$$

$$F_{FB}(t) = \frac{P[0 < T_{FB} < t\ \&\ T_{FB} < T_{FQ}\ \&\ T_{FB} < T_B]}{P[T_{FB} \geq 0\ \&\ T_{FQ} \geq 0\ \&\ T_B \geq 0\ ]}$$

$$F_{FB}(t) = \frac{\int_0^t \int_{t_{FB}}^{\infty} \int_{t_{FB}}^{\infty} \lambda_{FB}\ e^{-\lambda_{FB} t_{FB}}\ .\ \lambda_{FQ}\ e^{-\lambda_{FQ} t_{FQ}}\ .\ \lambda_B\ e^{-\lambda_B t_B}\ \ dt_B\ dt_{FQ}\ dt_{FB}}{\int_0^{\infty} \int_0^{\infty} \int_0^{\infty} \lambda_{FB}\ e^{-\lambda_{FB} t_{FB}}\ .\ \lambda_{FQ}\ e^{-\lambda_{FQ} t_{FQ}}\ .\ \lambda_B\ e^{-\lambda_B t_B}\ \ dt_B\ dt_{FQ}\ dt_{FB}}$$

Here *t* represents time of observation and *T* represents time of failure.

The limits for variables in the numerator are: t_{FB} is *(0, t)*, t_{FQ} is *(t_{FB}, ∞)* and t_B is *(t_{FB}, ∞)*

The limits for variables in denominator are: *(0, ∞)* for all three t_{FB}, t_{FQ} and t_B

Solving the above expression, the crude probability distribution function becomes

$$F_{FB}(t) = \frac{\lambda_{FB}}{\lambda_{FB}\ +\ \lambda_{FQ}\ +\ \lambda_B} \left(1 -\ e^{-(\lambda_{FB} + \lambda_{FQ} + \lambda_B)t}\right)$$

By analogy

$$F_{FQ}(t) = \frac{\lambda_{FQ}}{\lambda_{FB}\ +\ \lambda_{FQ}\ +\ \lambda_B} \left(1 -\ e^{-(\lambda_{FB} + \lambda_{FQ} + \lambda_B)t}\right)$$

$$F_B(t) = \frac{\lambda_B}{\lambda_{FB}\ +\ \lambda_{FQ}\ +\ \lambda_B} \left(1 -\ e^{-(\lambda_{FB} + \lambda_{FQ} + \lambda_B)t}\right)$$

The probability of failure from risk *FB* is given by

$$\pi_{FB} = \lim_{t \to \infty} F_{FB}(t) = \lim_{t \to \infty} \frac{\lambda_{FB}}{\lambda_{FB} + \lambda_{FQ} + \lambda_B} \left(1 - e^{-(\lambda_{FB} + \lambda_{FQ} + \lambda_B)t}\right)$$

$$\pi_{FB} = \frac{\lambda_{FB}}{\lambda_{FB} + \lambda_{FQ} + \lambda_B}$$

Similarly

$$\pi_{FQ} = \frac{\lambda_{FQ}}{\lambda_{FB} + \lambda_{FQ} + \lambda_B}$$

$$\pi_B = \frac{\lambda_B}{\lambda_{FB} + \lambda_{FQ} + \lambda_B}$$

$\pi_{FB} + \pi_{FQ} + \pi_B = 1$; which means that at infinite time, the item will definitely fail from any one type of risk.

Probability of survival from all the three risks *FB*, *FQ* and *B* is $S_T(t)$, thus at any instant *t*

$$F_{FB}(t) + F_{FQ}(t) + F_B(t) + S_T(t) = 1$$

$$S_T(t) = 1 - F_{FB}(t) - F_{FQ}(t) - F_B(t)$$

$$S_T(t) = 1 - \frac{\lambda_{FB}}{\lambda_{FB} + \lambda_{FQ} + \lambda_B} \left(1 - e^{-(\lambda_{FB} + \lambda_{FQ} + \lambda_B)t}\right) - \frac{\lambda_{FQ}}{\lambda_{FB} + \lambda_{FQ} + \lambda_B} \left(1 - e^{-(\lambda_{FB} + \lambda_{FQ} + \lambda_B)t}\right) - \frac{\lambda_B}{\lambda_{FB} + \lambda_{FQ} + \lambda_B} \left(1 - e^{-(\lambda_{FB} + \lambda_{FQ} + \lambda_B)t}\right)$$

$$S_T(t) = e^{-(\lambda_{FB} + \lambda_{FQ} + \lambda_B)t}$$

References

[1] J. Chiles, Inviting Disaster, 1st edition, New York: HarperCollins , 2001.

[2] R. Billington, Reliability Evaluation of Engineering Systems, 2nd edition, Plenum Press, 1992.

[3] "Lessons Learned: Proactive Review of Large Hadron Collider (LHC) Magnet Over-Pressurization Event Leads to Improved Safety at BNL," 14 December 2009. [Online]. Available: sbms.bnl.gov.

[4] "RHIC Configuration Manual," Brookhaven National Laboratory, Upton, NY, 2006.

[5] M. Riordan, "The First Few Microseconds," Scientific American Inc, 2006.

[6] S. Wagner, "LHC Machine Protection System: Method for Balancing Machine Safety and Beam Availabilityf,," PhD thesis, ETH Zurich, 2010.

[7] M. Iwasaki, "Design and Status of the SuperKEKB Accelerator Control System," in *International Conference on Accelerator and Large Experimental Control Systems*, San Francisco, CA, 2013.

[8] J. Johnson, "KECK Telescope Control System Upgrade Project Status," in *International Conference on Accelerator and Experimental Physics Control Systems*, San Francisco, CA, 2013.

[9] G. Maire, "The Detector Safety System of NA62 Experiment," in *International Conference on Accelerator and Large Experimental Control Systems*, San Francisco, CA, 2013.

[10] L. Catani, "!CHAOS: the "Control Server" Framework for Controls," in *International Conference on Accelerator and Large Experimental Physics Control Systems*, San Francisco, CA, 2013.

[11] A. Yamashita, "A New Message-Based Data Acquisition System for Accelerator Control," in *International Conference on Accelerator and Large Experimental Physics Control Systems*, San Francisco, CA, 2013.

[12] P. Chu, "Accelerator Lattice and Model Services," in *International Conference on Accelerator and Large Experimental Physics Control Systems*, San Francisco, CA, 2013.

[13] J. Fisher, "Monitoring of the National Ignition Facility Integrated Computer Control System," in *International Conference on Accelerator and Large Experimental Physics Control Systems*, San Francisco, CA, 2013.

[14] K. Tsubota, "Keck Telescope Control System Upgrade," in *International Conference on Accelerator and Large Experimental Physics Control Systems*, Melbourne, Australia, 2015.

[15] T. Hakulinen, "Building an Interlock: Comparison of Technologies for Constructing Safety Interlocks," in *International Conference on Accelerator and Large Experimental Physics Control Systems*, Melbourne, Australia, 2015.

[16] S. Sasaki, "Upgrade of Abort Trigger System for SuperKEKB," in *International Conference on Accelerator and Large Experimental Physics Control Systems*, Melbourne, Australia, 2015.

[17] M. Pezetti, "Active Magnetic Bearings System Upgrade for LHC Cryogenic Cold Compressor, Radiations Mitigation Project (R2E)," in *International Conference on Accelerator and Large Experimental Physics Control Systems*, Melbourne, Australia, 2015.

[18] F. Tao, "Safety Integrity Level (SIL) Verification for SLAC Radiation Safety Systems," in *International Conference on Accelerator and Large Experimental Physics Control Systems*, Melbourne, Australia, 2015.

[19] A. Voitier, "Formalizing Expert Knowledge in order to Analyse CERN's Control Systems," in *International Conference on Accelerator and Large Experimental Physics Control Systems*, Melbourne, Australia, 2015.

[20] E. Matias, "CLS Control System Contribution to System Reliability," in *Accelerator Reliability Workshop*, Vancouver, Canada, 2009.

[21] J. Veray, "Cilex-Apollon Personnel Safety System," in *International Conference on Accelerator and Large Experimental Physics Control Systems*, San Francisco, CA, 2013.

[22] K. Cerff, "Evaluation of the Beamline Personnel Safety System at ANKA under the Aegis of the 'Designated Architectures' Approach," in *International Conference on Accelerator and Large Experimental Physics Control Systems*, San Francisco, CA, 2013.

[23] R. Filippini, "Reliability Analysis of the LHC Beam Dumping System Taking into Account the Operational Experience during LHC Run 1," in *International Conference on Accelerator and Large Experimental Physics Control Systems*, San Francisco, CA, 2013.

[24] R. Fleming, "NIF Device Health Monitoring," in *International Conference on Accelerator and Large Experimental Physics Control Systems*, San Francisco, CA, 2013.

[25] T. Lensch, "Machine Protection Diagnostics on a Rule Based System," in *International Conference on Accelerator and Large Experimental Physics Control Systems*, San Francisco, CA, 2013.

[26] P. Bellomo, "SLAC Next-Generation High Availability Power Supply," in *Accelerator Reliability Workshop*, Vancouver, Canada, 2009.

[27] R. Larsen, "SLAC Accelerator Research High Availability Electronics R&D Program," in *Accelerator Reliability Workshop*, Vancouver, Canada, 2009.

[28] M. Takao, "Failure Postmortem Analysis at the SPring-8 Storage Ring," in *Accelerator Reliability Workshop*, Vancouver, Canada, 2009.

[29] K. Hsu, "Post-Mortem Diagnosics for the Taiwan Light Source," in *Accelerator Reliability Workshop*, Vancouver, Canada, 2009.

[30] K. Brown, "Control System Issues and Planning for eRHIC," in *International Conference on Accelerator and Large Experimental Physics Control Systems*, San Francisco, CA, 2013.

[31] K. Brown, "Machine Protection Issues for eRHIC," in *International Conference on Accelerator and Large Experimental Physics Control Systems*, San Francisco, CA, 2013.

[32] J. Lamarre, "Performances of the Soleil Synchrotron Light Source Operation," in *Accelerator Reliability Workshop*, Vancouver, Canada, 2009.

[33] S. Krecic, "New Reliability Aspects for ELETTRA after Booster Installation," in *Accelerator Reliability Workshop*, Vancouver, Canada, 2009.

[34] R. Leitch, Reliability Analysis for engineers, 2nd edition, Oxford science publications, 1995.

[35] B. Todd, "A Beam Interlock System for CERN High Energy Accelerators," PhD Thesis, Brunel University, West London, 2006.

[36] G. Guaglio., "Reliability of the Beam Loss Monitors System for the Large Hadron Collider at CERN.," PhD thesis, Universit ´e Clermont Ferrand II - Blaise Pascal, 2005.

[37] L. Burgazzi, "Reliability Studies of a High Power Proton Accelerator for Accelerator Driven System Applications for Nuclear Waste Transmutation," *Reliability Engineering & System Safety,* vol. 4, no. 92, pp. 449 - 463, 2007.

[38] R. Filippini, "Dependability Analysis of a Safety Critical System: The LHC Beam Dumping System at CERN.," PhD thesis, Universit `a di Pisa, 2006.

[39] A. V. Fernandez, "Reliability of the Quench Protection System for the LHC superconducting elements.," PhD thesis, Universitat Polit`ecnica de Catalunya, 2003.

[40] P. Chitnis, "Quantitative Fault Tree Analysis of the Beam Permit System Elements of RHIC at BNL," in *International Conference on Accelerator and Large Experimental Physics Control Systems*, San Francisco, CA, 2013.

[41] P. Chitnis, "A Monte Carlo Simulation Approach to the Reliability Modeling of the Beam Permit System of RHIC at BNL," in *International Conference on Accelerator and Large Experimental Physics Control Systems*, San Francisco, CA, 2013.

[42] P. Chitnis, "Bayesian Reliability Model for Beam Permit System of RHIC at BNL," in *International Conference on Accelerator and Large Experimental Physics Control Systems*, Melbourne, Australia, 2015.

[43] P. Chitnis, "Nonlinear System Identification of Superconducting Magnets of RHIC at BNL," in *International Conference on Accelerator and Large Experimental Physics Control Systems*, Melbourne, Australia, 2015.

[44] P. Chitnis, "Analytical Modeling of Inductance for Saturation and Hysteresis of Superconducting Magnets," *submitted for publication.*

[45] B. Brown, "Results on Fermilab Main Injector Dipole Measurements," *IEEE Transactions on Magnetics,* vol. 32, no. 4, 1996.

[46] P. Hagen, "Comparison between Electromagnetic Models and Magnetic Measurements in the LHC Magnets," *IEEE Transactions on Applied Superconductivity*, vol. 22, no. 3, 2012.

[47] R. Gupta, "Field Quality Improvements in Superconducting Magnets for RHIC," in *European Particle Accelerator Conference*, London, UK, 1994.

[48] S. Guha, "A New Method of Modeling Magnetic Saturation in Electrical Machines," in *Canadian Conference on Electrical and Computer Engineering*, Ottawa, Canada, 2006.

[49] S. Kuehl, "Bivariate Polynomial Approximation of Cross-Saturated Flux Curves in Synchronous Machine Models," in *IEEE International Energy Conference & Exhibition*, Florence, Italy, 2012.

[50] V. Janicic, "An Approach to Modeling the Hysteresis in Ferromagnetic by Adaptation of Presaich Model," in *Telecommunications Forum TELFOR*, Serbia, Belgrade, 2014.

[51] L. Cao, "Complete Parallelogram Hysteresis Model for Electric Machines," *IEEE Transactions on Energy Conversion*, vol. 25, no. 3, Sept 2010.

[52] S. Rabbi, "Analytical Modeling of a Hysteresis Interior Permanent Magnet Motor," in *International Conference on Electrical Machines, IEEE*, Hangzhou, China, 2014.

[53] J. Hammersley, Monte Carlo Methods, 1st edition, London, 1964.

[54] L. M. Leemis, Reliability, Probabilistic Models and Statistical Methods, 2nd edition, 2009.

[55] M. Crowder, Classical Competing Risks, Chapman & Hall / CRC, 2001.

[56] T. Robertazzi, Computer Networks and Systems: Queueing Theory and Performance Evaluation, 3rd edition, 2000.

[57] "RHIC Electrical Drawings, Internal Documentation," Brookhaven National Laboratory, Upton, NY.

[58] C. Conkling, "RHIC Beam Permit and Quench Detection Communication System," in *Particle Accelerator Conference*, Vancouver, Canada, 1997.

[59] "Quench Protection System Requirements, Internal Documentation," Brookhaven National Laboratory, Upton, NY.

[60] "Quench Detection – Focusing on Tuning, Internal Documentation," Brookhaven National Laboratory, Upton, NY, 2007.

[61] W. Lee, "Fault Tree Analysis, Methods and Applications – A Review," *IEEE transactions on Reliability*, Vols. R-34, no. 3, 1985.

[62] W. Vesely, Fault Tree Handbook with Aerospace Applications, v1.1, NASA Publication, 2002.

[63] B. Dhillon, Engineering Reliability - New Techniques and Applications, John Wiley & Sons Inc, 1981.

[64] "Distribution Models for Reliability Data, Technical Support Document, Knowledgebase ID 2716," Minitab Inc.

[65] MIL-HDBK-217F, "Military Handbook-Reliability Prediction of Electronic Equipment, Department of Defense," Department of Defense, 1995.

[66] FMD-97, "Failure Mode / Mechanism Distribution," Reliability Analysis Center, Rome, NY, 1997.

[67] "JESD85, JEDEC Standard - Methods for Calculating Failure Rates in Units of FITS," JEDEC Solid State Technology Association, 2001.

[68] "Telcordia SR-332, Reliability Prediction Procedure for Electronic Equipment, Issue 1," 2001.

[69] L. Ljung, System Identification - Theory for the User, Prentice Hall Inc., 1987.

[70] M. Centikaya-Rundel, "Data Analysis and Statistical Inference, Coursera videos," Duke University, 2014. [Online]. Available: https://www.coursera.org/.

[71] D. S. Moore, The Basic Practice of Statistics, 2nd edition, W H Freeman and Company, 2000.

[72] A. W. Chao, Handbook of Accelerator Physics and Engineering, 2nd ed.,, Singapore: World Scientific Publishing Co. Pte. Ltd., 2012.

[73] "V120 RHIC Beam Permit System Module, Internal Documentation," Brookhaven National Laboratory, [Online]. Available: http://www.cadops.bnl.gov/Hardware/permit/permit.htm#P10.

[74] T. Peterson, "Magnet Quench," 01 11 2008. [Online]. Available: http://www.symmetrymagazine.org/article/november-2008/explain-it-in-60-seconds-magnet-quench.

[75] Wikipedia, "Inverse Transform Sampling," Wikipedia.org, [Online]. Available: https://en.wikipedia.org/wiki/Inverse_transform_sampling.

[76] P. Chitnis, "Understanding the Failure Characteristics of the Beam Permit System of RHIC at BNL," in *International Conference on Accelerator and Large Experimental Physics Control Systems*, Melbourne, Australia, 2015.

[77] "Mathematica - Version 9," Wolfram Research Inc., Champaign, IL, 2014.

[78] S. T. Rachev, *Private Communication*, Stony Brook, NY: Professor of Finance, Stony Brook University, 2014.

[79] S. T. Rachev, Bayesian Methods in Finance, John Wiley & Sons, Inc, 2008.

[80] B. Vidakovic, "MCMC Methodology," [Online]. Available: http:// www2.isye.gatech.edu/~brani/isyebayes/bank/handout10.pdf.

[81] S. M. Ross, Introduction to Probability Models, 10th ed., Elsevier Inc., 2010.

[82] *MATLAB® Release 2015a*, Natick, MA,: The MathWorks Inc., 2015.

[83] K. Burnham, Model Selection and Multimodel Inference: A Practical Information Theoretic Approach, 2nd edition, Springer Inc., 2002.

[84] V. V. Kashikhin, "Magnetic Instabilities in Nb3Sn Strands and Cables," *IEEE Transactions on Applied Superconductivity*, vol. 15, no. 2, 2005.

[85] A. Jain, *Private communication*, Upton, NY: Superconducting Magnet Division, Brookhaven National Laboratory, 2015.

[86] F. Pilat, "ATR Magnet Transfer Functions, Technical Note," Brookhaven National Laboratory, Upton, NY, 1996.

[87] "RHIC Magnet Database - "magbase"," Brookhaven National Laboratory, 2015. [Online]. Available: http://www.rhichome.bnl.gov/RHIC/Runs/.

[88] B. Brown, "Hysteresis Study Techniques and Results for Accelerator Magnets with Unipolar Current Excitation," in *Particle Accelerator Conference*, New York, 1999.

[89] W. Fischer, "Run Overview of the Relativistic Heavy Ion Collider," 29 Oct 2015. [Online]. Available: http://www.rhichome.bnl.gov/RHIC/Runs/.

[90] C. Schultheiss, *Private Communication*, Upton, NY: Collider Accelerator Department, Brookhaven National Laboratory, 2015.

[91] G. Morgan, "Final Report of the Task Force on the RHIC Iron Specification, Note 420," Brookhaven Magnet Division, Brookhaven National Laboratory, Upton, NY, 1992.

[92] "eRHIC design study," Brookhaven National Laboratory, Upton, NY, 2014.

[93] "Electron Ion Collider: The Next QCD Frontier, 2nd edition," Brookhaven National Laboratory, Upton, NY, 2014.

[94] R. Filippini, "Reliability Assessment of the LHC Machine Protection System," in *Particle Accelerator Conference*, Knoxville, Tennessee, 2005.

[95] B. Dehning, "LHC Machine Protection," in *Beam Instrumentation Workshop*, Tahoe City, CA, 2008.

[96] "Cornell Energy Recovery Linac - Science Case and Project Definition Design Report," Cornell University, Ithaca, NY, 2013.

[97] B. Puccio, "The CERN Beam Interlock System: Principle and Operational Experience," in *International Particle Accelerator Conference*, Kyoto, Japan, 2010.

[98] V. Ptitsyn, "eRHIC, A Future Electron-Ion Collider at BNL," in *European Particle Accelerator Conference*, Luceme, 2004.